Nanoscale Characterization of Lead-Free Piezoceramics Using Atomic Force Microscopy

Xijie Jiang

Dissertation submitted as a requirement for the degree of Doctor of Natural Science
September 2022 – Technical University of Darmstadt (TUDa) – D17

Physics of Surfaces

MATERIAL-WISSENSCHAFT

TECHNISCHE UNIVERSITÄT DARMSTADT

This page was intentionally left blank

Nanoscale Characterization of Lead-Free Piezoceramics Using Atomic Force Microscopy

Dissertation Submitted to the Department of Materials and Earth Sciences at Technische Universität Darmstadt

in Fulfillment of the Requirements for the Degree of
Doctor of Natural Science (Dr. rer. nat.)

By
Xijie Jiang

M.Sc. Solid State Electric Physics 2015
B.Eng. Material Science and Engineering 2012

Born in China

Referee: Prof. Dr. Robert W. Stark
Co-referee: Prof. Dr. Wolfgang Donner

Date of Submission: 20. 09. 2022
Date of Oral Examination: 15. 12. 2022

TECHNISCHE
UNIVERSITÄT
DARMSTADT

Technische Universität Darmstadt, Hochschulkennziffer D17

Darmstadt 2022

Jiang, Xijie: Nanoscale Characterization of Lead-Free Piezoceramics Using Atomic Force Microscopy

Darmstadt, Technische Universität Darmstadt
Publication Year of Dissertation at TUprints: 2023
URN: urn:nbn:de:tuda-tuprints-231596
Date of Oral Examination: 15. 12. 2022

THESIS SUPERVISORS

Prof. Dr. Robert W. Stark

Professor of Material Science
Geo- and Material Sciences Department
Technical University of Darmstadt

Dr. Christian Dietz
Geo- and Material Sciences Department
Technical University of Darmstadt

THESIS COMMITTEE

Prof. Dr. Robert W. Stark

Referee
Professor of Material Science
Geo- and Material Sciences Department
Technical University of Darmstadt

Prof. Dr. Wolfgang Donner
Co-referee
Professor of Material Science
Geo- and Material Sciences Department
Technical University of Darmstadt

Prof. Dr. Leopoldo Molina-Luna
Examiner
Professor of Materials Science
Geo- and Material Sciences Department
Technical University of Darmstadt

Prof. Dr. Ulrike Kramm
Examiner
Professor of inorganic chemistry
Chemistry Department
Technical University of Darmstadt

This page was intentionally left blank

“Diligence is the means by which one makes up for one's dullness.”

“勤能补拙”

This page was intentionally left blank

Nanoscale Characterization of Lead-Free Piezoceramics Using Atomic Force Microscopy

By Xijie Jiang

Submitted to the Department of Materials and Earth Sciences on 20.09.2022 in Partial Fulfillment of the Requirements for the Degree of Doctor of Philosophy in Material sciences

ABSTRACT

The last 35 years have seen a tremendous advancement in atomic force microscopy (AFM) in terms of its versatility and resolving power in exploring the functional properties of materials. Among them, the introduction of the piezoresponse force microscopy (PFM) technique, pioneered by Güthner and Dransfeld in 1992, has turned into a mainstream method for probing and controlling the static and dynamic properties of nanoscale ferroic structures and devices. PFM enables non-destructive visualization and manipulation of ferroelectric nanodomains and direct measurements of the local physical characteristics of ferroelectrics. Using the PFM technique, the work in this thesis is dedicated to studying ferroelectric domain structure in lead-free piezoceramics from two perspectives. On the one hand, the underlying mechanisms of measured functional properties in piezoceramics have been probed by direct observation with PFM. On the other hand, the domain structure evolution of piezoceramics under external stimuli has been visualized, thereby revealing their potential applications. Several different AFM techniques, including standard PFM, Kelvin probe force microscope (KPFM), and switching spectroscopy PFM, have been utilized for making the comprehensive study.

Firstly, the evolution of the domain structure of a lead-free $Ba(Zr_{0.2}Ti_{0.8})O_3$-$x(Ba_{0.7}Ca_{0.3})TiO_3$ (BZT-xBCT) piezoceramic under temperature and electric field stimulation on micrometer and nanometer scales was studied. The PFM results highlight the critical role of wedge-shaped domains in domain evolution. Transitional domain structures with an increased density of nanodomains appear in both the thermal and poling cycles. Interestingly, the electric-field-dependent domain structure evolution at different temperatures shows better domain structure reversibility at high temperatures than at temperatures close to the phase boundary, implying a slow rate of fatigue for the functional properties in this temperature range.

Next, the unipolar fatigue behavior of three BZT-xBCT compositions with different crystallographic structures, *i.e.*, 40BCT(R), 50BCT(O) and 60BCT(T), were evaluated. PFM studies were performed to relate the fatigue behavior to the different strain mechanisms of each of the three studied compositions. PFM domain maps indicate that the high amount of extrinsic contributions to strain made orthorhombic 50BCT(O) and rhombohedral 40BCT(R) compositions most susceptible to fatigue during unipolar cycling. Unlike them, the tetragonal composition 60BCT(T) has a high amount of

intrinsic contributions to strain, making it more resistant to electric fatigue, resulting in relatively stable electromechanical properties.

$Na_{1/2}Bi_{1/2}TiO_3$-based compositions have been another promising candidate for lead-free piezoceramics. With the inclusion of ZnO, the depolarization temperature of $0.94Na_{1/2}Bi_{1/2}TiO_3$-$0.06BaTiO_3$:0.1ZnO relaxor ferroelectric/semiconductor composites is enhanced. Room temperature PFM data directly demonstrate a long-range ferroelectric order induced by the ZnO inclusion in NBT-6BT:0.1ZnO composites. Also, PFM results show a slow rate of depolarization after poling in NBT-6BT:0.1ZnO composites. Compared to pure NBT-6BT ceramics, site-specific PFM hysteresis loops were acquired to reveal the modification of local ferroelectricities with the ZnO inclusion. In addition, I tried to map the domain structure of BT under different creep mechanisms with the PFM technique.

Taking advantage of the unique advantages of AFM in terms of good spatial resolution and versatility, this thesis presents four studies on lead-free piezoceramics in terms of structural morphology, domain structure, domain wall dynamic, local hysteresis properties, and local potential. It provides an in-depth understanding of functional behaviors in piezoceramics from the structure point of view, primarily the ferroelectric domain (wall) structure.

ZUSAMMENFASSUNG

In den letzten 35 Jahren hat sich die Rasterkraftmikroskopie (AFM) in Bezug auf ihre Vielseitigkeit und ihr Auflösungsvermögen bei der Erforschung der funktionellen Eigenschaften von Materialien enorm weiterentwickelt. Die Einführung der Piezoresponse-Kraftmikroskopie (PFM), die 1992 von Güthner und Dransfeld eingeführt wurde, hat sich zu einer gängigen Methode für die Untersuchung und Kontrolle der statischen und dynamischen Eigenschaften von nanoskaligen ferroischen Strukturen und Geräten entwickelt. PFM ermöglicht die zerstörungsfreie Visualisierung und Manipulation ferroelektrischer Nanodomänen und direkte Messungen der lokalen physikalischen Eigenschaften von Ferroelektrika. Mit Hilfe der PFM-Technik wird in dieser Arbeit die ferroelektrische Domänenstruktur in bleifreien Piezokeramiken aus zwei Perspektiven untersucht. Einerseits haben wir die zugrundeliegenden Mechanismen der gemessenen funktionellen Eigenschaften in Piezokeramiken durch direkte Beobachtung mit PFM untersucht. Andererseits haben wir die Entwicklung der Domänenstruktur von Piezokeramiken unter externen Stimuli visualisiert und damit ihr Anwendungspotenzial aufgezeigt. Für die umfassende Studie wurden verschiedene AFM-Techniken eingesetzt, darunter das Standard-PFM, das Kelvin-Sondenkraftmikroskop (KPFM) und das PFM mit Schaltspektroskopie.

Zunächst untersuchten wir mit PFM die Entwicklung der Domänenstruktur einer bleifreien $Ba(Zr_{0.2}Ti_{0.8})O_3$-$x(Ba_{0.7}Ca_{0.3})TiO_3$ (BZT-xBCT) Piezokeramik unter Temperatur- und elektrischer Feldanregung im Mikrometer- und Nanometerbereich. Die PFM-Ergebnisse unterstreichen die kritische Rolle der keilförmigen Domänen bei der Domänenentwicklung. Übergangsdomänenstrukturen mit einer erhöhten Dichte von Nanodomänen treten sowohl in den thermischen als auch in den Polungszyklen auf. Interessanterweise zeigt die vom elektrischen Feld abhängige Entwicklung der Domänenstruktur bei verschiedenen Temperaturen eine bessere Reversibilität der Domänenstruktur bei hohen Temperaturen als bei Temperaturen nahe der Phasengrenze, was auf eine langsame Ermüdungsrate für die funktionellen Eigenschaften in diesem Temperaturbereich schließen lässt.

Anschließend wurde das unipolare Ermüdungsverhalten von drei BZT-xBCT-Zusammensetzungen mit unterschiedlichen kristallographischen Strukturen, d. h. 40BCT(R), 50BCT(O) und 60BCT(T), untersucht. Es wurden PFM-Studien durchgeführt, um das Ermüdungsverhalten mit den unterschiedlichen Belastungsmechanismen der drei untersuchten Zusammensetzungen in Verbindung zu bringen. PFM-Domänenkarten zeigen, dass die orthorhombischen 50BCT(O)- und rhomboedrischen 40BCT(R)-Zusammensetzungen aufgrund des hohen extrinsischen Anteils an der Dehnung am anfälligsten für Ermüdung während unipolarer Zyklen sind. Im Gegensatz dazu weist die tetragonale Zusammensetzung 60BCT(T) einen hohen Anteil an intrinsischen Dehnungsbeiträgen auf,

was sie widerstandsfähiger gegen elektrische Ermüdung macht und zu relativ stabilen elektromechanischen Eigenschaften führt.

$Na_{1/2}Bi_{1/2}TiO_3$-basierte Zusammensetzungen sind ein weiterer vielversprechender Kandidat für bleifreie Piezokeramiken. Durch den Zusatz von ZnO wird die Depolarisationstemperatur von $0.94Na_{1/2}Bi_{1/2}TiO_3$-$0.06BaTiO_3$:0.1ZnO-Relaxor-Ferroelektrik/Halbleiter-Kompositen erhöht. PFM-Daten bei Raumtemperatur zeigen direkt eine ferroelektrische Ordnung mit großer Reichweite, die durch den ZnO-Einschluss in NBT-6BT:0.1ZnO-Verbundwerkstoffen hervorgerufen wird. Außerdem zeigen die PFM-Ergebnisse eine langsame Depolarisationsrate nach der Polung in NBT-6BT:0.1ZnO-Verbundwerkstoffen. Im Vergleich zu reinen NBT-6BT-Keramiken wurden ortsspezifische PFM-Hystereseschleifen erfasst, um die Veränderung der lokalen Ferroelektrizitäten durch den ZnO-Einschluss aufzuzeigen. Darüber hinaus haben wir versucht, die Domänenstruktur von BT unter verschiedenen Kriechmechanismen mit der PFM-Technik abzubilden.

Unter Ausnutzung der einzigartigen Vorteile der AFM in Bezug auf eine gute räumliche Auflösung und Vielseitigkeit, präsentiert diese Arbeit vier Studien über bleifreie Piezokeramiken in Bezug auf strukturelle Morphologie, Domänenstruktur, Domänenwanddynamik, lokale Hystereseeigenschaften und lokales Potenzial. Sie bietet ein tiefgreifendes Verständnis des funktionellen Verhaltens von Piezokeramiken aus struktureller Sicht, insbesondere der ferroelektrischen Domänenstruktur (Wand).

ACKNOWLEDGMENTS

In this part, I would like to thank all the people who helped me and encouraged me during this period. I would not have completed my study without the guidance, support, help, and encouragement of many people. I sincerely thank you all for making such an unforgettable experience.

First and foremost, I deeply appreciate my thesis supervisor, Prof. Dr. Robert Stark, for giving me this study opportunity in his group at the Technische Universität Darmstadt. I am very grateful for his support, patience, and inspiration throughout my doctoral study, especially during my parental leave. Robert offered complete freedom of my PhD research and gave me financial support during my stay at TU Darmstadt, which made my life much easier. Without him, I would not finish my Ph.D. in this pleasant situation.

I sincerely thank my another supervisor, Dr. Christian Dietz, for his full support and the countless discussions we had. I appreciate all his contributions, which made my thesis work smooth. Christian has been continuously guiding me to understand the theories of atomic force microscopy and giving physical insights to my projects. He also gave me a lot of valuable suggestions in my life and helped me a lot when I had some problems with the German language. He is a very kind and enthusiastic person. I feel fortunate to work with and learn from the exemplary scientist.

I am grateful to Prof. Dr. Wolfgang Donner for being the co-referee of my PhD thesis and helping correcting my thesis. I also would like to thank Prof. Dr. Leopoldo Molina-Luna and Prof. Dr. Ulrike Kramm for being my thesis examiners and giving valuable comments.

I owe my sincere thanks to Dr. Na Liu for her generous help and encouragement. Na has introduced me to the experimental techniques and has been giving beneficial advice whenever I consult her. She is also my flatmate and best friend, and I will never forget the happy time we had together.

I am grateful to my wonderful collaborators for their indispensable input and pleasant collaboration with the Group of Prof. Dr. Jürgen Rödel. Dr. Virginia Rojas has provided the $Ba(Zr_{0.2}Ti_{0.8})O_3$-$x(Ba_{0.7}Ca_{0.3})TiO_3$ (BZT-xBCT) samples for me. The macroscopic functional behaviors, such as macroscopic bipolar and unipolar hysteresis loops and strain loops, as well as the relevant piezoelectric coefficient, were studied by her. $0.94(Na_{1/2}Bi_{1/2})TiO_3$-$0.06BaTiO_3$:$x$ZnO (NBT-6BT:$x$ZnO) samples were offered by Lukas M. Riemers and Dr. Lalitha K Venkataraman. They provided all the macroscopic structure analysis, such as XRD, SEM, and hysteresis loops. Dr. Rongpeng Ren supplied BaTiO3 (BT) samples with different creep temperatures and SEM measurements. All the information they offered, including the knowledge they shared during the discussion, helped me a lot and gave me a reference for my further investigation. Dr. Jurij Koruza oversaw the whole work and gave me a lot of expert suggestions from the aspect of piezoceramics.

I also acknowledge many lovely and warm-hearted people in the PoS group. Marcus Schulze helped me a lot in the laptop techniques and introduced me to magnetic force microscopy; Sabine Hesse helped me order the cantilevers; Lars-Oliver Heim introduced me the MFP-3D; Chen Shen helped me in PFM measurement. Alena Bell, Lukas Stühn, Julia Auernhammer, Asma Siddique, and Anahid Amiri, we had a pleasant and unforgettable time together. It has been a significant and enjoyable period in my life.

Last but not least, I would like to express my sincere thanks to my family. My parents have always given their all to support me to receive the best education possible. They are continuously concerned about my well-being and health. My sisters always support me and inspire me. My husband and my son bring a lot of happiness to my life. Your love and encouragement always warm my life and inspire me to pursue excellence.

BIOGRAPHICAL NOTE

EDUCATION

Dr.rer.nat.	**Technical University of Darmstadt (TUDa)**		**2016–2022**
	Surface Physics, Materials Science	*Supervised by,* Prof. Dr. Robert W. Stark	
M.Sc.	**Ningbo University**		**2012–2015**
	Solid State Electronic Physics	*Supervised by,* Prof. Dr. Laihui Luo	
B.Eng.	**University of Jinan**		**2008–2012**
	Materials Science and Engineering	*Supervised by,* Prof. Xianqin Hou	

PUBLICATIONS

Published:

A. **Jiang, X.**, Dietz, C., Liu, N., Rojas, V. & Stark, R. W. *Ferroelectric Domain Evolution in A $Ba(Zr_{0.2}Ti_{0.8})O_3$-$0.5(Ba_{0.7}Ca_{0.3})TiO_3$ Piezoceramic Studied Using piezoresponse Force Microscopy.* Applied Physics Letters, (2021). **118**, 262902

B. Riemer, L. M., Venkataraman, L. K., **Jiang, X.**, Liu, N., Dietz, C., Stark, R. W., ... & Rödel, J. *Stress-induced phase transition in lead-free relaxor ferroelectric composites*. Acta Materialia, (2017). **136**: 271-280.

C. Rojas, V., Koruza, J., Patterson, E. A., Acosta, M., **Jiang, X.**, Liu, N., ... & Rödel, J. *Influence of composition on the unipolar electric fatigue of $Ba(Zr_{0.2}Ti_{0.8})O_3$-$(Ba_{0.7}Ca_{0.3})TiO_3$ lead-free piezoceramics*. Journal of the American Ceramic Society, (2017). **100**(10): 4699-4709.

D. Luo, L., **Jiang, X.**, Zhang, Y., & Li, K. *Electrocaloric effect and pyroelectric energy harvesting of $(0.94\text{-}x)Na_{0.5}Bi_{0.5}TiO_3$-$0.06BaTiO_3$-$xSrTiO_3$ ceramics*. Journal of the European Ceramic Society, (2017). **37**(8): 2803-2812.

E. Wang, H., **Jiang, X.**, Wang, Y., Stark, R. W., van Aken, P. A., Mannhart, J., & Boschker, H. *Direct observation of huge flexoelectric polarization around crack tips.* Nano Letters. (2019). **20**(1): 88-94.

F. Ren, P., Höfling, M., Koruza, J., Lauterbach, S., **Jiang, X.**, Frömling, T., ... & Kleebe, H. J. *High temperature creep-mediated functionality in polycrystalline barium titanate.* Journal of the American Ceramic Society, (2020). **103**(3), 1891-1902.

G. Wang, H., Srot, V., **Jiang, X.**, Yi, M., Wang, Y., Boschker, H., Merkle, R., Stark, R., Mannhart, J., van Aken, P. *Probing Charge Accumulation at $SrMnO_3/SrTiO_3$ Hetero-interfaces via Advanced Electron Microscopy and Spectroscopy*. ACS Nano. (2020). **14**(10): 12697-12707.

Published: Earlier Work

1. **Jiang, X.**, Wang, B., Luo, L., Li, W., Zhou, J., & Chen, H. *Electrical properties of $(1-x)(Bi_{0.5}Na_{0.5})TiO_{3-x}KNbO_3$ lead-free ceramics*. Journal of Solid State Chemistry, (2014). **213**: 72-78.
2. **Jiang, X.**, Luo, L., Wang, B., Li, W., & Chen, H. *Electrocaloric effect based on the depolarization transition in $(1-x)Bi_{0.5}Na_{0.5}TiO_3–xKNbO_3$ lead-free ceramics*. Ceramics International, (2014). **40**(2): 2627-2634.
3. Luo, L., Wang, B., **Jiang, X.**, & Li, W. *Energy storage properties of $(1-x)(Bi_{0.5}Na_{0.5})TiO_3–xKNbO_3$ lead-free ceramics*. *Journal of materials science*, (2014). **49**(4), 1659-1665.
4. Wang, B., Luo, L., **Jiang, X.**, Li, W., & Chen, H. *Energy-storage properties of $(1-x)Bi_{0.47}Na_{0.47}Ba_{0.06}TiO_3–xKNbO_3$ lead-free ceramics.* Journal of alloys and compounds, (2014). **585**: 14-18.
5. Yue, Q., Luo, L., **Jiang, X.**, Li, W., & Zhou, J. *Aging effect of Mn-doped $Ba_{0.77}Ca_{0.23}TiO_3$ ceramics*. Journal of alloys and compounds, (2014). 610, 276-280.

Conference contributions

a. **Jiang, X.**, Liu, N., Rojas, V., Koruza J., Stark, R. W., Dietz, C. "*Nanoscale piezoelectric properties of (1-x)$Ba(Zr_{0.2}Ti_{0.8})O_3$-x$(Ba_{0.7}Ca_{0.3})TiO_3$ ceramics studied by piezoresponse force microscopy*", poster presentation, ISAF/ECAPD/PFM Conference. Darmstadt, Germany, August 21th-25th, 2016.
b. **Jiang, X.**, Liu, N., Rojas, V., Koruza J., Stark, R. W., Dietz, C. "*Nanoscale piezoelectric properties of (1-x)$Ba(Zr_{0.2}Ti_{0.8})O_3$-x$(Ba_{0.7}Ca_{0.3})TiO_3$ ceramics studied by piezoresponse force microscopy*", poster presentation, Materials Science and Engineering. Darmstadt, Germany, September 27th-29th, 2016.
c. **Jiang, X.**, Liu, N., Rojas, V., Koruza J., Stark, R. W., Dietz, C. "*Domain evolution in $Ba(Zr_{0.2}Ti_{0.8})O_3$-0.5$(Ba_{0.7}Ca_{0.3})TiO_3$ (BZT-0.5BCT) piezoceramic studied by piezoresponse force Microscopy*", poster presentation, German Physical Society Spring Meeting. Berlin, Germany, March 11th-16th, 2018.
d. Wang, H., Boschker, H., **Jiang, X.**, Wang, Y., Stark, R. W., Mannhart, J., van Aken, P. A. "Atomic-scale imaging of flexoelectric polarization around engineered crack tips," poster presentation, Microscopy & Microanalysis (M&M) 2021, online, August 1-5, 2021.

Contents

List of Figures

List of Tables

List of Abbreviations

AC	Alternating current
AFM	Atomic force microscope
AM-KPFM	Amplitide modulated Kelvin probe force microscopy
BCT	Barium calcium titanate $(Ba_{0.7}Ca_{0.3})TiO_3$
BT	Barium titanate $BaTiO_3$
BZT	Barium zirconium titanate $Ba(Zr_{0.2}Ti_{0.8})O_3$
CPD	Contact potential difference
CPE	Converse piezoelectric effect
DC	Direct current
DW	Domain walls
FM-KPFM	Frequency modulated Kelvin probe force microscopy
KNN	Potassium sodium niobate $K_{1/2}Na_{1/2}NbO_3$
KPFM	Kelvin probe force microscopy
LiA	Lock-in amplifier
LPFM	Lateral piezoresponse force microscopy
MPB	Morphotropic phase boundary
NBT	Bismuth sodium titanate $Na_{1/2}Bi_{1/2}TiO_3$
PFM	Piezoresponse force microscopy
PLZT	Lead lanthanum zirconate titanate $Pb_{1-x}La_x(Zr_{1-y}Ti_y)_{1-x/4}O_3$
PMN	Lead magnesium niobate $Pb(Mg_{1/3}Nb_{2/3})O_3$
PPT	Polymorphic phase transition
PR	Piezoelectric response
PT	Lead titanate $PbTiO_3$
PZN	Lead zinc niobate $Pb(Zn_{1/3}Nb_{2/3})O_3$
PZT	Lead zirconate titanate $Pb(Zr_{1-y}Ti_y)O_3$
RT	Room temperature
SEM	Scanning electron microscopy
SNR	Signal-to-noise ratio

SPM	Scanning probe microscopy
SS-PFM	Scanning spectroscopy piezoresponse force microscopy
STO	Strontium titanate $SrTiO_3$
TEM	Transmission electron microscopy
VDW	Van der Waals
VPFM	Vertical piezoresponse force microscopy
XRD	X-ray diffraction

List of Symbols

d_{33}	Piezoelectric coefficient measured along the poling direction
d_{33}^*	Large signal piezoelectric coefficient
φ	Phase shift with respect to the driving field
E	Electric field
E_c	Coercive electric field
χ	Electrical susceptibility
P	Electric polarization
P_{max}	Maximum polarization
P_s	Spontaneous polarization
P_r	Remanent polarization
T_C	Curie temperature
T_d	Depolarization temperature
T_m	Maximum dielectric constant temperature
tan(δ)	Dielectric loss factor
t	Tolerance factor
Φ	Work function
ε	Dielectric permittivity
ε_r	Relative dielectric permittivity
ε_r'(0)	Zero-field permittivity
k_{33}	Coupling factor
f_{CR}	Contact resonance frequency
k	Spring constant
V_{ac}	Driving voltage
V_{dc}	Poling voltage
E_v	vacuum energy level
E_{ft}	Fermi energy level of tip
E_{fs}	Fermi energy level of sample
R	Rhombohedral

T	Tetragonal
O	Orthorhombic
C	Cubic

1. Introduction

Ferroelectric materials have attracted considerable interest in various real-life applications, including transducers, sensors, memory cells, actuators, generators, and ultrasonic motors. [1-5] However, the lead-containing materials based on lead zirconate titanate $Pb(Zr_{1-x}Ti_x)O_3$ (PZT) are dominant in most applications due to their outstanding piezoelectric performance, low cost, and good stability. [6] Since the first report of PZT in the 1950s [7], lead-containing materials have an estimated market share of billions of dollars worldwide. [8] However, searching for alternative lead-free materials for PZT has been initiated in environmental regulations in many countries because of the hazardous effect of toxic lead on the environment and humans. Since the release of the regulations [9-11], one primary research topic in the field has been to look for lead-free materials [12-15] with piezoelectric properties competitive with lead-containing materials. To date, numerous lead-free systems with excellent piezoelectric behaviors have been reported. Among them, potassium sodium niobate $K_{1/2}Na_{1/2}NbO_3$ (KNN)-based [16-18], sodium bismuth titanate $Na_{1/2}Bi_{1/2}TiO_3$ (NBT)-based [19-23] and barium titanate $BaTiO_3$ (BT)-based [24, 25] materials have been recognized as most promising substitutions for PZT. However, the replaceable environmentally friendly materials for PZT in all devices have not been found due to the lower electromechanical properties. [12, 18, 26, 27]

Barium titanate $BaTiO_3$ (BT) is a typical lead-free perovskite ferroelectric material. BT-based ferroelectric ceramics have gained tremendous attention in the electronic industry as they have high dielectric constant and have been extensively explored in dielectric capacitors and high-energy storage devices. [28, 29] BT has a cubic perovskite structure above Curie temperature $T_C \approx 128°C$. Below T_C, it first transforms to the tetragonal phase and then to orthorhombic at about 5°C. In the tetragonal phase state, the fourfold rotation axis is the polar direction (*c*-axis). Because of this, domain walls between antiparallel polarizations and domain walls between orthogonal polarizations, which are also called 180° walls and 90° walls, respectively, are exited in BT. Since the macroscopic electromechanical behavior of ferroelectrics is mainly determined by the domain structure and their dynamic response to the temperature and applied electric fields, it is crucial to observe domain morphology in order to get the relation between macroscopic electromechanical properties and the microscopic properties of ferroelectrics. [12, 30-32] It is, therefore, necessary to understand ferroelectric structures with respect to the size, morphology, and dynamic response and evolution to a static or dynamic external electric stimulus or temperature change down to the nanoscale. However, the underlying mechanism of the ferroelectric behavior of BT-based ferroelectrics at the nanoscale dimension is by far needs further improvement. During the present decade, nanoscale investigation of ferroelectric properties from micron to nanoscales has become increasingly important.

Domain morphology can be influenced by many reasons, such as the applied electric field and the temperature. The domain structure and its dynamics in a ferroelectric sample determine the macroscopic ferroelectric properties, such as the dielectric susceptibility and piezoelectric response.

[33, 34] Moreover, the contribution of the domain walls dominates the emergence of these changes. [35] Many techniques for sying ferroelectric domain were developed, e.g., X-ray diffraction (XRD) [36, 37], diffuse neutron scattering [38, 39], dielectric spectroscopy [40, 41] and high-resolution transmission electron microscopy (TEM) [42]. All techniques have their pros and cons. However, these techniques generally do not directly measure the ferroelectric domain and its evolution.

Today the scanning probe microscope (SPM) is an essential tool in nanoscience and nanotechnology. It can be used to characterize the domain structures and observe local polarization dynamics of ferroelectric materials with high resolution in a non-destructive manner. [43-45] Atomic force microscopy (AFM), based on the probe–sample interaction and capable of measuring non-conductive materials, has been a leading technique of SPM. More interestingly, AFM is able to sy a broad range of materials operating in various conditions: liquids, vacuum, gases, air, and different temperatures. AFM has a high spatial resolution below the nanometer scale. Among the SPM techniques, piezoresponse force microscopy (PFM) has been the most popular technique for characterizing ferroelectric domain structure. [45] PFM allows for imaging and manipulating the piezoelectric/ferroelectric domains at the nanometer scale. PFM was first implemented by Güthner and Dransfeld in 1992. After that, PFM has steadily attracted more and more interest and substantially developed and used to characterize ferroelectric materials. [46-51] Compared with other nanoscale ferroelectrics measured techniques, PFM can measure the ferroelectric materials with a high spatial resolution (a few tens of nanometers) without destroying the sample. PFM can acquire topography and piezoresponse simultaneously and effectively manipulate nanoscale domains and local spectroscopy capabilities.[52-55]

This thesis focuses on observing the nano-domain structure and its dynamic in BT-based ferroelectrics using the PFM technique. The domain evolution in lead-free $Ba(Zr_{0.2}Ti_{0.8})O_3$-$x(Ba_{0.7}Ca_{0.3})TiO_3$ (BZT-xBCT) piezoceramics under the external stimulus and $0.96(Na_{1/2}Bi_{1/2})TiO_3$-$0.06BaTiO_3$ (NBT-6BT) piezoceramic with the ZnO inclusion has been extensively studied. Furthermore, the correlation between the domain structure and the unipolar fatigue behavior in BZT-xBCT piezoceramics and high temperature creep behavior in polycrystalline BT were investigated. This thesis aims to gain an insight into the fundamental physical mechanisms and thus unravel the domain-structure-property relationships in ferroelectrics and decipher the underlying mechanisms of the macroscopic properties of studied materials.

2. Fundamentals and Experiments

The basic principles of dielectric, piezoelectric, and ferroelectric properties are introduced in this chapter. The related underlying structural mechanisms are depicted as well. The fundamentals for ferroelectric domain and scanning probe microscope techniques used in this thesis are introduced, primarily based on books of Ref. [56-58]. A brief summary of famous lead-free ferroelectric systems is given. Furthermore, the ferroelectric properties and related mechanisms of BZT-*x*BCT and NBT-based systems are discussed. It is worth noting that the basic principles and illustrations of the materials are mainly based on these books [7, 28, 59-63].

2.1 Fundamental of the Materials with their Dielectric, Piezoelectric, and Ferroelectric Properties

32 possible combinations of symmetry operations result in the 32 crystal classes, which are often also referred to as the 32 point groups. There are 32 crystal classes classified for all crystallized materials. According to their pyroelectric, piezoelectric, electrostrictive and ferroelectric properties, these crystal classes can be divided into groups, as shown in Fig. 2.1.

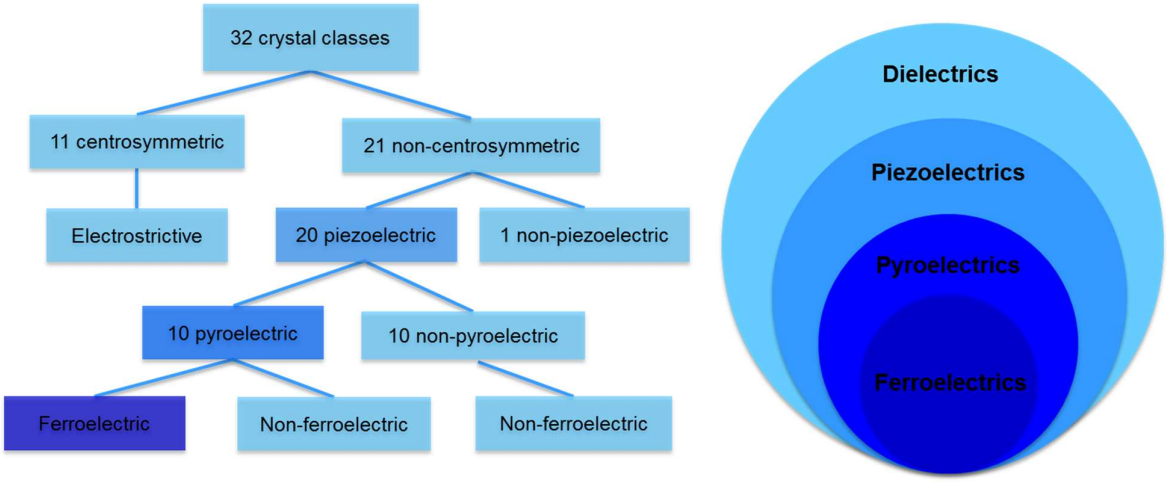

Figure 2.1 The relation chart showing crystal classes corresponding to piezoelectricity, pyroelectricity, ferroelectricity, and electrostricticity and their relationship.

2.1.1 Dielectricity

Dielectrics are insulating materials that can be polarized under an external electric field. Electrical charges of dielectric materials deviate from the equilibrium positions when placed in an electric fileld. Therefore, the centers of positive and negative charges are separated, leading to the formation of polarization dipoles. (Fig. 2.2).

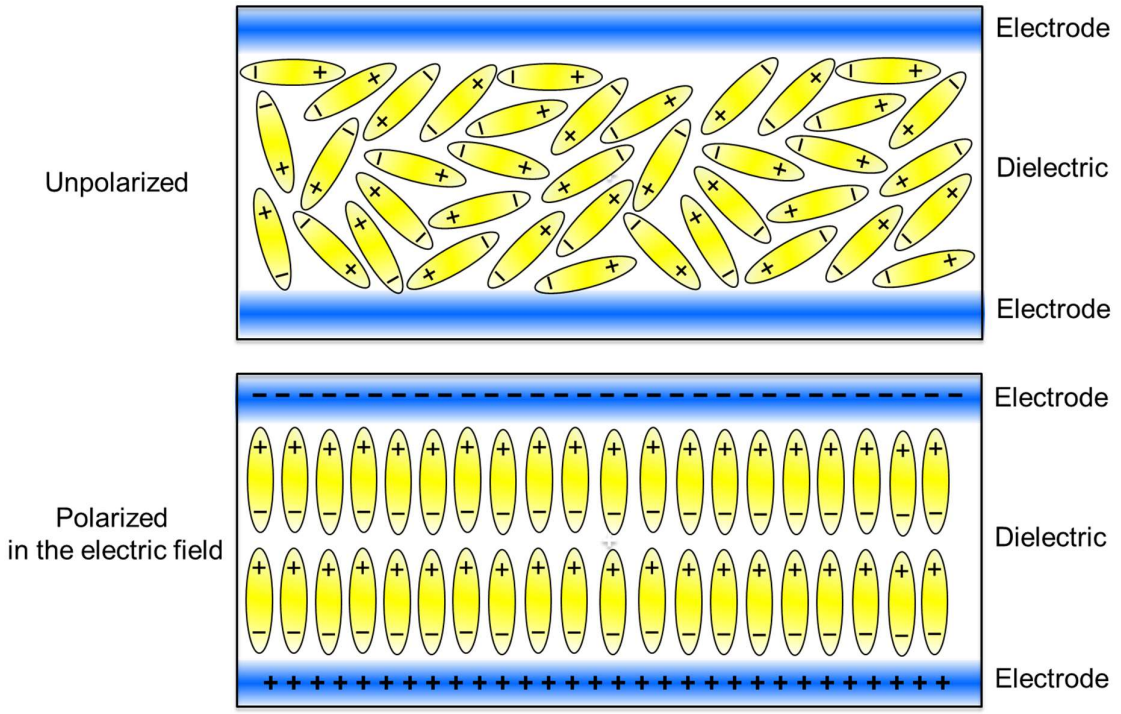

Figure 2.2 Sketch of a dielectric material placed in an external electric field: polarization-dipoles are formed.

The electric polarization (P) can be described as a dipole moment per unit volume and can be related to the electric field (E) through electrical susceptibility $\boldsymbol{\chi}$:

$$\boldsymbol{P} = \varepsilon_0 \cdot \chi \cdot \boldsymbol{E} \tag{2.1}$$

where $\boldsymbol{\varepsilon_0}$ is the electric permittivity of free space and equals $8.85 \cdot 10^{-12}$ F/m.

The electrical displacement D is given as:

$$\boldsymbol{D} = \varepsilon_0 E + P = \varepsilon_0 (1 + \chi)\boldsymbol{E} = \varepsilon_0 \varepsilon_r \boldsymbol{E} \tag{2.2}$$

where ε_r represents the relative permittivity (dielectric constant).

Electrostriction

Electrostriction is a basic electromechanical phenomenon that occurs in all insulators or dielectrics. It is present in all crystal symmetries because of a fourth rank polar tensor. In the same and opposite direction of the applied field, the electrostriction and anions occurs. Because of this, all dielectric materials exhibit a displacement of cations under the application of an electric field and thus resulting in a net elastic deformation of the material. The degree of deformation depends on the crystal class to which the material belongs. The resulting strain S is proportional to the square of electric field (E_i)/polarization (P_i), and it can be expressed in the following equations:

$$S_{ij} = Q_{ijkl} P_k P_l \tag{2.3}$$

$$S_{ij} = M_{ijkl}E_kE_l \tag{2.4}$$

where Q_{ijkl} and M_{ijkl} are electrostrictive coefficients.

2.1.2 Piezoelectricity

Crystallized material can be classified according to 32 crystal classes (Fig. 2.1). When the mechanical strain is applied to the crystal, polarization charges will appear since a crystal environment is composed of electrically charged particles. Certain classes of dielectrics exhibit a piezoelectric effect property. Such an effect can be observed only in non-centrosymmetric piezoelectric behavior.

Piezoelectricity was first discovered in certain crystals such as quartz, tourmaline, zinc blends, and Rochelle salt in 1880 by Pierre and Jacques Curie. [60, 64] When mechanical stress is applied to a material, electrical charges are generated because the crystal ions are shifted toward the opposite direction, forming an electrical field. It is known as the direct piezoelectric effect. The converse piezoelectric effect (CPE) describes a mechanical deformation resulting from an applied electrical field.

Direct (equation 2.5) and converse (equation 2.6) piezoelectric effects can be mathematically depicted in terms of tensor form:

$$P_i = d_{ijk}S_{jk} \tag{2.5}$$

$$S_{ij} = d_{ijk}E_k \tag{2.6}$$

where P_i is the polarization vector, d_{ijk} is the piezoelectric coefficient tensor, S_{jk} is the mechanical stress tensor, S_{ij} is the mechanical strain tensor and E_k is the electric field vector. The piezoelectric coefficient tensor limits the possible polarization direction because the nonzero elements of the piezoelectric coefficient tensor is related to the crystal symmetry.

Fig. 2.3 illustrates the direct (converse) piezoelectric effect. For the direct piezoelectric effect, when an external mechanical stress is applied to a piezoelectric material, a surface charge is generated, leading to a shifting of the negative and positive charge centers. The direction of the applied stress, i.e., compressive or tensile, decide the polarity of the formed surface charge. When applying an external electrical field to the piezoelectric material,, a deformation (contracts or expands) occurs, depending on the direction of the field. This is the converse piezoelectric effect.

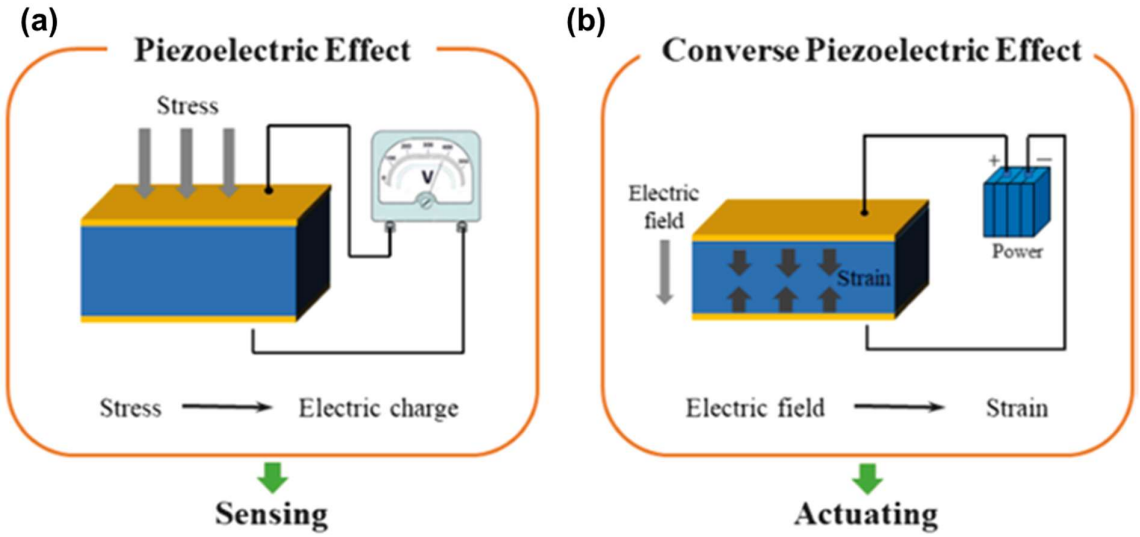

Figure 2.3 The schematic diagram of (a) direct piezoelectric effect, mechanical stress is applied to the crystal, and electric charges are induced; (b) converse piezoelectric effect, an electric field is applied to the piezoelectric material and thus induces the generation of the strain (Reprinted from Ref. [65] with the permission from Springer Nature. Permission license number: 5392990868708)

2.1.3 Ferroelectricity

Ferroelectrics are a subgroup of piezoelectrics and pyroelectrics. Ferroelectric materials are crystalline materials that exhibit spontaneous electrical polarizations, which can be switched by an external electric field. [66] The electric polarization is induced by the displacement of positive and negative charge centers. Hence, polarization switching consists of both displacements of atoms and the corresponding shift of charges. Typically, this polarization has at least two metastable equilibrium states or discrete stable states. Thus polarization dipoles can be switched from one state to another reversibly under the external electric field. [67] The crystal structure states are identical at any two orientation states. The only difference is the electric field polarization vector when the electric field is zero. The spontaneous polarization P_S is the polarization vector at zero electric fields. [61] In a ferroelectric material, regions where polarization vector with different orientations coexist, are called ferroelectric domains. As was mentioned before, the characteristics of domains and domain walls are bounded to macroscopic properties. By measuring the polarization loop as a function of the applied electric field, the change in domain orientation can be indirectly detected. The polarization as a function of the electric field is also called a "hysteresis loop (*P*-*E* loop)", which is a sign of the bulk ferroelectric. [68, 69]

In 1921, P. Curie found the ferroelectric phenomenon in the Rochelle salt single crystal.[70] Since the discovery of ferroelectricity in $BaTiO_3$ in 1949 [71], the sy of ferroelectricity has reached a turning point. $BaTiO_3$ was the first recognized ferroelectric whose structure is perovskite and the crystal structure is much simpler. After that, more and more ABO_3 perovskite-type compounds have been developed and extensively reviewed for ferroelectric properties. The ferroelectricity merely occurs in

the ferroelectric crystal at temperatures below the Curie temperature T_C, where the material experiences a phase transition. This phase transition changes from the paraelectric state to the ferroelectric state, which can be characterized by a normal dielectric behavior above T_C and a reversible spontaneous polarization below T_C, respectively. [7]

In the following section, the perovskite structure, the critical physical properties, domain and domain walls, as well as the temperature-dependent phase transition, are introduced.

Perovskite Ferroelectrics

The natural mineral perovskite ($CaTiO_3$) was discovered by Gustav Rose in 1839 and named after Russian mineralogist Lev Aleksevich von Perovski. [72] The perovskite oxides' chemical formula is ABO_3, where A-site cation correspond to divalent alkali earth or trivalent rare earth metal, B-site cation is a transition metal with partly filled d-orbitals. For a typical cubic perovskite, A-site cations, the smaller B-site cations and the oxygen ions are located at the corners of the cube, the body-centered position and face-centered position, respectively. A-site cations are surrounded by 12 anions, while B-site cations are octahedrally coordinated by 6 anions, as illustrated in Fig. 2.4.

Owing to the lattice distortions caused by different instabilities, most of the perovskite oxides are not the ideal cubic structure. The size of the A-site and B-site cations was considered to understand the symmetry-lowering distortions better. Typically, A-site cation (*e.g.*, Na^+, Ba^{2+} or Bi^{3+}) has the valence from +1 to +3 and B-site cation (*e.g.*, Ti^{4+}) has the valence from +3 to +6. The Goldschmidt tolerance factor (t) is often employed to predict how much the perovskite structure deforms from a cubic structure [73]:

$$t = \frac{R_A + R_O}{\sqrt{2}(R_B + R_O)} \tag{2.7}$$

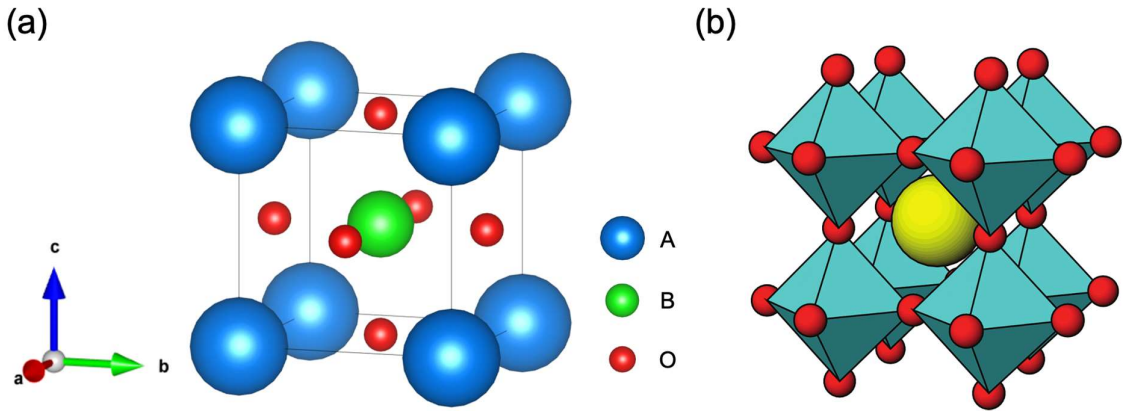

Figure 2.4 (a) Ideal cubic perovskite structure for ABO_3. (b) the perovskite framework (cyan, BO_6 units; yellow, A atoms). A atoms are in the center, BO_6 octahedra are in the corner (Reprinted with permission from Ref. [74]. Copyright (2012) American Chemical Society)

where R_A, R_B, and R_O represent the radii of A and B cation and O anion. A typical tolerance factor is in the range of $0.95 < t < 1.06$. If $t = 1$, the structure is stabilized in the cubic phase so that B cation has no space to move. When $t > 1$, B ion is very small for the BO_6 octahedra (oxygen octahedra). Thus, the B cation is free to move-off center, leading to a slight polar distortion, *e.g.,* as for $BaTiO_3$. This kind of material is termed B-site driven. When $t < 1$, the materials are rarely ferroelectric, called A-site driven materials. The larger B cation favors the oxygen octahedron's rotation and tilt, whereas the smaller A atom can not be effectively bonded to all 12 adjacent oxygen ions.

For example, Ba^{2+} and Ti^{4+} in barium titanate $BaTiO_3$ occupy the corner (A) and the center (B) of the cubic unit cell, respectively (Fig. 2.5). The O^{2-} lies at the face center, forming TO_6 oxygen octahedron. The shift of Ti^{4+} and O^{2-} ions leads to the electric dipole and further induces the appearance of spontaneous polarization P_s. The dimensions of the unit cell change, followed by the appearance of spontaneous polarization. The cubic phase of $BaTiO_3$ is the centrosymmetric crystal class, meaning that the center of positive charges (Ba^{2+} and Ti^{4+}) coincides with the center of negative charges (O^{2-}), which leads to a zero spontaneous polarization P_s. When the phase translates from cubic to lower symmetry ferroelectric phases, P_s will change and be non-zero. At ambient pressure, $BaTiO_3$ goes through a sequence of first-order phase transitions when cooled: cubic $\xrightarrow{\sim 131^\circ C}$ tetragonal $\xrightarrow{\sim 0^\circ C}$

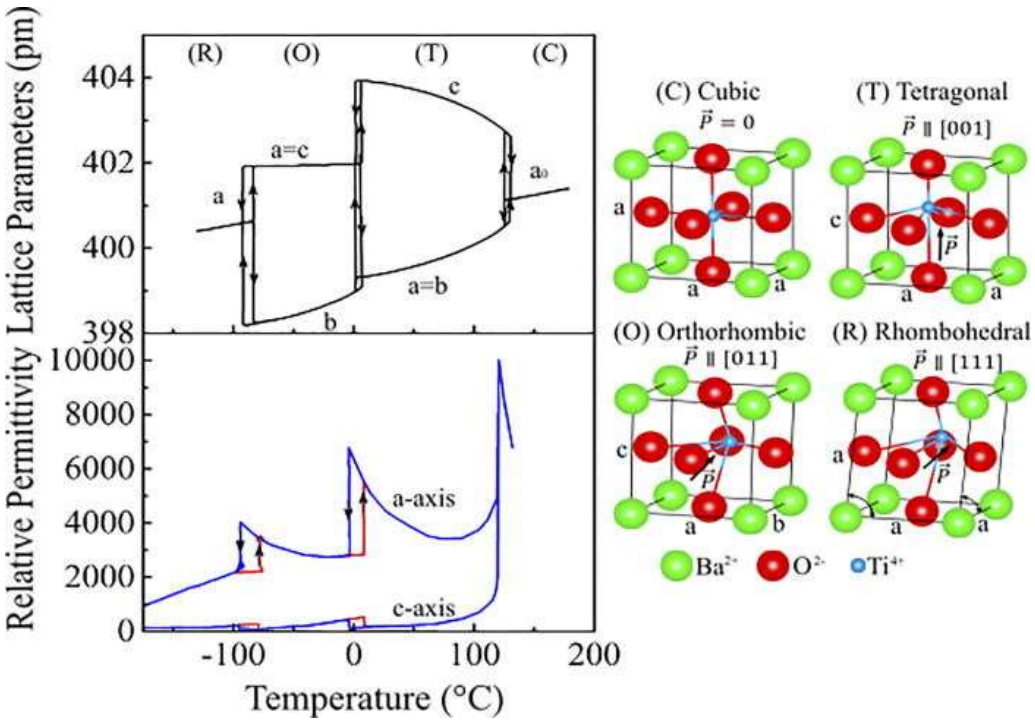

Figure 2.5 The left-side panel shows changes in primitive-cell lattice parameters and anomalies in relative permittivity with the temperature change during the phase transitions in $BaTiO_3$. The right-side one demonstrates the crystal structure of the cubic prototype phase and the unit cell distortions in tetragonal, orthorhombic, and rhombohedral ferroelectric phases of $BaTiO_3$. (Reprinted from Ref. [75], with the permission of AIP Publishing. Permission license number: 5412681031759)

orthorhombic $\xrightarrow{\sim -90°C}$rhombohedral. [76] These transitions are related to the appearance of P_s. Cooling down to Curie temperature (for $BaTiO_3$, $T_C \approx 131$ ℃), the phase transition from cubic symmetry to a tetragonal distortion can lead to a shape change of the unit cell. The off-center shift of Ti^{4+} and O^{2-} relative to Ba^{2+} is shown in Fig. 2.5. The corresponding spontaneous polarization is directed parallel to the edge of the perovskite structure's pseudocubic unit cell (along the c-axis). When further cooling down, the electric dipoles will realign along a face diagonal in the orthorhombic phase and a body diagonal in the rhombohedral phase. While external stimuli, e.g., an electric field and mechanical stress, are removed, the polarization direction will be along crystallographic directions with the lowest free energy. For example, the polarization vector for BT in the tetragonal (*P*4*mm*) phase could be along any of the six equivalent <100> directions. As illustrated in the relative permittivity, three distinct maxima indicate strong dielectric softening during the transitions between phases.

Ferroelectric Domains and Domain Walls

The electric dipoles in the ferroelectric material are usually not oriented in the same direction throughout the whole material. Instead, they are usually aligned along several possible directions. During the temperature-induced ferroelectric phase transition, spontaneous polarization has the equal possibility of being in any of the possible directions. The ferroelectric regions where the electric dipoles are aligned are referred to as ferroelectric domains. Ferroelectric domains generate to minimize the elastic energy associated with mechanical constraints and electrostatic energies of depolarizing fields of the system. [77-79] To minimize the electrostatic and elastic energy, the different orientated domains are separated by the boundaries or regions with a width of about several lattice constants. The boundary that separates the two domains is known as the domain walls (DW). [80] The strong coupling between the polarization and the strain influence the energy of the domain wall. For this reason, the polarization reversal takes place on a much smaller scale of several unit cells. In ferroelectrics, DW significantly influences their optical, electromechanical, magnetic, and electrical properties.

Domain walls presented in ferroelectric materials are classified into two types. Depending on the orientations of spontaneous polarization are antiparallel or perpendicular (for 90°), 180° and non-180° ferroelectric domain walls occur. The walls separating domains differ in orientation by 180° rotations are described as 180° domain walls, whereas the walls separating domains with polar vectors oriented by non-180° rotations are called non-180° domain walls. For orthorhombic (*Amm*2) symmetry, the allowed domains are 60°, 90°, 120°, and 180°, the allowed domains for the rhombohedral (*R*3*m*) symmetry are 71°, 109°, and 180°. [81] Figure 2.6(a) illustrates the formation mechanisms of 180° and 90° domain walls for the tetragonal symmetry. Both 90° and 180° domain walls weaken the effects of depolarizing electric fields (electrostatic energy) associated with surface charges. Nevertheless, only the formation of 90° domain walls minimizes the elastic energy. [69, 82, 83] Domain walls that differ in orientation to the spontaneous polarization vector and the spontaneous strain tensor are called

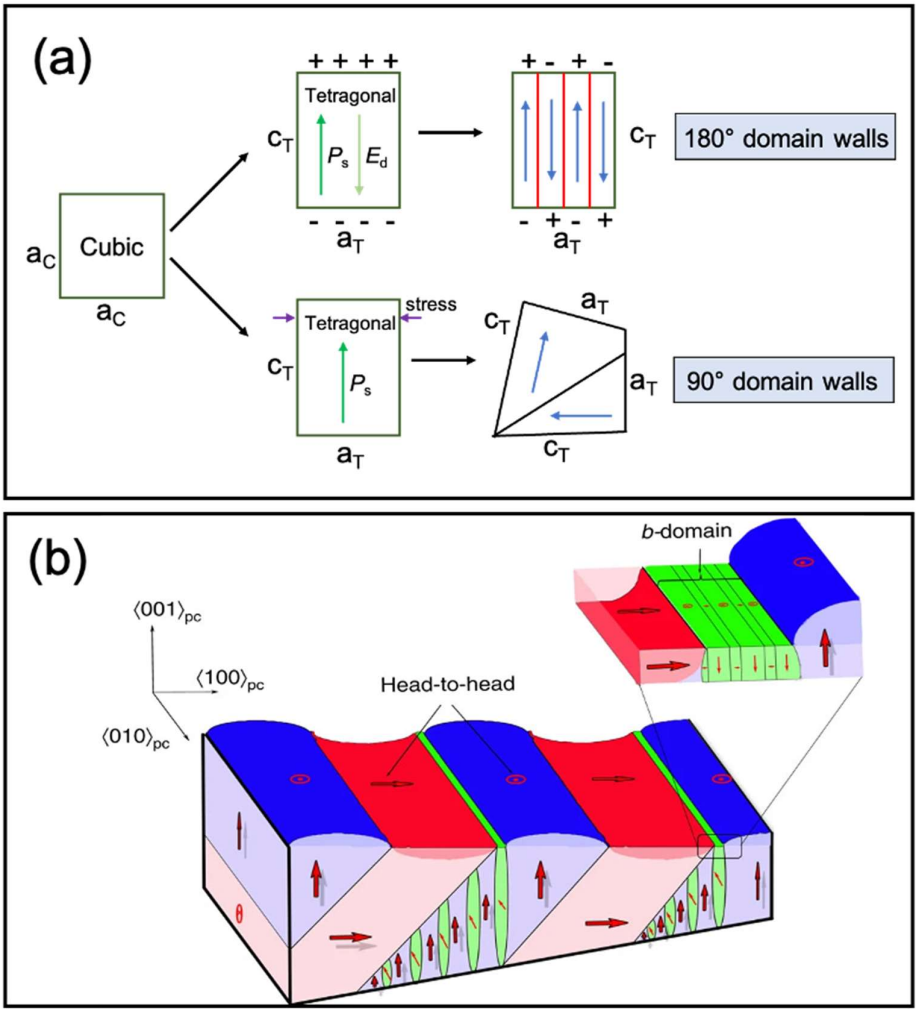

Figure 2.6 (a) Schematic diagram for forming 180° and 90° ferroelectric domain walls in a tetragonal symmetry. (b) Schematic illustration of the domain structure in tetragonal BT, built by combining the AFM and Raman mapping results. a, b, and c domains are in red, green, and blue color, respectively (from Ref. [84])

ferroelectric domain walls and ferroelastic domain walls, respectively. Ferroelastic domains have no 180° domain walls, while ferroelectric domains have both 180° walls and 90° walls. As a material is cooled through Tc, both the electric and elastic boundary conditions are combined, inducing a complicated domain structure composed of 180° and 90° domain walls. Figure 2.6(b) shows the sketch of BT's domain structure based on AFM and Ramen results. Both 180° and 90° domain walls are presented. Head-to-head domain walls process high internal stress so that b-domains emerge to minimize internal stress. A lot of factors can impact the virgin domain pattern, such as magnies of spontaneous polarization, history of the crystal preparation and sample geometry, electrical conductivity, elastic and dielectric compliances, defect structure, and crystal symmetry. [85]

The ferroelectric and strain hysteresis loops is promoted by the dissemination and switching of domains. The characterization of the polarization and strain hysteresis loop will be affected by the new formatted domain and the movement of domain walls. The displacement of domain walls under weak

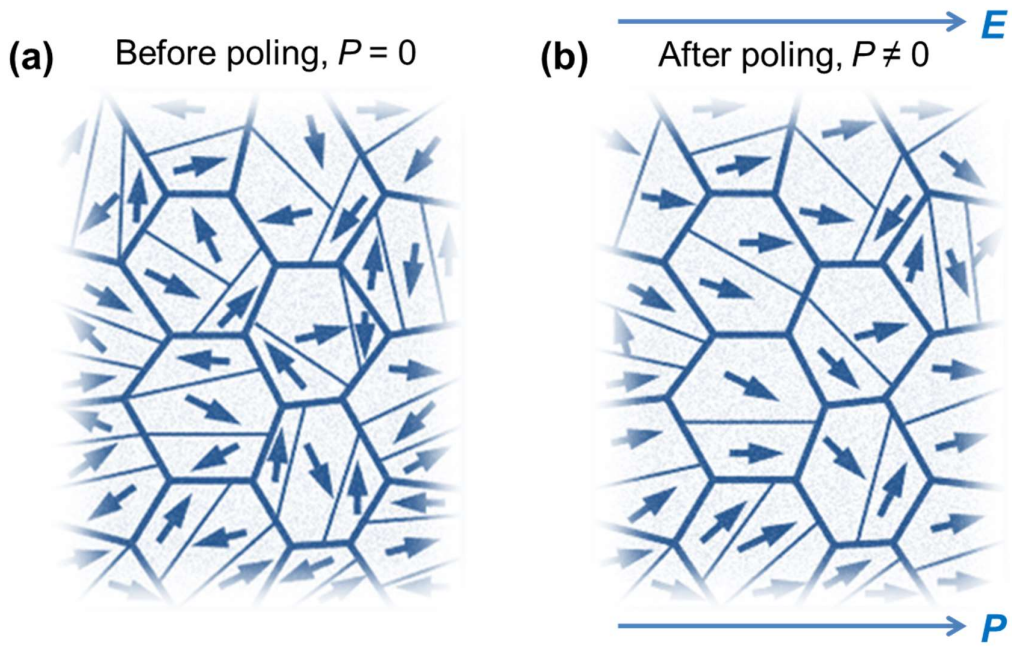

Figure 2.7 Randomly orientated grains in a polycrystalline ferroelectric before (a) and after (b) poling. Many domain walls are still present after the poling process; nevertheless, the net remanent polarization P_r is nonzero.

or moderate external fields significantly influences the piezoelectric, mechanical, and electrical properties of ferroelectric materials. Furthermore, slight displacements of all types of domain walls affect the ferroelectric properties of materials. For non-180° walls, the piezoelectric effect can be directly promoted in addition to polarization change. [86] The movement of domain walls at weak to moderate external fields is one of the most critical extrinsic (nonlattice) contributions to the piezoelectric, elastic, and dielectric properties of ferroelectric materials [86-90] and may be comparable to the lattice's intrinsic effect [91].

Poling

As illustrated in Fig. 2.7 (a), many domains and domain walls exist in the grains due to the complicated electric and elastic boundary conditions between grains in ferroelectric materials. As mentioned before, the spontaneous polarization in the ferroelectric material is usually randomly oriented throughout the material and hence leads to a zero net polarization $P_s = 0$. Consequently, the macroscopic properties, such as piezoelectric and pyroelectric effects, will offset and can not be observed. This is the so-called 'virgin' ferroelectric state (before poling). Such material is neither piezoelectric nor pyroelectric. Ferroelectric materials may be induced into a poled state under a strong external electric field (usually at 10-100 kV cm^{-1}). And the process is normally achieved at elevated temperature. In this state, the electric dipoles within individual grains tend to rotate toward the direction of the applied electric field. This process is called poling or the switching process of the ferroelectric domains under the external electric field, and grains cannot be oriented during the

process. Thus, macroscopic piezoelectric and pyroelectric properties can be unveiled in the poled ferroelectric state, even though many domain walls are still present, as shown in Fig. 2.7 (b). The polarization reversal by a field poling process can only be achieved in ferroelectric materials. A state that does not contain domains in a single crystal is called to be in a single-domain state and can be gained by poling.

It is widely recognized that temperature plays a significant role in poling. Exposing the ferroelectric material to the same external electric field, poling at a high temperature can help stimulate a higher fraction of domain reorientations because the lattice distortion decreases and the coercive field is reduced, thus leading to the improvement of piezoelectric properties. [92, 93] Apart from the poling-induced domain reorientations, defect charge carriers may rearrange near the domain boundaries and an internal bias field may also form. The formed internal bias field is often apparent in the resulting asymmetry of strain versus field (*S*–*E*) loops and polarization versus field (*P*–*E*) loops.

Hysteresis Loops

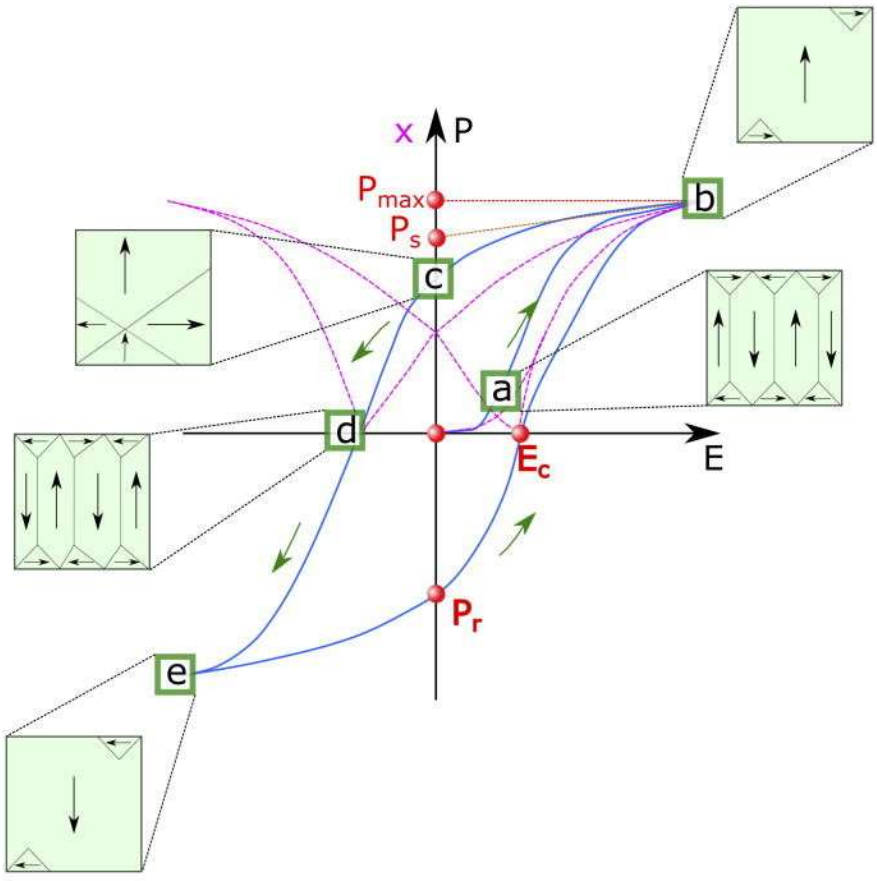

Figure 2.8 Ferroelectric polarization versus electric field hysteresis loop (*P*-*E* loop) (blue line). (a), (b), (c), (d), and (e) represent the domain orientation at the indicated fields. The strain-electric field butterfly loop (pink line) is also shown. (Reprinted from Ref. [75], with the permission of AIP Publishing. Permission license number: 5412681031759)

The switch of the domain from different states can be studied by indirect measurement. As illustrated schematically in Fig. 2.8 (blue line), the ferroelectric hysteresis loop (P-E loop) describes the polarization as a function of an applied electric field.[68, 69]. Macroscopically, the sample has randomly aligned multiple domains and compensates for each other, and the polarization P will be zero without any external electric field at the origin state. In Fig. 2.8 (a), the domains in a ferroelectric material are randomly oriented at the pristine state and the macroscopic polarization P is zero. As an external electric field is applied, the polarization switching can be attributed to the motion of the domain walls, which can induce the reorientation of domains and lead to domain nucleation and growth. Because of the intrinsic material response, the polarization increases nearly linearly with the applied electric field at low electric fields. If the external stimulus, such as an electric field or mechanical stress, is large enough, domain walls can be displaced, giving rise to domain switching. This is the extrinsic process. P-E loop appears due to the induced domain switching and the polarization also nonlinearly increases with the applied electric field (Fig. 2.8).

There are reversible and irreversible domain-wall motions, depending on the distribution of the local lattice energy potential generated by lattice defects. [69, 90] For the reversible domain wall motion, the domain wall will move around a local energy minimum and vibrate around an equilibrium position, which means that the ferroelectric domain orientations can not be changed under the small applied electric fields [94], and the domain wall can move back to its initial location when switching off the external electric field [95]. It happens only at a low electric field. By further increasing the applied electric field, the domain wall has enough energy to overcome the adjacent potential barriers and thus can jump between local energy minima. [96] The total polarization reaches a saturation value and can be further improved by dielectric charging with a further enhanced field (P_{max}). Owing to the irreversible motion of the domain walls, the system's polarization increases non-linearly as the applied electric field is enhanced. The switchable domains are all aligned at a very high electric field, reaching a saturation state. The polarization non-linearly increases with the applied electric field [Fig. 2.8(b)]. Via extrapolating the linear portion near the saturation polarization along the saturation polarization target, the intersection with the polarization axis (or zero-field axis) is the spontaneous polarization P_s. When the field is reduced, some domains will switch back as a response to local electric and mechanical fields. After removing the field (at zero fields), the polarization is non-zero and called remanent polarization P_r. The macroscopic remanent polarization P_r is caused by irreversible domain switching [Fig. 2.8(c)]. When the field increases in the opposite direction, the polarization will decrease and restore to zero if the field reaches a sufficient value. The electric field when the polarization is reduced to zero is named the coercive field E_c. The domains are again randomly oriented, and no net polarization can be measured [Fig. 2.8(d)]. As the electric field is further at opposite positions, domains are all aligned again, thereby, the polarization saturates [Fig. 2.8(e)]. Therefore, the ferroelectric hysteresis loop (P-E loop) is originated from the domain's reversible and irreversible switching.

A strain-electric field hysteresis loop (the S-E hysteresis loop) is obtained, accompanied by the reverse of the domain and re-orientation of P_s, which resembles the shape of a butterfly (Fig. 2.8 pink line). The strain-field hysteresis generates because of the existence of the converse piezoelectric effect and the electrostriction in ferroelectrics.

2.2 Bismuth Sodium Titanate $Na_{1/2}Bi_{1/2}TiO_3$-based Lead-free Ferroelectric Ceramics

Discovered by Smolenskii *et al.* in 1961 [97, 98], bismuth sodium titanate $Na_{1/2}Bi_{1/2}TiO_3$ (NBT) is a well-known relaxor ferroelectric material. It has the ABO_3 perovskite structure, where Bi^{3+} and Na^+ cations are located at the A-sites and the B-sites are Ti^{4+} cations. Like the La-doped lead zirconium titanate (PLZT)- and $Pb(Mg_{1/2}Nb_{2/3})O_3$ (PMN), the A-site disorder leads to the relaxor behavior in NBT at room temperature. [99-101] It exhibits a strong frequency dispersion of the dielectric permittivity at T_m (approximately at 340°C) and the depolarization temperature is about 185°C. [102, 103] NBT has a rhombohedral $R3c$ structure [104], which is stable from -268 to 255°C [105]. The characteristic phase transition from the cubic ($Pm\bar{3}m$) to the tetragonal ($P4bm$) occurs at approximately 540°C and tetragonal to rhombohedral symmetry ($R3c$) arises at ca. 300 °C. [102, 103] As the temperature is increased, the cubic structure with $Pm\bar{3}m$ symmetry transforms to the tetragonal phase at ca. 540°C. tetragonal and cubic phases coexist in the temperature range from 500ºC to 540ºC. The pure tetragonal phase exists at temperatures ranging from 400ºC to 500ºC. [105], a rhombohedral and tetragonal phases coexist between 255 ºC and 400 ºC. The Curie temperature reported for the NBT system is about 320°C. [106, 107] The tetragonal phase is considered to be ferroelastic [108] or super paraelectric above the Curie temperature [109]. At 540ºC, the tetragonal phase transforms to the paraelectric cubic phase [107].

At room temperature, the piezoelectric constant and remanent polarization of NBT is 73 pC/N and 38 $\mu C/cm^2$ respectively. The high Curie temperature and good electromechanical properties making NBT system an appropriate substitute for lead-containing material systems like PZT. [19, 105, 110, 111] However, a high coercive field (Ec = 7.3 kV/mm) is induced by the low polarizability of NBT, makes an limition of the application in many fields. [112-114] [19, 115] Thus, the modified NBT using other perovskite materials became increasingly important, where especially the morphotropic phase boundary (MPB)-based composition that has been intensively studied because of its excellent electromechanical properties, e.g., the sizeable normalized strain (S_{max}/E_{max}) of > 500 pm/V. [19, 116-119] The electric field-induced output strength even surpasses one of the PZT-based counterparts. [12, 115]

NBT-based systems have been identified to exhibit a pseudo-cubic symmetry and feature the relaxor behavior macroscopically. The polar nanoregions in NBT-based relaxors are suggested to be embedded into the cubic matrix, which plays a crucial role in the field- and temperature-dependent

Table 2. 1 Properties of NBT–*x*BT piezoceramics.

Parameter	Xu et al. [120]	Xu et al. [121]	Chu et al. [122]	Chen et al. [123]	Takenaka et al. [124]	unit
composition *x*	0.06	0.06	0.06	0.07	0.06	
coupling	k_p=0.367	k_p=0.28	k_p=0.29	k_p=0.26	k_{33}=0.55	
E_c	3.41	4.27	2.88	2.72	n/a	$kV \cdot mm^{-1}$
P_{rem}	0.388	0.37	0.4	0.378	0.2	$C \cdot m^{-2}$
T_d	129	n/a	100	87	150	°C
T_m	225	n/a	240	290	242	°C
d_{33}	122	180	176	155	110	$pC \cdot N^{-1}$

evolution of electrical properties. [117, 118, 125-128] It was suggested that the origin of the large electromechanical response in NBT-based piezoceramics is attributed to the reversible transition from an ergodic relaxor state to a ferroelectric state and irreversible transition from a non-ergodic relaxor state to a ferroelectric state upon the application of a sufficiently large external electric field. [8, 118, 129-131]

Numerous NBT-based systems have been reported and developed to improve their functional properties. [19, 132, 133] Among them, $(Na_{1/2}Bi_{1/2})TiO_3$–*x*$BaTiO_3$ (NBT–*x*BT) obtained more and more attention since the report by Takenaka et al. [19] Due to its outstanding piezoelectric properties and ease of processing, NBT–*x*BT has been one of the most promising NBT-based systems. [12] According to the phase diagram of NBT–*x*BT, rhombohedral and tetragonal phases coexist at 6 ~ 7 mol % BT, forming displays an MPB condition. [19] Similar to the properties of PZT, the NBT–*x*BT has optimal performance close to the MPB region. For example, coupling factor (k_{33}) is 0.55, the piezoelectric constant and remanent polarization is up to 180 pC/N and 38.8 μC/cm^2 respectively. [19, 20, 110, 121-123, 134] Nevertheless, the applitation of the NBT–BT system is limited by the low depolarization temperature (T_d). [135, 136] An overview of the properties of NBT – *x*BT solid solution is shown in Table 2.1. [137]

2.3 $Ba(Zr_{0.2}Ti_{0.8})O_3$-*x*$(Ba_{0.7}Ca_{0.3})TiO_3$ Lead-free Ferroelectric Ceramics

Lead-free $Ba(Zr_{0.2}Ti_{0.8})O_3$-*x*$(Ba_{0.7}Ca_{0.3})TiO_3$ (BZT-*x*BCT) solid solution has received more and more attention as a replacement for lead-contained piezoelectric materials in recent years due to its outstanding dielectric and electromechanical properties. [138-144] The BZT–*x*BCT system exhibit a perovskite structure, where Ba^{2+} ions on A-sites are substituted by Ca^{2+} ions and Zr^{4+} ions substitute Ti^{4+} ions on B-sites. An exciting point for BZT-*x*BCT system is that the polymorphic phase transition (PPT) composition BZT-0.5BCT, pioneered by Liu and Ren [145], processes a high piezoelectric coefficient (d_{33} = 620 pC/N), which is even higher than soft PZT. [145] Its piezoelectric, dielectric,

ferroelectric properties [146-150], optical, elastic, microstructural features [142, 151-153], phase transitions [42, 140, 154], etc. have been widely studied.

Based on the measurements of temperature-dependent dielectric permittivity and X-Ray diffraction, the composition-temperature phase diagram of the BZT–*x*BCT system was made by Liu and Ren (Fig. 2.9(a)). [145] There exist 3 phases, including a paraelectric cubic (C) (space group Pm3m), ferroelectric tetragonal (T) (space group P4mm), and ferroelectric rhombohedral (R) (space group R3m). Depending on the composition, the paraelectric C phase becomes stable above Curie temperature (usually ranging from 0 to 100 °C). If $x < 0.32$, the BZT–*x*BCT only goes through a single phase transition from the paraelectric cubic to ferroelectric rhombohedral phase as the temperature decrease. If $x > 0.32$, a new ferroelectric phase (tetragonal phase) occurs during the change of temperature. Hence, as the temperature decrease, two phase transitions, C → T and T → R can be observed. (Fig. 2.9 (a)). Two ferroelectric phases separated by the morphotropic phase boundary (MPB) are extremely sensitive to the temperature. To describe more precisely, the phase transition is named a polymorphic phase transition (PPT). The triple point locates at $x \sim 0.32$ and at $T \sim 57$ °C, where the paraelectric C phase coexists with ferroelectric R and T phases. [145] It should be noted that the C – R – T triple point was also observed for high-performance lead-based systems such as PZT and $Pb(Zn_{1/3}Nb_{2/3})O_3$–$PbTiO_3$ (PZN–PT).[155] The high piezoelectricity in the BZT–*x*BCT is generally considered to be induced by the enhanced polarization rotation around the triple point. The energy barrier between C, R, and T phases is low enough so that enables enhanced polarization rotation around the triple point. However, compared with the phase diagram initially reported by Liu and Ren, it is much more complex in the BZT-*x*BCT system, according to recent studies. [140, 143, 156]

Many peer investigations have proved the phase diagram proposed by Liu and Ren. [150, 156] Nevertheless, many studies found that R and T phases coexist around the PPT region. [154, 157, 158] This point was evidenced by experimental observations such as Raman, thermally stimulated depolarization currents and elastic and dielectric properties. [157, 159, 160] The temperature-dependent in situ X-Ray diffraction technique studies demonstrate R, T, and possibly C phases coexist over a considerable temperature and composition range, as depicted in Fig. 2.9 (b). [154] More recently, based on their high-resolution synchrotron X-ray powder diffraction studies, Keeble et al. reported a phase diagram that an intermediate orthorhombic (O) phase (space group Amm2) emerges between the R and T phases (Fig. 2.9 (c)). [144] Hence, the phase transitions R → T → C is refined into R → O → T → C as the temperature increase, which is consistent with that of the $BaTiO_3$ system. [144] Instead of a triple point [145], a phase convergence region was detected, where R, T, O, and C phases are hardly distinguished with experimental methods. [144] As further confirmed by Tian et al. [161] and Zhang et al. [162], the O phase acts as a bridging phase in a narrow region between R and T phases.

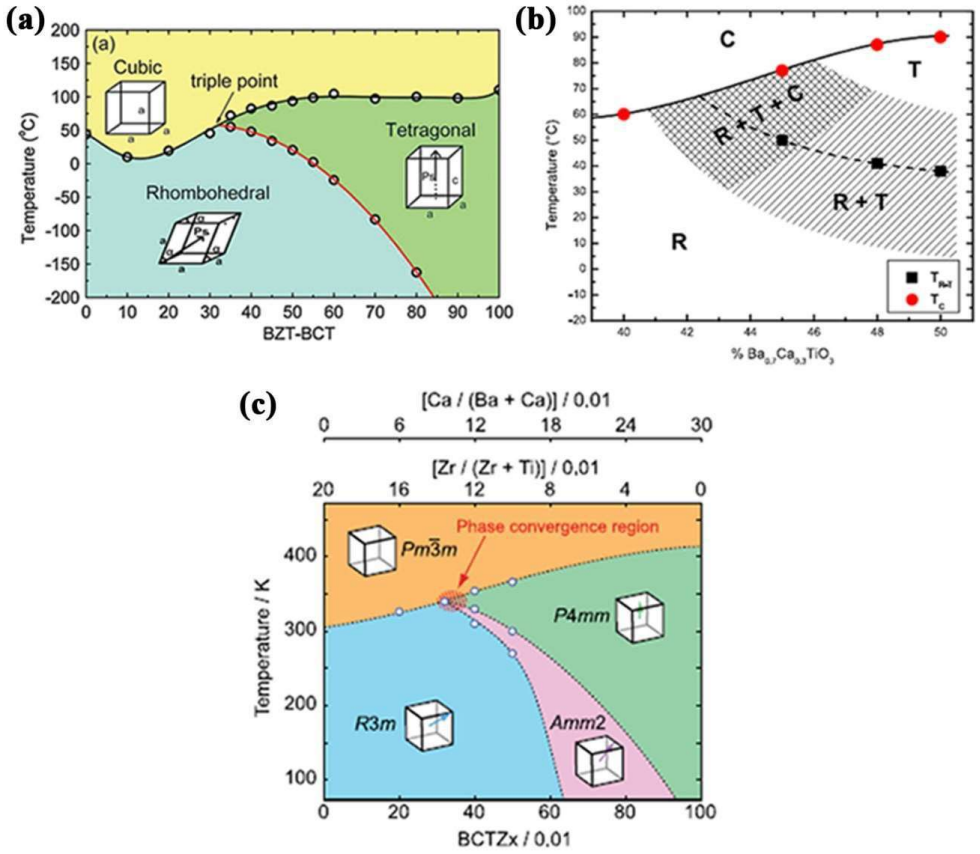

Figure 2.9 (a) Composition – temperature phase diagram of BZT-*x*BCT system reported by Liu and Ren. (Reprinted with permission from Ref. [145]. Copy right (2009) by the American Physical Society. Permission license number: RNP/22/OCT/059050) (b) Phase diagram of BZT-xBCT system close to the PPT reported by Ehmke et al. (Reprinted from [154], with the permission of AIP Publishing. Permission license number: 5453541421109) (c) Revised phase diagram of BZT-xBCT reported by Keeble et al. (Reprinted from [144], with the permission of AIP Publishing. Permission license number: 5453541015526).

2.4 Atomic Force Microscopy

Shortly after Binnig and Rohrer's invention of SPM in 1982 [163], AFM was developed in 1986, which is part of local probe microscopy techniques. Unlike SPM, which mainly depends on measuring the tunneling current between the sample and the tip, AFM is normally based on the measurement of short-range forces between tip and sample surface, such as capillary forces and Van der Waals (VDW) force. AFM can be widely used on many materials, primarily used to measure the surface topography in the precision of nanoscale. Furthermore, more surface properties, such as surface potential, and electrical and magnetic properties, can also be measured in the resolution of the nanoscale. AFM techniques are helpful in many research fields considering their wide range of applications.

AFM is based on a probe with a sharp tip attached to a flexible cantilever's end. The radius of curvature for the tip is on the order of nanometers (generally 10-20 nm). This allows AFM can

achieve high spatial resolution. Typically, the order of the resolution in the Z direction is sub-nanometer. Lateral resolution can also be a few tens of nanometers, which is limited by the tip radius of curvature. When the tip approaches the surface, the cantilever's vertical deflection is closely related to the force of the tip-sample surface. The force acting between the tip and surface can be described by Hooke's law, expressed as $F = -kz$, where F is the force, k the spring constant, and z is the deflection of the cantilever. Figure 2.10 (a) shows the total forces work between the sample surface and the tip. As presented in Fig. 2.10 (b), if the tip-sample distance is large enough (d >10 nm), nearly no force can be detected, and the cantilever will have no deflection in this case. When the tip approaches the sample surface (0.1 nm< d <10 nm), the tip-sample surface interaction is mainly attractive (mostly Van der Waals) force, as shown in Fig. 2.10 (c). In case the tip moves further approach to the sample surface (d < 0.1 nm), as illustrated in Fig. 2.10 (d), Pauli forces become sufficiently large, and thus the total interaction becomes repulsive.

Typically, the cantilever's deflection is detected by the laser beam on its back, and the laser is then reflected into a four-quadrant photosensitive detector. A column of piezoelectric material is used to support the sample in order to position the tip/cantilever (or sample) in the lateral (x, y) and vertical (z)

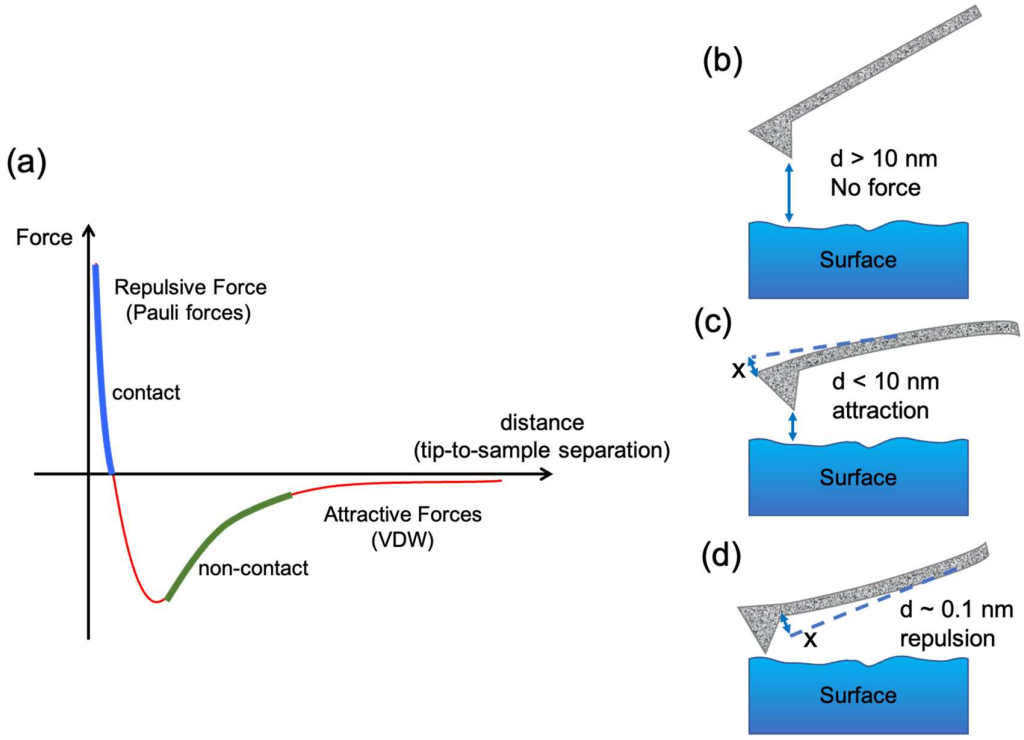

Figure 2.10 (a) Typical total force interaction between the AFM tip and the sample surface (b) For the distance large enough (d >10 nm), the force between the tip and sample is negligible, and the cantilever has no deflection (c) For intermediate (0.1 nm< d <10 nm) distances, the cantilever is pulled towards the sample, it is in an attractive regime (d). For a very short (d < 0.1 nm) distance, the cantilever is in hard contact with the surface, it is in a repulsive regime.

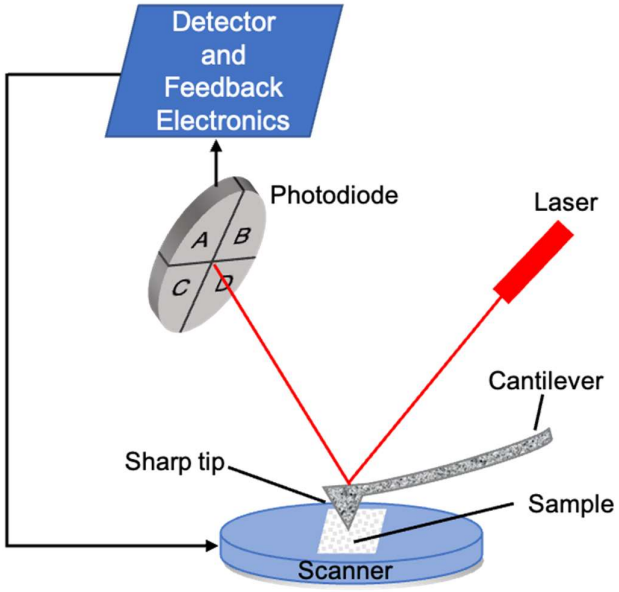

Figure 2.11 Schematic illustrating the basic principle of atomic force microscopy.

directions. By using a feedback loop, the sample-tip interaction keeps constant when the tip is scanned over the sample surface. During this process, the cantilever vertical deflection is set to be the feedback parameter while the desired "setpoint" value is got from the tip-sample distance. In the feedback loop, the tip-surface distance or the contact force maintains constant depending on the scanning mode employed. The topography of the scanned region can be obtained by moving the tip up and down. A schematic illustration of the basic principle of AFM can be seen in Fig. 2.11.

Three standard operation modes are manipulated in AFM depending on the distance between the tip and the sample. In non-contact mode, also called frequency modulation (FM), the force between the tip and sample surface is maintained in an attractive regime without any friction force and changed with the alter of the tip-sample distance, thus induced to a change in oscillation resonance frequency. In this mode, the deflection of the cantilever may be too small to detect because of the relatively small interaction force. Moreover, significant artifacts can be caused due to surface contamination. For this reason, there are many limitations to using non-contact AFM mode. In contact mode, the force between the AFM tip and sample surface keeps in a regime of repulsive. In order to define contact, the vertical deflection setpoint is opted. The vertical extension of the piezoelectric column (modified by applied voltages) was continuously adjusted by the feedback loop to keep the vertical deflection

constant. And this is directly related to the topography. In this mode, soft samples are not preferred due to the high friction forces. In intermittent contact or tapping mode, also referred to as amplitude modulation (AM), the cantilever mechanically oscillates between the repulsive and attractive force regimes, leading to a change in oscillation amplitude. In this mode, the advantages of contact and non-contact modes are combined.

2.5 Piezoresponse Force Microscopy

2.5.1 Principle of Piezoresponse Force Microscopy

Under the application of an external electric field, piezoresponse force microscopy (PFM) allows to image and control of ferroelectric domains without destruction, extending the functionality of the contact-mode AFM technique. [164] Güthner, and Dransfeld et al. pioneered the invention and first implementation of PFM in 1992. [165] PFM has attracted much interest and has become popular because of the increasing need for microscopic insights into the physical mechanisms behind the working principle of these materials. [46, 166-168] PFM can be used in various fields, including ferroelectrics, semiconductors, and biology. [169] PFM is a non-destructive method with a high resolution and the possibility to measure the local piezoelectric effect in complex geometries. It can also simultaneously acquire the topography and piezoelectric response.

The basic idea of PFM was to tactilely scan a nanometer-sized conductive probe over the surface of ferroelectric materials to detect the local polarization of ferroelectric samples [164, 170-172], as shown in Fig. 2.12. Owing to the converse piezoelectric effect (CPE), the sample deforms (contract or expand) under an alternating current (AC) bias applied to the probe tip, inducing a deflection of the PFM cantilever. An equipped standard split photodiode detector measures the amplitude and phase of the cantilever deflection, converting the oscillating surface displacement into an oscillating voltage signal. The surface deformation details can then be acquired using a lock-in amplifier (LiA) which can demodulate the oscillating voltage signal obtained before. Hence, nanometer resolution of surface topography and ferroelectric domain structures can be obtained simultaneously.

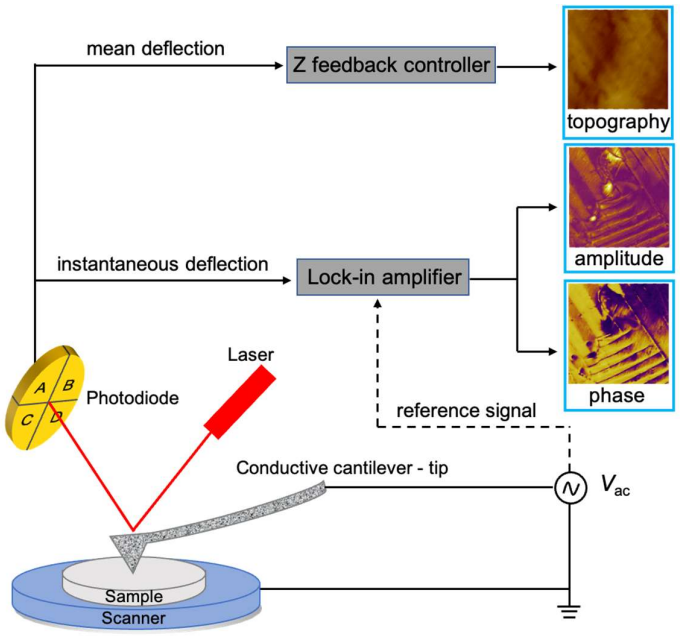

Figure 2.12 Schematic illustrating the operating principle of PFM.

Considering the magnie of the CPE is usually very small, the electromechanical response to an applied direct current (DC) field is generally on the sub-nanometer scale, which is below or very close to the level of possible detection of the system. In order to separate this small signal from random noise, an alternating voltage combined with lock-in techniques is used.

In this case, in a standard PFM measurement, the tip is scanned across the sample surface with a driving voltage

$$V_{\text{tip}} = V_{\text{dc}} + V_{\text{ac}} \cos(\omega t) \tag{2.8}$$

Because of the converse piezoelectric effect, the material deforms mechanically. Thus the surface displacement can be calculated as

$$z = d_{33} V_{\text{ac}} \cos(\omega t + \varphi) \tag{2.9}$$

The surface piezoelectric response can be defined as the tip deflection induced by the first-harmonic component of bias, which can be described as

$$d = A_{\text{dc}} + A_{\text{ac}} \cos(\omega t + \varphi) \tag{2.10}$$

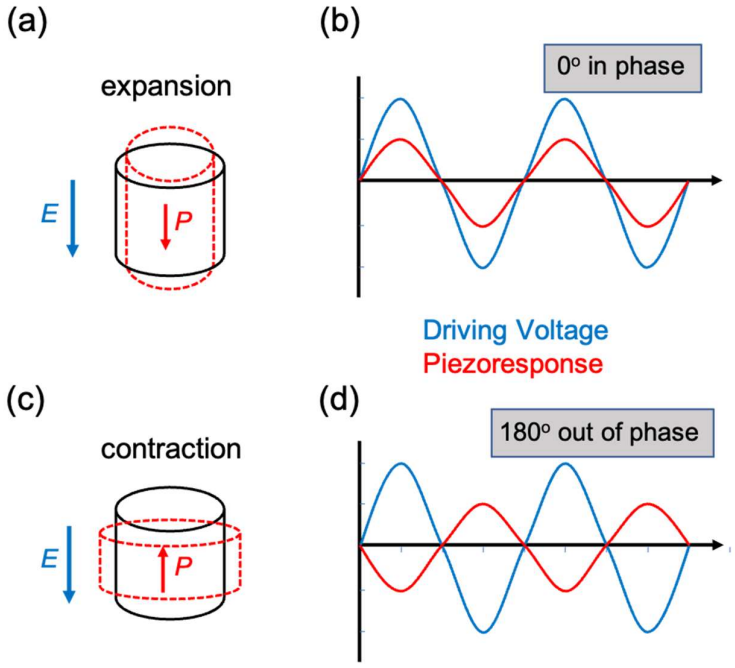

Figure 2.13 Principle of the phase shift in piezoresponse. Regarding the downward polarization domain, an in-phase piezoresponse to the driving voltage is shown, (a) the surface expands with the applied parallel electric field *E*, the cantilever is bending upwards, (b) in-phase $\boldsymbol{\varphi = 0^{\circ}}$ piezoresponse occurs; For an upward polarization domain, the vibration is out of phase with the driving voltage, (c) the surface contracts with the applied antiparallel electric field *E*, the cantilever is bending downwards, (d) out-of-phase $\boldsymbol{\varphi = 180^{\circ}}$ piezoresponse occurs.

The probing voltage V_{ac} should be high enough to obtain a detectable response of the local ferroelectric domains but sufficiently low to avoid tip-induced local switching effects. [54, 55] The phase shift φ between the driving signal and the piezoresponse signal yields information about the polarization direction of the domains under the tip.

If the polarization below the tip is pointing downwards, the positively applied excitation field E will induce the expansion of the sample, as shown in Fig. 2.13(a). The resulting oscillation of the sample is synchronized with the driving voltage of the tip. In this case, the corresponding phase shift is 0° (Fig. 2.13(b)). Conversely, if the polarization is pointing upwards, the antiparallel positive excitation field E could induce the contraction of the sample, as shown in Fig. 2.13(c). A corresponding out-of-phase piezoresponse with a phase shift of 180° is detected (Fig. 2.13(d)). Generally, domains with their spontaneous polarization pointing out of the surface (upwards) are denoted c^+ domains and those with their spontaneous polarization pointing into the surface (downwards) are denoted c^- domains.

Basically, two operating modes of PFM imaging are widely accepted: vertical and lateral PFM (VPFM and LPFM). VPFM is sensitive to out-of-plane piezoresponse, whereas LPFM is sensitive to in-plane piezoresponse.[173] VPFM allows the spatial mapping of the out-of-plane component of the ferroelectric polarization, as illustrated in Fig. 2.14(a). LPFM measures the in-plane piezo-mechanical deformation of the sample surface (as illustrated in Fig. 2.14(b)), which is associated with the lateral torsion of the cantilever. Combined with VPFM, the overall signals, e.g., the 3-dimensional orientation of the polarization and sample surface analysis, can be deduced using equipped multiple lock-in amplifiers. This method is called vector PFM [173, 175].), in which the collected piezoresponse signal consists of phase and amplitude (PRphase and PRamplitude). [176]

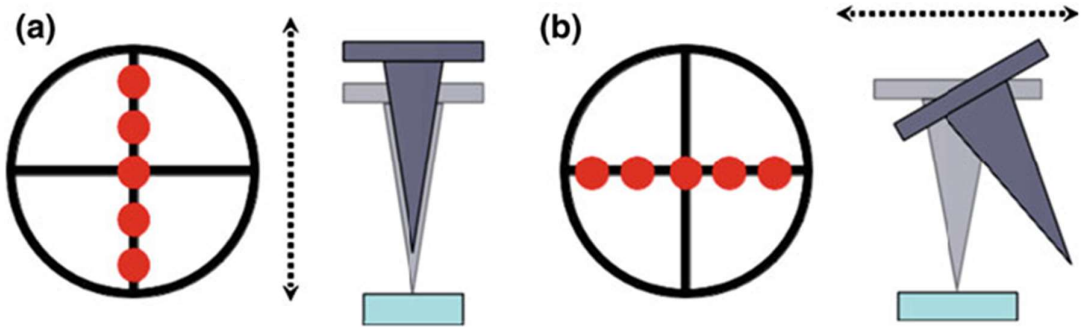

Figure 2.14 Schematic illustration of vertical and lateral PFM acquisition. In VPFM (a), the vertical oscillation of the reflected laser is measured and associated with the deflection of the cantilever. InLPFM (b), the horizontal shift of the reflected laser is measured and associated with the cantilever torsion. (Reprinted from Ref. [174] with the permission of Springer Nature. Permission license number: 5452990226787)

2.5.2 Switching Spectroscopy Piezoresponse Force Microscopy

Switching Spectroscopy Piezoresponse Force Microscopy (SS-PFM) extends the application of standard PFM. Its site-specified measurement enables precise nanoscale measurement of the ferroelectric properties of materials. SS-PFM allows for quantitative imaging of the local ferroelectric switching, saturation, coercive biases, and remanent responses. [177, 178]. SS-PFM greatly enhances the capacity of the PFM technique, offering a new landscape for nanoscale domain studies.

In SS-PFM, as represented in Fig. 2.15(a), by applying an electric waveform $V_{tip} = V_{dc} + V_{ac} \sin \omega t$ to the conductive cantilever/tip, a local *P-E* loop is picked at each grid point on a designed N × M mesh. When acquiring a hysteresis loop, the tip keeps touching a given location on the material's surface. An SS-PFM map is obtained by moving the tip point by point after each hysteresis loop is achieved. The obtained SS-PFM maps can be correlated with the surface topography or results from other microscopic techniques to understand the mechanism behind the ferroelectric properties of materials. In SS-PFM, a square wave V_{dc} superimposed by an *ac* signal moves in magnie with time, carrying a sine wave. As shown in Fig. 2.15(b), the signal consists of a series of pulses with increasing/decreasing amplitudes and time length τ_1 (high state) divided by zero-bias intervals lasting for τ_2 (low state). The envelope of the voltage pulses can be presented by a triangular waveform, which has a specified amplitude and period. After a settling time δτ, the piezoresponse amplitude/phase signals are acquired for the time span τ_3 by the superimposed ac signal in the high (low) state, which is customarily called bias-on and bias-off hysteresis loops, respectively. Within the

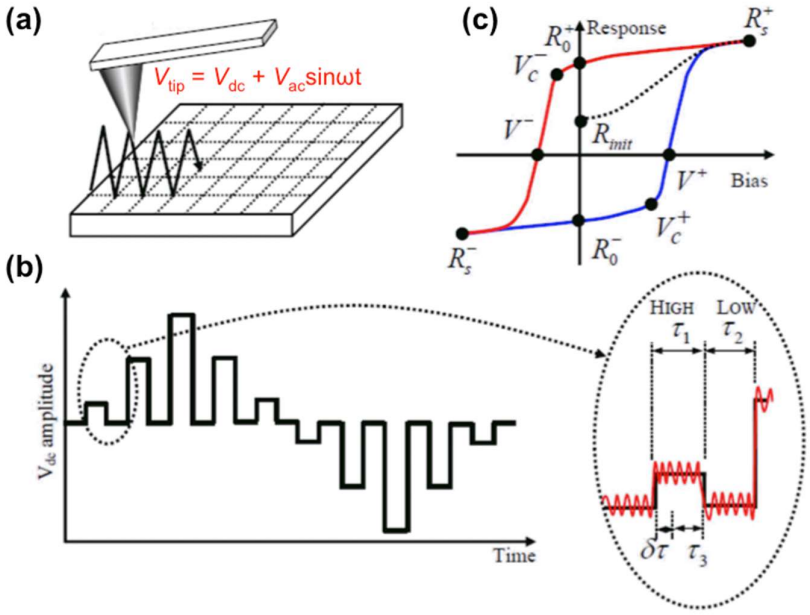

Figure 2.15 Diagram of SS-PFM. (a) The map of local hysteresis loops is collected at each point on the designed *N* × *M* mesh. (b) The applied electric waveform and the data acquisition sequence for each hysteresis loop. (c) A representative PFM hysteresis loop. (from Ref. [179])

triangle voltage waveform at the off-field state, the piezoresponse can be acquired at each voltage value for the given hysteresis loop measurement. Thus, the PFM hysteresis loop is gained at each grid point. Several loops are taken at each point to verify the reproducibility and reduce the noise level of the signal. The relevant switching parameters, such as switchable polarization, imprint, coercive voltage VC, and effective switching work, i.e., the area under the loop, can be extracted in case PFM hysteresis loops are obtained at each grid point. A single hysteresis loop described as the effective piezoelectric response PR can be calculated from the amplitude and phase response in the hysteresis loops according to the following equation:

$$PR = A_h \cos(\phi_h) / V_{ac} \tag{2.11}$$

where A_h is the hysteresis amplitude loop, ϕ_h is the respective hysteresis phase loop.

An ideal hysteresis loop that originated from purely electromechanical detection is shown in Fig. 2.15(c). It contains the forward response $R^+(V)$ and reverses $R^-(V)$ response branches acquired at each point. R_{init} is the initial response. In the ideal case, the zero of $R^-(V)$ is V^- (negative coercive field) and the zero of $R^+(V)$ is V^+ (positive coercive field). The imprint is denoted by Im=$(V^+ + V^-)/2$. $R_0 = R_0^+ - R_0^-$ is a remanent switchable response, where R_0^+ and R_0^- correspond to negative and positive remanent responses. The maximal switchable response is defined as $R_m = R_s^+ - R_s^-$, where R_s^+ and R_s^- represent the negative and positive saturation responses. V_c^- and V_c^+ represent the reverse and forward domain nucleation voltages determined by crossovers between the hysteresis loop's rapid and constantly changing regions. In reality, the hysteresis loops obtained by SS-PFM are strongly affected by the measurement conditions, such as tip-surface contact quality, instrumental artifacts, finite driving amplitude, and electrostatic forces' influence. In general, hysteresis loops describe the evolution of the piezoresponse signal upon switching. For the SS-PFM measurement, a strongly localized and inhomogeneous electric field is applied to a single location with the probe, and thus the nucleation of a single ferroelectric domain is measured when starting the polarization switching. In contrast, macroscopically, the nucleation, growth, and interaction of multiple separated domains are involved in the switching process when applying a uniform electric field.

2.6 Kelvin Probe Force Microscopy

The basic principle of Kelvin probe force microscopy (KPFM) and the operational mode will be introduced, mainly based on Ref. [180, 181].

2.6.1 Principle of Kelvin Probe Force Microscopy

Kelvin probe force microscopy, modified from AFM. is a chemically sensitive method. [182] It is aimed to measure the local contact potential difference (CPD) between the sample surface and the tip. Since the first presentation in 1991 by Nonnenmacher et al [183], KPFM has been used in many

diverse fields as a unique technique to measure the nanoscale electrical properties due to the direct and quantitative measurement of the surface potential distribution.

By mapping the electrostatic interactions between the conductive tip and the sample, KPFM can measure potential differences. The measured potential between the tip and the sample is defined by their difference in work function Φ. The CPD between the tip and the surface is denoted by:

$$V_{CPD} = \frac{\Phi_{sample}}{q} - \frac{\Phi_{tip}}{q} = \Delta\Phi/q \tag{2.12}$$

where Φ_{sample} represents the work function of the sample, Φ_{tip} denotes the work function of the tip, and q means the elementary charge. When the tip is brought close to the sample surface, an electrical force between the sample surface and the conductive tip appears due to the differences in their Fermi energy levels. Fig. 2.16 shows the electronic energy levels of the sample and AFM tip. When the tip and sample surface are in contact, the Fermi levels will align through electron current flow. The tip and sample will be charged, and an apparent V_{CPD} will be formed. Thus, electrical force appears. By applying a DC voltage that has the same magnitude as the V_{CPD} with opposite direction, the force can be nullified. Since V_{CPD} is equal to the work function difference between the tip and sample, the work function of the sample can be calculated when the tip work function is known.

As an AC voltage (V_{AC}) is applied to the tip (sample) to excite the cantilever, oscillating electric forces between the sample surface and the conductive tip appear, which are proportional to the potential difference between the conductive tip and the surface. In order to eliminate the oscillating electrical forces, an additional DC voltage (V_{DC}) is applied so that a lock-in amplifier compensates for the potential difference introduced by the AC voltage. The bias's magnie and sign are determined by the

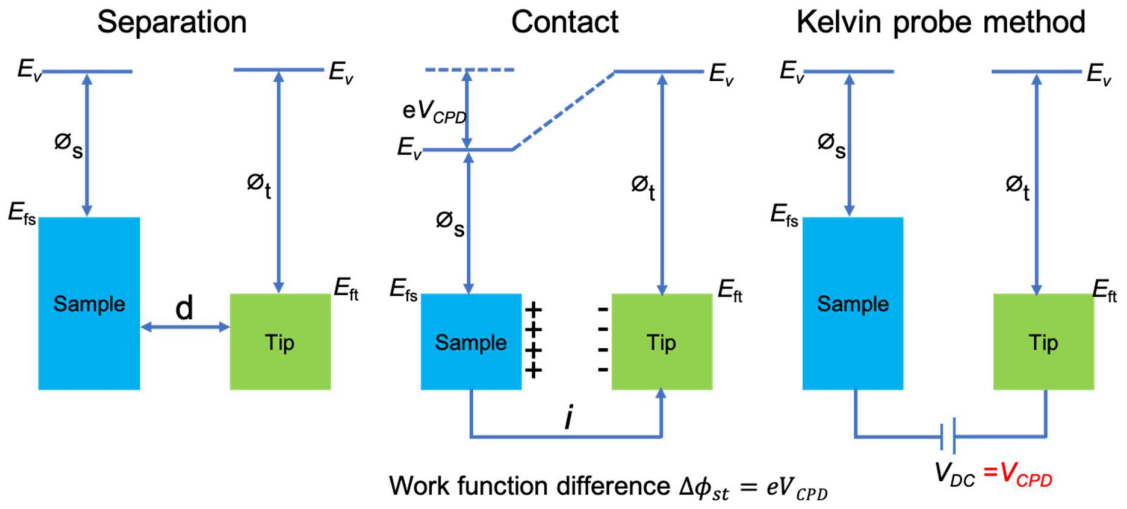

Figure 2.16 Principle of Kelvin Probe measurements. When the tip and the sample are contacted, a DC voltage is applied to nullify the CPD and thus the electrical force between tip and sample. E_v is the vacuum energy level. E_{ft} and E_{fs} are Fermi energy levels of the tip and sample, respectively.

contact potential difference where the nullifying V_{DC} is applied to the tip (−)or the sample (+). [184] The electrostatic force (F_{es}) between the tip and sample can be described as:

$$F_{es} = -\frac{1}{2}\frac{\partial C(z)}{\partial z}\Delta V^2 \tag{2.13}$$

where z represents the direction perpendicular to the surface, ΔV and $\partial C/\partial z$ correspond to the potential difference between the tip voltage and V_{CPD}, and the gradient of the capacitance between tip and surface. As $V_{AC}\sin(\omega t) + V_{DC}$ is applied to the tip, ΔV will be defined as:

$$\Delta V = V_{tip} \pm V_{CPD} = (V_{DC} \pm V_{CPD}) + V_{AC}\sin(\omega t) \tag{2.14}$$

With the combination of equations 2.13 and 2.14, the electrostatic force applied to the tip is given as:

$$F_{es}(z,t) = -\frac{1}{2}\frac{\partial C(z)}{\partial z}[(V_{DC} \pm V_{CPD}) + V_{AC}\sin(\omega t)]^2 \tag{2.15}$$

The equation above can be divided into three terms:

$$F_{DC} = -\frac{\partial C(z)}{\partial z}[\frac{1}{2}(V_{DC} \pm V_{CPD})]^2 \tag{2.16}$$

$$F_{\omega} = -\frac{\partial C(z)}{\partial z}(V_{DC} \pm V_{CPD})V_{AC}\sin(\omega t) \tag{2.17}$$

$$F_{2\omega} = \frac{\partial C(z)}{\partial z}\frac{1}{4}{V_{AC}}^2(\cos(2\omega t) - 1) \tag{2.18}$$

F_{DC} leads to a static deflection of the tip, which is frequency-dependent. F_{ω} occurs at the AC voltage drive frequency ω, and it can be utilized to measure the V_{CPD}. $F_{2\omega}$ oscillates at twice the drive frequency, being used for capacitance microscopy. [181] An oscillatory force at the drive frequency can be stimulated by applying the AC bias at frequency ω to the tip and the sample. The excited oscillatory force is proportional to the potential difference between the conductive tip and the surface and the magnie of the applied AC voltage. By using a lock-in amplifier, V_{CPD} is measured. Thereby, the electrical force component with frequency ω (F_{ω}) can be subtracted. The output of the lock-in amplifier is closely related to the difference between V_{CPD} and V_{DC}. Using a feedback loop with a input which is the component of the electrostatic force at a frequency of ω, F_{ω} can be eliminated when apply a V_{DC} to the tip that makes $V_{DC} = V_{CPD}$. Therefore, V_{CPD} value can be obtained.

2.6.2 KPFM operation modes

In KPFM, the electrostatic force F_{ω} can be measured in both amplitude mode (AM) and frequency mode (FM). In the FM-KPFM mode, F_{ω} denotes frequency shift at ω. When adding an oscillating bias to a DC offset, the corresponding frequency shift yields at the bias modulation frequency. In order to nullify the generated frequency shift, V_{DC} is applied to the tip. Therefore, V_{CPD} can be acquired. In the AM-KPFM mode, F_{ω} can be directly measured from the amplitude of the cantilever

oscillation at ω caused by V_{CPD} and V_{AC}. The resulting amplitude is nullified by applying V_{DC} to the tip so that V_{CPD} is measured. The FM-KPFM has a higher spatiall resolution while AM-KPFM offers a higher signal to noise ratio (SNR). KPFM images measured by AM- have artifact induced since the surface potential measurement is significantly affected by the stray capacitance between the cantilever and surface.

KPFM measures topography and V_{CPD} signals at the same time, and a method is desired to separate both signals. For this reason, V_{AC} in the KPFM setup is often modulated at a higher frequency than topography feedback's bandwidth to hinder the interference between CPD and topography signals. For AM-KPFM, there are two passes for its working process. It is also called lift-mode surface potential imaging. For the first pass, by using standard AFM at tapping mode, the topography can be acquired by the cantilever oscillation at the first resonance frequency of the tip. In the second pass, the surface potential V_{CPD} can be obtained by measuring the amplitude of the cantilever oscillation at the tip's second resonance frequency. Both passes are staggered. The tapping drive for the cantilever is activated, measuring the oscillation response for the first pass, and switched off for the second pass. Nevertheless, the applied V_{AC} to the tip is tuned to the second resonance frequency on the second pass so that the tip can be activated by the electric force. In this scenario, the topography and potential signal can be divided and displayed individually. In FM-KPFM mode, the tip scans over the surface at a fixed height. The mechanical vibration of the tip is obtained at the first resonance frequency. In order to get the modulation of the electrostatic force, V_{AC} is applied to the tip, thus leading to the separation of topography and potential.

3. Results and Discussions

3.1 Ferroelectric Domain Evolution in a $Ba(Zr_{0.2}Ti_{0.8})O_3$-$0.5(Ba_{0.7}Ca_{0.3})TiO_3$ (BZT-0.5BCT) Piezoceramic Studied Using Piezoresponse Force Microscopy*

Due to increasing concerns regarding environmental protection and human health, tremendous efforts have been devoted to investigations of Pb-free piezoceramics, whose electromechanical properties are competitive with those of lead-zirconate-titanate. ($PbZr_xTi_{1-x}O_3$, PZT). [185], [186] Examples include compositions based on $BaTiO_3$, $Na_{0.5}Bi_{0.5}TiO_3$, $K_{0.5}Bi_{0.5}TiO_3$, $BaZr_xTi_{1-x}O_3$, $Ba_{1-x}Ca_xTiO_3$, $K_{0.5}Na_{0.5}NbO_3$, etc. [187, 188] are widely studied. Among these, lead-free $Ba(Zr_{0.2}Ti_{0.8})O_3$-$x(Ba_{0.7}Ca_{0.3})TiO_3$ (BZT-xBCT) solid solution has received considerable attention in recent years due to its excellent electromechanical properties. [75], [189] Since the initial discovery of the BCT-xBZT system by Liu and Ren [145], researchers have widely studied its microstructural features, [190-192] phase transitions, [42, 193-195] dielectric, [196, 197] optical, [198-200] electromechanical [201] and ferroelectric properties. [202] Furthermore, its piezoelectric properties as a function of temperature and poling cycles have been intensively studied in the literature. [143, 203] Temperature-dependent studies indicated a maximized piezoelectric coefficient and a relatively constant maximum polarization (P_{max} ~ 13–14 μC cm^{-2}) in the phase-convergent region. [143] The piezoelectric coefficient (d_{33}^*) and remanent polarization (P_r) of BZT-0.5BCT ceramics show a drop of 13% and 12%, respectively, after 10^7 unipolar cycles. [203] Nevertheless, our understanding of the structure-property relationship of BZT-0.5BCT ceramics is still limited. For instance, the phase diagram of BZT-xBCT ceramics close to room temperature (RT) remains controversial, specifically regarding the phase structure and transition temperatures. [143, 193] It is well known that the domain structure of piezoelectric ceramics, which is formed to minimize the electrostatic energy and relieve the elastic energy in the materials, is strongly related to their phase composition, macroscopic properties, and stability in their applications. [204] Previous studies have shown that the highest contribution to the electromechanical response of BCT-0.5BZT comes from extrinsic contributions, i.e., from domains (more than 60%). [201, 205] Therefore, comprehensive studies of the domain evolution of BZT-xBCT ceramics are required to uncover the fundamental physical mechanisms behind their excellent properties and to help engineer novel electronic devices.

To date, a broad spectrum of microscopy techniques have been developed for visualizing ferroelectric domain structures at different length scales. [206] Common methods include optical microscopy techniques at the micrometer scale, [207] e.g., second harmonic generation techniques, scanning force microscopy methods at the micro- to nanometer scale, [57] e.g., piezoresponse force microscopy

*This chapter has been published in Ref. [208]. (Reprinted with the permission of AIP Publishing. The permission license number: 5465290068904)

(PFM), and electron microscopy methods at the atomic scale, [209] e.g., transmission electron microscopy (TEM). Owing to their high spatial resolution, PFM and TEM are often adopted to study mesoscopic domains and atomically sharp domain walls in piezoelectric materials. [210, 211, 142, 151] Numerous TEM studies have focused on delineating the domain morphology of BZT-*x*BCT ceramics. Using TEM, Gao *et al.* [158] and Zheng *et al.* [212] demonstrated the existence of hierarchical nanodomains in the BZT-*x*BCT system at RT. However, the TEM specimen has to be very thin (ideally below 50 nm) for this approach, and electron beam radiation can be destructive to the structure, possibly altering the experimental results. [207] In contrast to TEM, PFM imaging, which can be conducted after a simple polishing of the sample surface, enables us to nondestructively image domain structures closer to their original states. Indeed, one should be very careful about surface effects on PFM results. Rojas *et al.* [203] used PFM to visualize the evolution of domain morphology for the BZT-*x*BCT system after cycling, and clarified the effects of strain on fatigue behavior. Coondoo *et al.* [213] investigated the local electrical polarization with PFM, revealing a complex mosaic-like domain structure. Although many works based on PFM imaging of BZT-0.5BCT ceramics can be indexed, [146, 214] researchers have yet to systematically investigate how the domain structure changes under the influences of both temperature and electric field stimulation, which would be beneficial for understanding the relation between domain structure and functionality in practical applications. To this end, I have studied the field-dependent domain structure at different temperatures using PFM to investigate the domain evolution of BZT-0.5BCT piezoceramics.

3.1.1 Experimental

$Ba(Zr_{0.2}Ti_{0.8})O_3$-$0.5(Ba_{0.7}Ca_{0.3})TiO_3$ (BZT-0.5BCT) samples were prepared by conventional solid-state synthesis method. Powders of $BaCO_3$ (99.8%), $CaCO_3$ (99.5%), ZrO_2 (99.5%), and TiO_2 (99.6%) were mixed according to the corresponding stoichiometric formula. Calcination was performed at 1300°C for 2 hours. After calcination, the powders were formed into discs by uniaxial hand pressing in a 10 mm die, followed by cold isostatic pressing (CIP 100 E, Paul-Otto Weber GmbH, Remshalden, Germany) at 300 MPa. Sintering was performed at 1500°C for 2 hours. Details of the sample synthesis and the relevant functional properties, including the polarization curves at elevated temperatures, can be found in Refs. [203, 138].

For the preparation of the PFM sample, BZT-0.5BCT ceramics were polished using diamond paste with abrasive particles of 15 µm, 6 µm, 3 µm, 1 µm, and 0.25 µm (DP-Paste P, Struers A/S, Ballerup, Denmark) for 1 hour each. The finishing was performed in a final polishing step of 15 min with a colloidal silica polishing suspension (Mastermet, Buehler GmbH, Düsseldorf, Germany), and then annealed at 400 °C for 2 hours.

The PFM measurements were performed using an MFP-3D atomic force microscope (Asylum Research, Santa Barbara). Electrically-conductive cantilevers AC240TM (Asylum Research, Santa

Barbara) with tip coatings of Ti/Pt (5/20) were used and the PFM was operated in its standard mode. For the PFM measurements, the nominal (free) resonance frequency and nominal force constant were 60 kHz and 2 N/m. The contact resonance frequency was $f_{CR} \approx 650$ kHz for the lateral tip vibration. The driving frequencies were set slightly below the respective contact resonance frequencies to provide stable detection signals and avoid drift during data acquisition. Images were taken at a scan rate of 0.8 Hz, resulting in a tip velocity of 12 µm/s with a digital resolution of 256 × 256 pixels. Next, *dc* voltages (HVA220 high voltage amplifier, Asylum Research, Santa Barbara) ranging from -30 V to +30 V were applied to the tip for hysteresis analysis and electric field-dependent measurements while scanning the sample surface. I ensured a stable topographic feedback during poling using topography and the mean deflection signal, ensuring that the tip remained on the surface (see Appendix Fig. A.4). For the temperature-dependent PFM study, a heating stage was used to set the temperature reversibly from 25 °C to 60 °C in 5 °C steps. Due to an enhanced thermal drift at higher temperatures, reliable and consistent results above 60 °C with our experimental setup can not be obtained. Therefore, our temperature-dependent domain evolution studies were focused on medium temperatures. Before the PFM measurement, an electrical tune was performed to find the tip-sample contact resonance frequency. The drive amplitude was adjusted in order to obtain a reasonable signal-to-noise ratio, which was usually achieved for vertical target amplitudes of approximately 1–3 nm. The drive voltage was not changed during the experiment to ensure the comparability of the images. The typical ac driving voltages were 2 V and 1 V for Fig.s. 3.1-3.4 and Fig. 3.5, respectively. The match of trace and retrace curve in the observables obtained during the measurement could further ensure that the results were reliable. The lateral (2256 nm/V) and vertical (69 nm/V) inverse optical sensitivity for the cantilever type AC240TM used in this study were calibrated. For the vertical signal, standard deflection (V) vs. distance (nm) curves were generated and the resulting slope was measured in nm/V. For the lateral direction, I brought the tip into contact (set point force 140 nN), and scanned a silicon surface with a scan size of 5 and 10 nm (while the tip remained in stiction with the surface) perpendicular to the long cantilever axis, measuring the lateral deflection accordingly. [215]

In this work, the study of the domain evolution is mainly based on the lateral PFM results due to a high lateral resolution from the strong mechanical tip-sample coupling. [216, 217] Vertical results are displayed in the Appendix.

3.1.2 Results and Discussions

Figure 3.1(a) shows the phase diagram for the BZT-*x*BCT material system. The BZT-0.5BCT composition exhibited a phase transition from orthorhombic to tetragonal to cubic as the temperature increased above RT. According to this phase diagram, the BZT-0.5BCT system should be in an orthorhombic phase at RT. However, the actual phase composition at RT is a subject of debate.

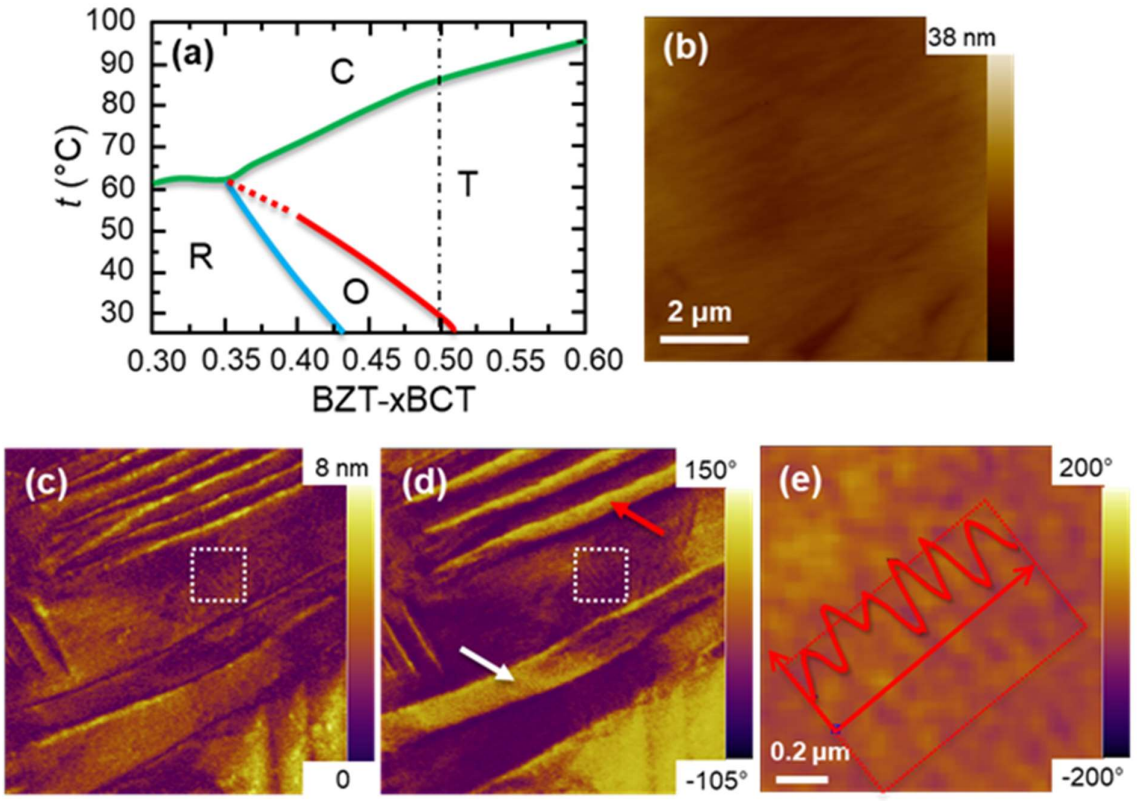

Figure 3.1 (a) A phase diagram of a BZT-*x*BCT ceramic (adopted from Ref. [143]). C, R, O, and T correspond to cubic, rhombohedral, orthorhombic, and tetragonal, respectively. The phase transition temperatures of the BZT-0.5BCT ceramic are approx. 30 °C (O-T) and approx. 90 °C (T-C). (b) The topography, (c) lateral PFM amplitude, and (d) lateral PFM phase image for the BZT-0.5BCT ceramic in its virgin state prior to poling and heating (see Appendix A.1 for vertical PFM results). (e) A close-up PFM phase image of the nanodomain structures indicated by the dash-squared area in (d). The inset shows the averaged intensity profile of the dashed box region.

Previous symmetry studies have indicated that the BZT-0.5BCT ceramic could exist in a rhombohedral, orthorhombic, tetragonal, or any combination of these phases at RT, with these states being hardly distinguishable experimentally. [144] Figure 3.1(b) displays a representative topography image of a surface-polished BZT-0.5BCT ceramic. The uniform contrast of the image and small root-mean-square roughness ($R_q \approx 1.45$ nm) imply a smooth surface after fine polishing and subsequent annealing. Simultaneously-acquired lateral amplitude and phase images in Fig. 3.1(c) and (d) present the virgin domain structure of the BZT-0.5BCT ceramic (see Appendix A.2 for the domain structure of a large region). Parallel lamellar domains (white arrow) and needle-like wedge-shaped domains (red arrow) with lengths of several micrometers and widths of hundreds of nanometers were seen to coexist inside the grains. Rhombohedral and tetragonal phases have previously been observed for wedge-shaped and lamellar domains, respectively [218], revealing that there may exist multiple phases of the

BZT-0.5BCT ceramic at RT in its virgin state. The domain size (d) of perovskite-structure ferroelectrics strongly depends on the grain size (g). [204] Their relation can be described as

$$d = \left\{\left(\frac{\sigma}{\varepsilon^* P_0^2}\right) g\right\}^{1/2}, \tag{3.1}$$

where σ, ε^*, and P_0 correspond to the energy density of the domain wall, the effective dielectric constant, and the spontaneous polarization, respectively. [219] Empirically, this relation can be expressed as $d \propto g^m$, where m is in the range 0–1/2 when g is larger than 10 μm. [220] As-sintered BZT-0.5BCT ceramics have g=28.9±4.6 μm. [203] Thus, the observed domain size, which lies between micron and sub-micron scales, is reasonable according to the formula mentioned above. The observed sub-micron domains are believed to have a reduced domain wall energy and thus reduce the energy barriers between polarization states, playing a key role in piezoceramics with enhanced performances. [221],[222] A close-up image of the dash-squared area in Fig. 3.1(d) is displayed in Fig. 3.1(e), showing the miniaturized nanodomain structures with an averaged domain width of approx. 60 nm. Similar results have been reported in the literature.[42, 221, 222]

To probe the ferroelectric domain state and evolution mechanism of the BZT-0.5BCT system in different crystallographic states, the domain structure was then measured at a series of temperatures of 25 °C, 40 °C, 45 °C, 50 °C, 60 °C, and back to 25 °C. In order to reach the thermal equilibrium of the PFM setup, the domain structure was captured five minutes after reaching the desired temperatures.

Figure 3.2 shows the temperature-stimulated domain structure evolution in the BZT-0.5BCT piezoceramic. Similar to the results of Fig. 3.1, both lamellar and wedge-shaped domains were seen to be present in the studied region at the starting temperature (25 °C). A hierarchical domain structure with large quantities of nanoscale domains is visible. When the temperature was increased to 40 °C, one could observe some curved domain walls (circled in yellow) at the boundaries, where wedge-shaped domains and the parallel lamellar domains intercepted, which probably resulted from the immense strain difference between the two sides of the domain wall. [142] Similar curved domain walls have also been observed in Pb-based piezoceramics. [223] In the blue box region, initially containing wedge-shaped domains, the shape of the domains was slightly altered into a lamellar structure at 45 °C, and some domain walls moved toward the right side of the box region as the temperature increased. For example, the initial length of the white-line encircled domain was about 2.8 μm. It grew to 3.9 μm at 45 °C and 5.2 μm at 60 °C, which is almost twice the initial value in the virgin state. These temperature-dependent domain features imply that the phase transition to the tetragonal structure occurred at a temperature between 40 °C and 45 °C in our experiment. Interestingly, it shows that the original single domain structure, marked by the blue arrow, transformed into many lamellar nanodomains at 45 °C. This domain miniaturization can also be observed in the region marked by the red arrow. This phenomenon is attributed to a transitional state for releasing the elastic strain and thermal strain during the phase transition. While heating to 60 °C, a substantial

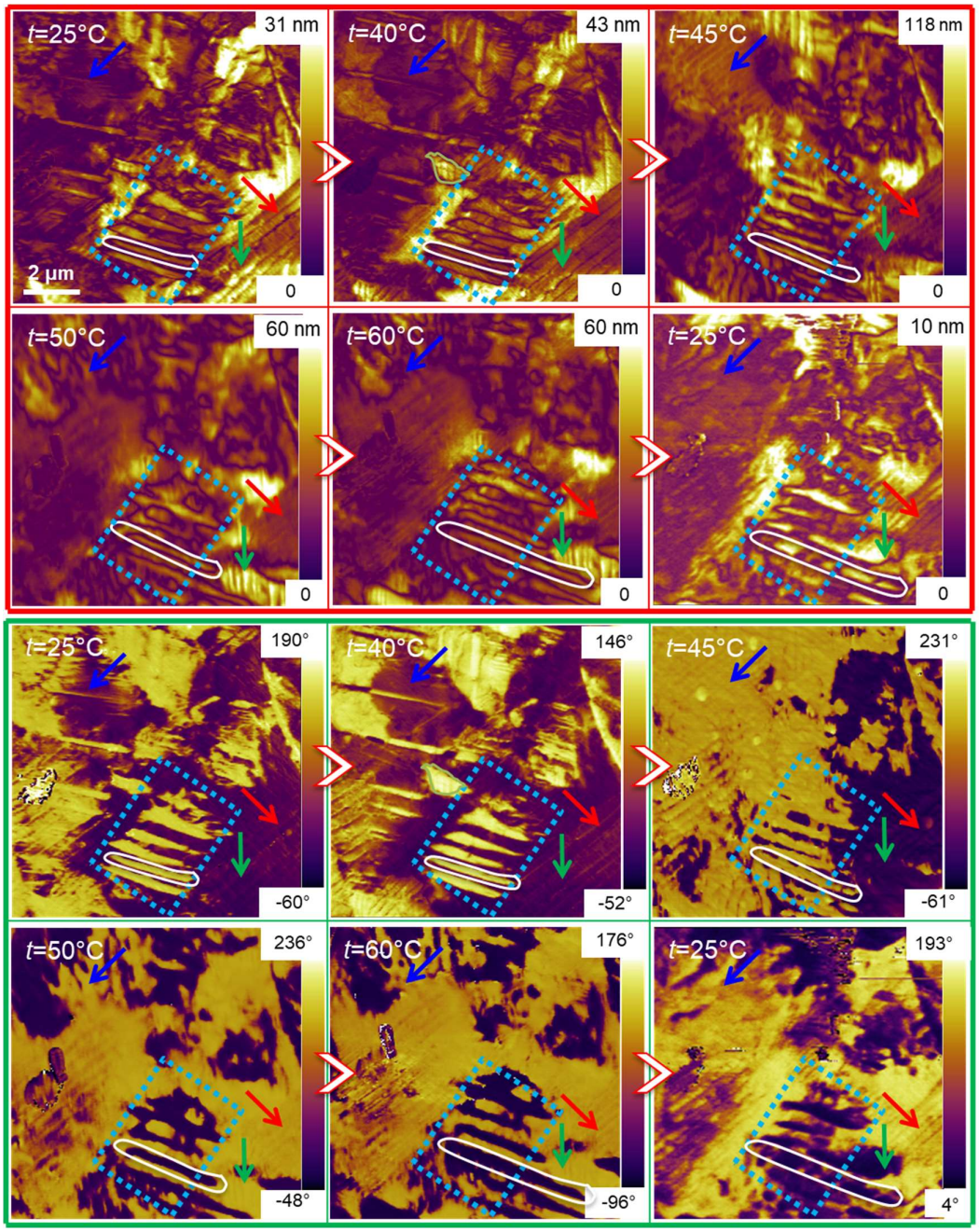

Figure 3.2 The temperature-dependent domain evolution of the BZT-0.5BCT ceramic. The lateral PFM amplitude (red box) and phase (green box) for the BZT-0.5BCT ceramic during heating up to 60 °C and subsequently cooling down to RT (t = 25 °C) (see Appendix Fig. A.3 for the topology and vertical PFM results).

change in the domain morphology occurred with a noticeable weakening in PFM contrast, resulting in a weakening of the piezoelectric effect as the Curie temperature was approached. Tip degradation as a reason for the loss of contrast can be excluded because of intact measurements using the same tip after the experiment. The wedge-shaped domains progressively disappeared, and nanodomains inside them started to merge and transform into parallel lamellar domains, confirming the transition to the tetragonal phase. Upon cooling back to RT, the domain structure came to consist of parallel lamellar

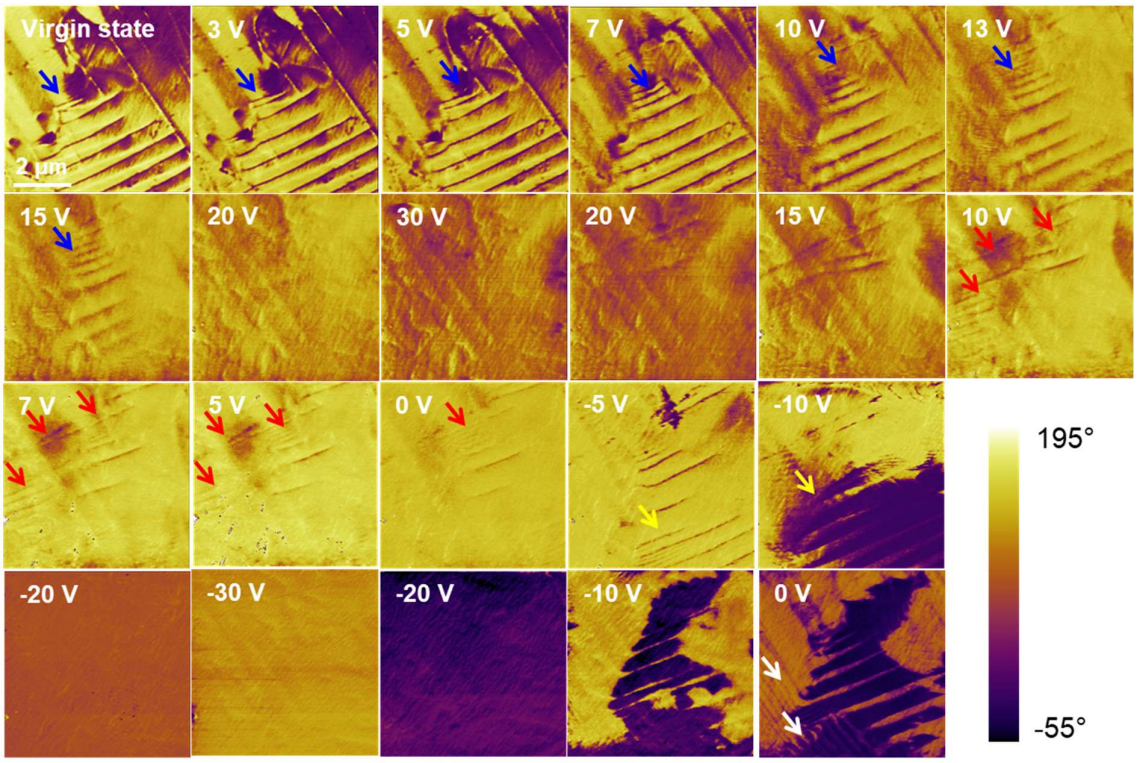

Figure 3.3 The domain evolution of the BZT-0.5BCT ceramic under the stimulation of external electrical fields generated by the PFM tip at RT (t = 25 °C). The presented lateral phase maps were acquired by applying voltages, which were applied to the same area as the picture size, in one complete loop (0 V→ 30 V→ 0 V→ -30 V→ 0 V) (see Appendix Fig. A.4 for the topology and vertical PFM results).

domains similar to those of the virgin state but with a smaller width and a higher density of domain walls, likely due to the growth of nanodomains. [158, 224] Furthermore, one could also observe that the wedge-shaped domains in the blue box region seen in the virgin state did not reappear. This effect may be due to some highly mobile walls of the wedge-shaped domains in the BZT-0.5BCT piezoceramic, which could have led to the formation of curved instead of straight domain walls when the temperature was reduced to RT. Furthermore, this observation might also be related to thermal strain effects, because wedge-shaped domains with a low symmetry structure could be susceptible to slight strain variations.

For technical applications of the BZT-0.5BCT ceramic, it is crucial to understand the domain-morphology evolution during the electrical poling process. Figure 3.3 shows the domain evolution of an identical region measured using PFM within one poling cycle. All domain maps were simultaneously acquired exploiting the ac voltage stimulus (signal reading) while the probe scanned over the surface under the specified dc voltage (domain switching). As the applied dc voltage was increased from 0 V to 20 V, more ferroelectric domains coalesced. The lamellar domains in the top-left region became blurred at 10 V due to the sidewise motion of the domain walls and almost coalesced to a single domain at 13 V. In contrast, the wedge-shaped domains marked by the blue

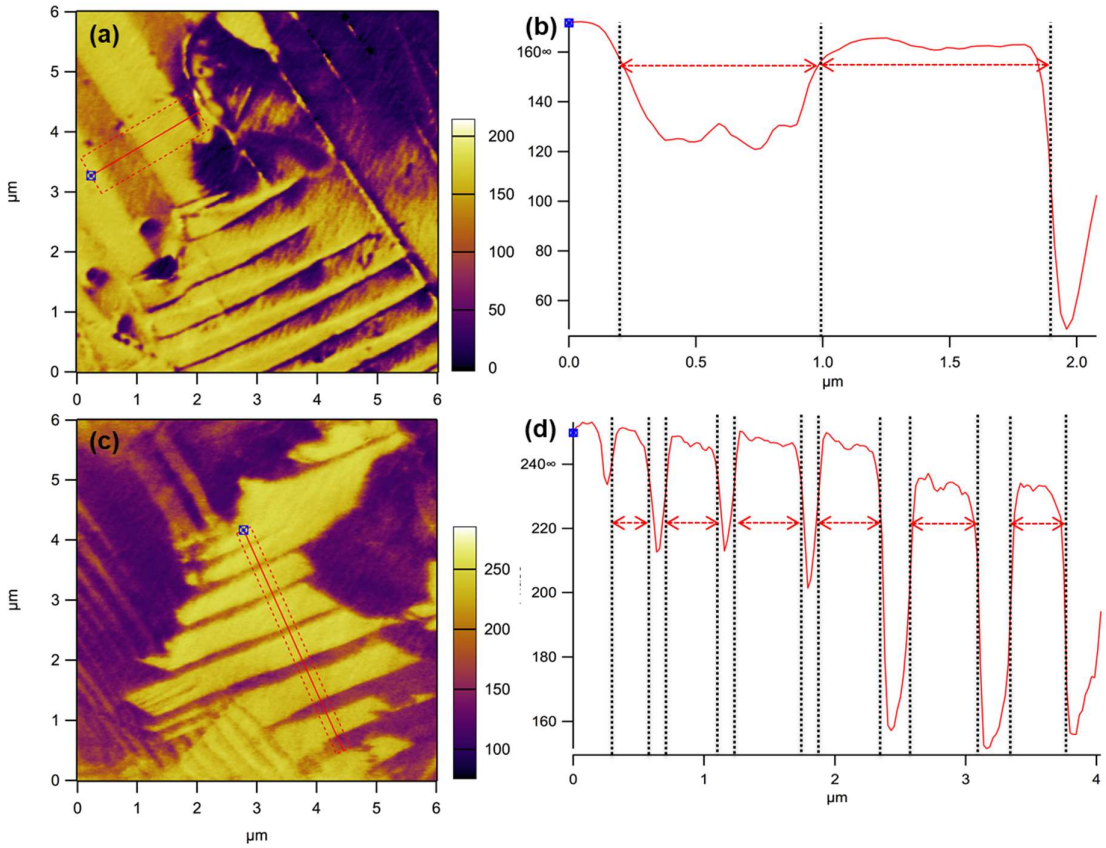

Figure 3.4 (a) The lateral PFM phase image for the BZT-0.5BCT ceramic in its virgin state. (b) The extracted intensity profile of the box region in (a). (c) The lateral PFM phase image for the BZT-0.5BCT ceramic after one poling cycle. (d) The extracted intensity profile of the box region in (c).

arrow initially remained visible (0 – 7 V, approx. 353 nm in width and 2823 nm in length at 0 V, given that a wedge can be mimicked by an isosceles triangle), but turned into smaller domains (approx. 178 nm in width and 1470 nm in length at 15 V). These small wedge-shaped domains in the region adjacent to the boundary between wedge-shaped and lamellar domains can persist at high poling fields up to 15 V. Similar phenomena have been reported in the literature. [225] [226] As the applied voltage was further increased to 30 V, the transformation from a multi-domain structure to a single-domain state occurred, with most domains in previously unfavorable polarization directions becoming aligned with the applied field direction. The observed single-domain state can be explained by the formation of a field-induced orthorhombic phase with significant elastic softening. [227] Very weak features of the domain walls were still observable as the field was increased to 30 V, probably due to the instability of the single-domain state against higher poling voltages. [42] As the field strength was subsequently reduced, some domains started to switch back. Similar to a finding in Ref. [153], a transitional domain state (marked by the red arrow) was present at 10 V in the boundary region between the wedge-shaped and lamellar domains. The transitional state then vanished at 0 V due to the continuing motion of the domain walls as the field strength decreased. A few domains appeared after

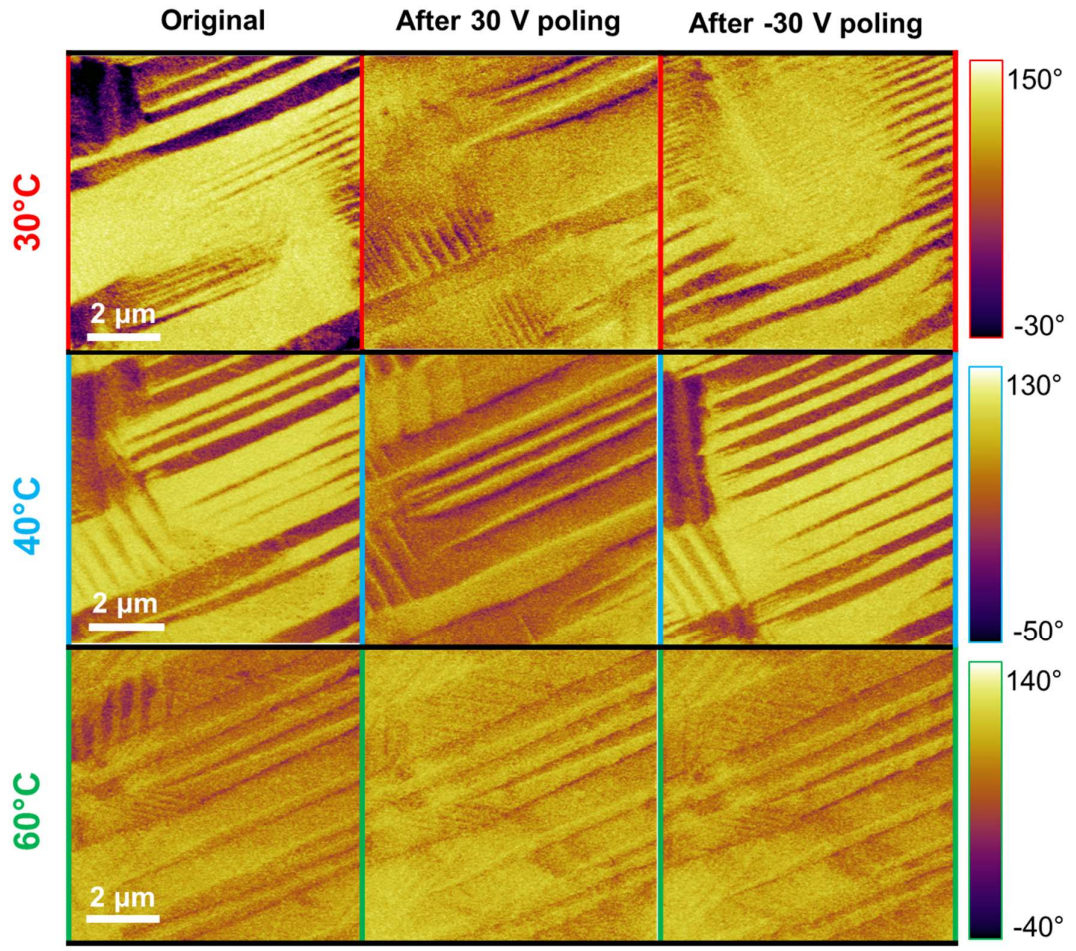

Figure 3.5 The domain evolution of the BZT-0.5BCT ceramic at three different temperatures (30 °C, 40 °C, 60 °C) during the poling process. The voltage was applied in one loop (0 V→ 30 V→ 0 V→ -30 V→ 0 V). PFM phase images captured for the 0 V initial states, states after the positive poling (30 V), and states after negative poling (-30 V) are displayed (see Appendix Fig. A.5 for the topology and vertical PFM results).

removing the field, indicating the existence of back-switched domains, which is in good agreement with former TEM studies. [42] The domain pattern after positive poling changed significantly from that of the virgin state. The region of interest was then poled in the opposite direction by applying a negative dc voltage to the tip with respect to the sample. The domain contrast became more significant at -5 V, which can be viewed as a transitional state of the domain evolution under negative poling. When further poled to -10 V, the shape of the domains, which were wedge-shaped in the virgin state, became lamellar. The single-domain state reappeared with the negative poling of -20 V. As the negative voltage was gradually reduced, lamellar domains emerged at -10 V and coexisted with wedge-shaped domains at 0 V. Interestingly, the wedge-shaped domain regions in the virgin state were changed to lamellar domains after one complete cycle of poling. This phenomenon may be due to a poling-induced premature phase transformation to the tetragonal phase, which could not be reversed after removing the poling field. [42, 228] The domain wall density was enhanced after just one poling

cycle. The total number of domain walls in a 6 μm×6 μm region increased from approx. 20 to approx. 40, with the averaged width of the lamellar domains being approx. 0.8 μm in the virgin state and approx. 0.3 μm after one poling cycle, as shwon in Fig. 3.4. This can be attributed to the reappearance of wedge-shaped nanodomains (marked by white arrows).

The reliability of piezoelectricity under thermal-electric cycling is vital for the practical application of piezoelectric materials. Electronic devices are often used above RT, and electric-field-induced heat originating from electron-phonon interactions may not dissipate quickly, leading to an inevitable increase in the material's temperature. Therefore, it is meaningful to perform a cross-study of the domain evolution under heating and poling. The BZT-0.5BCT ceramic in Fig. 3.5 was poled in the same manner as in Fig. 3.3 at different temperatures (see Appendix Fig. A.6, A.7 and A.8 for more domain maps). After a complete cycle of poling at 30 °C, the domain structure evolution was similar to that measured at RT, with the number of domains increased from 43 to 68. At 40 °C, the domain structure should still have a good extrinsic response to the applied voltage and therefore should exhibit some changes after poling because the temperature should still be in the vicinity of the phase boundary. In fact, in Fig. 3.5, one can see changes in the domain structure for the sample at 40 °C with the *E*-field applied, showing some newly-formed lamellar domains after a complete poling cycle with a minor increase in the number of domains from 35 to 40. However, the changes are not as significant as at 30 °C. When cycling the applied field at approximately 60 °C, the domain structure in the studied region was completely reversed. The number of domains remained fixed at 30. The BZT-0.5BCT ceramic is in the tetragonal phase at 60 °C. The domain structure generally has better reversibility at higher temperatures because of the decreased lattice distortion and decreased coercive field. [229] Furthermore, the response to the applied voltages is highly intrinsic for the tetragonal phase. Therefore, no changes in the domain structure are expected. These considerations explain the observations in this set of PFM experiments.

3.1.3 Conclusion

To conclude, our PFM experiments revealed that the virgin domain structure of a BZT-0.5BCT piezoceramic consisted of lamellar and wedge-shaped domains at RT. Under temperature and electric field stimulations, it is found that the wedge-shaped domains play a crucial role in the domain structure evolution of BZT-0.5BCT ceramics due to the swift response of its size and the domain wall motion. Furthermore, a transitional domain structure with a high density of domain walls in both the temperature and electric field cases is observed. Temperature-dependent domain evolution evidenced that a phase transition to a tetragonal structure occurred at a temperature between 40 °C and 45 °C in our experiment. A premature phase transition to the tetragonal phase under poling conditions was also revealed. Field-dependent domain studies at different temperatures for the BZT-0.5BCT piezoceramic directly revealed that the structure was mainly an extrinsic response at temperatures close to line of equilibrium in the phase diagram and intrinsic at higher temperatures far from the phase boundary.

Most interestingly, our electric-field-dependent PFM results show almost complete reversibility of the domain structure with an unaltered number and shape of domains at medium temperatures (40 °C – 60 °C), implying a slow rate of fatigue for the functional properties of the BZT-0.5BCT ceramics in this temperature range.[160, 203] An in-depth study of the correlation between the nanoscopic domain evolution and the macroscopic fatigue behavior will be a task for future work.

Contributions to this work:

Xijie Jiang (TUDa) carried out the PFM specimen preparation, PFM characterization, and related data processing. Na Liu (TUDa) and Christian Dietz (TUDa) offered help in PFM characterization. Virginia Rojas (TUDa) synthesized the BZT-0.5BCT ceramics. Jurij Koruza (TUDa) contributed to the discussion part of this chapter. Christian Dietz (TUDa) and Robert W. Stark (TUDa) supervised and oversaw this work. All authors discussed the results and contributed to this work.

3.2 Correlation between domain structure and the unipolar electric fatigue behavior in $Ba(Zr_{0.2}Ti_{0.8})O_3$-$x(Ba_{0.7}Ca_{0.3})TiO_3$ lead-free piezoceramics*

Piezoelectric materials have deeply affected modern life due to their wide application in electronic devices like actuators. Thanks to the outstanding piezoelectric properties at room temperatures, the lead-free (1-*x*)$Ba(Zr_{0.2}Ti_{0.8})O_3$-*x*$(Ba_{0.7}Ca_{0.3})TiO_3$ (BZT-*x*BCT) system has attracted much attention for practical applications. Furthermore, these materials exhibit a high blocking stress (σ_b) of about -64 MPa at 2 kV/mm [230] and low coercive fields (E_C below 0.5 kV/mm) [231], which exceed the performance of commercially available soft PZT. [232] As one of the major degradation mechanisms of piezoelectric devices, studies on the fatigue resistance behavior during electromechanical cycling are important for applications. The bipolar fatigue degradation of $Ba_{0.85}Ca_{0.15}Ti_{0.9}Zr_{0.1}O_3$ and $Ba_{0.92}Ca_{0.08}Ti_{0.945}Zr_{0.055}O_3$ has been reported by Zhang *et al.*[197] Both piezoceramics were found to have a higher resistance to bipolar fatigue at room temperature than that of soft PZT and NBT-BT materials. Subsequent work by Zhang *et al.* [233] studied the unipolar cycling resistance of BZT-50BCT, showing that the unipolar fatigue effect on the material is comparable to those of soft PZT ceramics. Nevertheless, detailed investigations on the electric fatigue behavior and its physical origin in BZT-*x*BCT ceramics with different compositions are relatively inadequate, hindering further development.

Electrical fatigue behavior of piezoceramics can be revealed by a broad spectrum of methods, including asymmetries and offsets in the polarization and strain hysteresis curves, a decrease of polarization, and even mechanical degradation. Many researchers have studied the electrical fatigue behaviors in ferroelectrics. [234-237] Macroscopic defects, such as microcracks, pores, and electrode edges, are thought to play a crucial role in the electric fatigue behavior because they constitute stress concentration points and serve as the origin for crack growth when submitted to electric cycling. [238, 239] Furthermore, point defects such as oxygen vacancies and other charge carriers are also susceptible to the applied electric field and migrate during cycling. The migration of such defects towards the grain boundaries or electrodes can hinder the domain wall movement, which affects the overall magnitude of electromechanical properties of the material. [240-243] Micro-to-nanoscale characterization of the morphology and ferroelectric domain evolution before and after electrical poling cycles is very useful to understand the electric fatigue behaviors of BZT-*x*BCT ceramics. Using SEM, Zhang *et al* [197] demonstrated that the BZT-*x*BCT ceramic with a lower amount of Ca and Zr exhibited a weaker domain wall pinning effect, but exhibited signs of more considerable mechanical degradation by microcracking due to the presence of large and irregular pores. For a deeper understanding of the domain structure, PFM studies of the phase and amplitude of domain structure in different directions are essential, which will be my main work in this part.

*Part of this chapter has been published in Ref. [203].

The deterioration of properties caused by electric fatigue might change with the different loading scenarios [235], which include unipolar [244, 245], bipolar [241], or sesqui polar cycling [246], and with or without compressive preloads [247]. Since actuators are generally driven with unipolar electric fields, this work will focus on studying the unipolar cycling scenario, which is essential from an application point of view.

The majority of studies on BZT-xBCT materials focus on the composition where x = 0.50, although other compositions also possess excellent properties. For instance, there is higher blocking stress for BZT-0.42BCT [160], the improved temperature stability of d_{33}^* in BZT-0.6BCT [143], and higher T_c for compositions with less Zr and Ca, such as in $(Ba(Zr_{0.15}Ti_{0.85})O_3$-$x(Ba_{0.8}Ca_{0.2})TiO_3)$ [248]. Moreover, the strain responses of different compositions were shown to be dominated by different mechanisms, which could have significant impacts on their cyclic degradation characteristics [201, 205]. Therefore, the aim of this study is to conduct domain configuration imaging using PFM before and after cycling and to probe the strain-unipolar fatigue behavior relationships of BZT-xBCT ceramics with different compositions with distinct crystal structures. Strain and polarization curves were evaluated up to 10^7 electric field cycles.

3.2.1 Experimental

Three compositions of the $(1\text{-}x)Ba(Zr_{0.2}Ti_{0.8})O_3$-$x(Ba_{0.7}Ca_{0.3})TiO_3$ (BZT-xBCT) system with x = 0.40, 0.50, and 0.60, hereafter referred to as 40BCT(R), 50BCT(O), and 60BCT(T), were prepared by the solid-state synthesis. Note that the letter in parentheses denotes the crystal structure at room temperature: rhombohedral (R), orthorhombic (O), and tetragonal (T), as determined by X-ray diffraction (D8 Advance, Bruker Inc., Rheinstetten, Germany). Powders of $BaCO_3$ (99.8%), $CaCO_3$ (99.5%), ZrO_2 (99.5%), and TiO_2 (99.6%) were mixed according to the corresponding stoichiometric formula and milled for 5 hours in a planetary mill using ethanol and ZrO_2 milling media. The suspension was then dried and the powders were calcined at 1300°C for 2 hours. After calcination, the powders were again milled, dried, and formed into discs by uniaxial hand pressing in a 10 mm die, followed by cold isostatic pressing (CIP 100 E, Paul-Otto Weber GmbH, Remshalden, Germany) at 300 MPa. Sintering was performed at 1500°C for 2 hours, with a heating rate of 5 °C/min. The sintered pellets were ground to a thickness of about 0.7 mm and silver electrodes (Silver paste, Gwent group of companies, Gwent, United Kingdom) were painted and burnt-in at 400°C. Subsequent annealing treatments after completing the unipolar cycling measurements were done at 400°C for 2 hours.

The electric field cycling tests were carried out using unipolar triangular waveforms with an amplitude of 5 times the coercive field (E_C) and a frequency of 50 Hz. A maximum of 10^7 cycles was performed and measurement of bipolar and unipolar polarization and the strain was done after every cycling decade at $5 \cdot E_C$ but at a frequency of 1 Hz. The first 10^5 cycles were done on the modified Sawyer-

Tower circuit also used for characterization. The electric cycling from 10^5 to 10^7 cycles, equivalent to ~55 hours of cycling, was carried out using a Sawyer-Tower setup designed for longer-running high voltage experiments.

The domain structure of polished surfaces of samples before and after cycling was observed using vector piezoresponse force microscopy (PFM). The polished samples were first imaged in the annealed state. The position of each image was recorded on an optical microscope picture of the polished surfaces. Subsequently, silver electrodes (Silberleitlack, Ferro GmbH, Frankfurt, Germany) were painted and dried at room temperature followed by the application of the 10^7 unipolar cycles. Afterwards the electrodes were removed using acetone. The samples were then carefully re-positioned on the PFM holder according to the images taken in the optical microscope in order to view the same area as before cycling. All PFM images were taken within 24 hours after the cycling was finished.

A Cypher atomic force microscope (Asylum Research, Santa Barbara, CA, USA) was used to perform the PFM measurements. The nominal force constant and first free resonance frequency of the conductive cantilevers ASYELEC-01 (Asylum Research, Santa Barbara, CA, USA) were k = 2 N/m and f = 70 kHz, respectively. The contact resonance frequencies for the cantilever vibration on the BZT-xBCT samples were $f_{CR,v} \approx 300$ kHz and $f_{CR,l} \approx 870$ kHz for the vertical and lateral vibration, respectively. The excitation frequencies for both directions were set slightly below the respective contact resonance frequencies in such a way that the vibrational amplitudes were approximately 30 % of the peak amplitude. A drive amplitude in both directions in the range of 2–4 V, a scan rate of 0.3 Hz (tip velocity 12 µm/s) and a digital resolution of 256×256 pixel was applied. Topography images were first-order flattened, whereas amplitude and phase images remained untreated.

3.2.2 Results and Discussions

The three investigated compositions, 40BCT (R), 50BCT (O), and 60BCT (T), have different crystallographic structures at room temperature, in agreement with previous works[143, 144]. According to the phase diagram proposed by Acosta *et al.* [143], the crystallographic structure of the 40BCT (R) is rhombohedral at room temperature and transforms to orthorhombic at 38 °C, to tetragonal at 53°C, and to cubic at 70 °C. The 50BCT (O) is in the orthorhombic phase at room temperature, transforms into the tetragonal phase at 29 °C, and into the cubic phase at 86 °C. The 60BCT (T) is in the tetragonal phase and has no phase transitions close to room temperature and the Curie temperature at 95 °C, where it transforms into a cubic structure. Since the compositions have different crystal structures, they also show differences in their ferroelectric properties[201]. These differences of ferroelectric properties originate from different possible directions for spontaneous polarization (6 for tetragonal, 8 for rhombohedral and 12 for orthorhombic), different ferroelastic domains (ideally, 90° domains for tetragonal phase, 109° and 71° for rhombohedral phase, and 60°

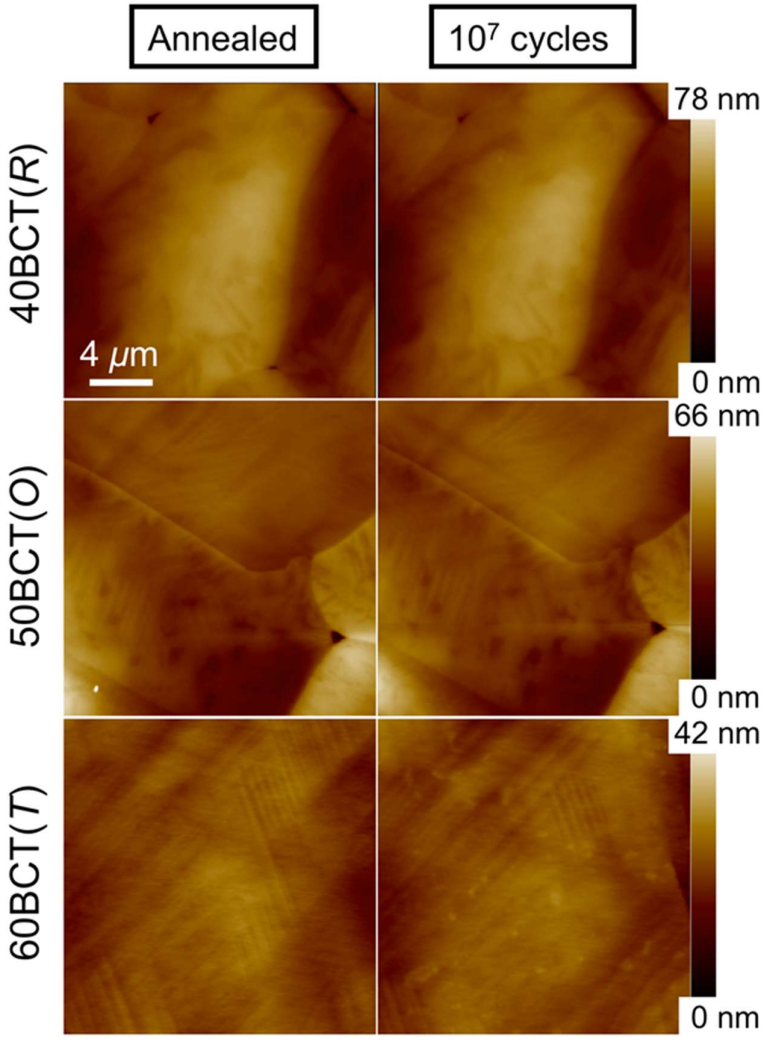

Figure 3.6 Topography images of 40BCT (R), 50BCT (O), and 60BCT (T) samples measured after annealing and after cycling. The corresponding color bar for different measurements are displayed in the right hand side of the topography images. The scale bar is the same for all displayed images.

and 120° for orthorhombic phase), different lattice distortions, and different proximities of room temperature to their closest phase transitions.

The surface morphology of 40BCT (R), 50BCT (O), and 60BCT (T) ceramics after fine mechanical polishing has been studied with AFM. Figure 3.6 displays corresponding AFM topography images, showing the flat surface of studied samples. It indicates that all three samples have been polished to similar states. Therefore, the polishing effects can be excluded when explaining the domain structure difference between the three samples. Furthermore, some macroscopic defects like minicracks and pores are invisible in Fig. 3.6, revealing that the influence of macroscopic defects on the electric fatigue behavior after poling cycles is ignorable in this work. The point defects related to the different doping concentrations in three compositions and the strain effect related to distinct structural phases are key factors for fatigue behavior. Next, functional properties studies have been performed to

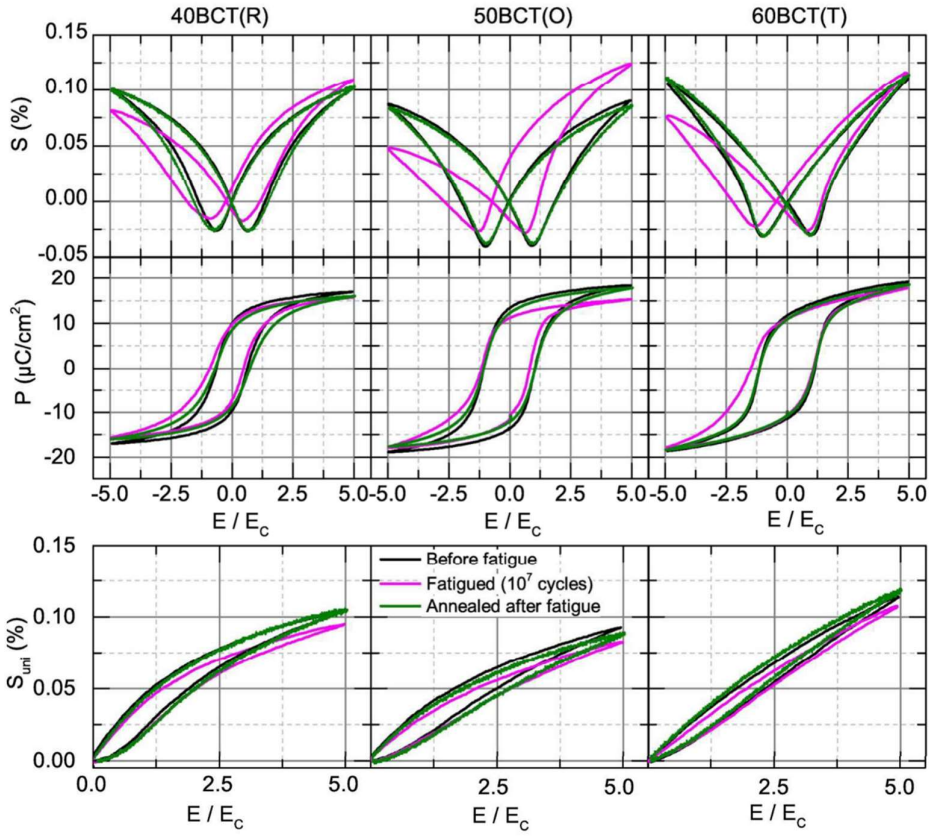

Figure 3.7 Bipolar strain and polarization and unipolar strain hysteresis curves as a function of the normalized electric field for the three investigated BZT-*x*BCT compositions, 40BCT (R), 50BCT (O), and 60BCT (T), before cycling (black), after 10^7unipolar cycles (pink), and after subsequent thermal annealing (green).

observe the fatigue of three compositions under increasing poling cycles. The degradation of the performance of the three compositions will also be investigated.

Figure 3.7 shows the bipolar strain, polarization hysteresis curves, and unipolar strain hysteresis curved as a function of the normalized electric field for three compositions in three different states: the initial annealed state, after 10^7 unipolar cycles, and after subsequent thermal annealing after cycling. The curves were measured at a cycling field of $5 \cdot E_C$ and are presented with the *x*-axis normalized to multiples of the coercive field value in order to evaluate changes to the hysteresis in a more direct manner. The bipolar hysteresis curves for all compositions show the asymmetric strain curves and the shift of the polarization curves along the abscissa axis towards the negative side of the applied electric field, demonstrating the fatigue behavior. It shows that the strain asymmetry is more pronounced in the orthorhombic 50BCT (O) composition and is less prominent in the rhombohedral and tetragonal compositions.

The effect of fatigue is also reflected in the unipolar strain curves, evident by lowering the maximum achieved strain for all compositions. However, thermal annealing of the fatigued samples at 400°C for

2 hours resulted in the full recovery of the electromechanical properties, which indicates that no permanent degradation was induced during the unipolar electric field cycling.

Figure 3.8(a) exhibits the normalized remanent polarization for all studied samples. Only a minor decrease between 2% and 4% of the initial value is visible for the first 10^4 cycles. However, the decrement of the normalized remanent polarization becomes prominent after 10^5 cycles. Compared with 40BCT (R) and 60BCT (T) samples, 50BCT (O) shows a more obvious degradation. After 10^7 cycles, the remanent polarization is reduced by about 6% for the 60BCT (T), 9% for the 40BCT (R), and 12% for the 50BCT (O). Figure 3.8(b) presents the normalized significant signal piezoelectric coefficient d_{33}^* for evaluating the effect of unipolar effect on strain output. This coefficient d_{33}^* is defined as $d_{33}^*=S_{uni}^{max}/E^{max}$, where S_{uni}^{max} is the unipolar strain at the corresponding electric field E^{max}. The normalized coefficients for 40BCT (R), and 60BCT (T) samples have a similar response to

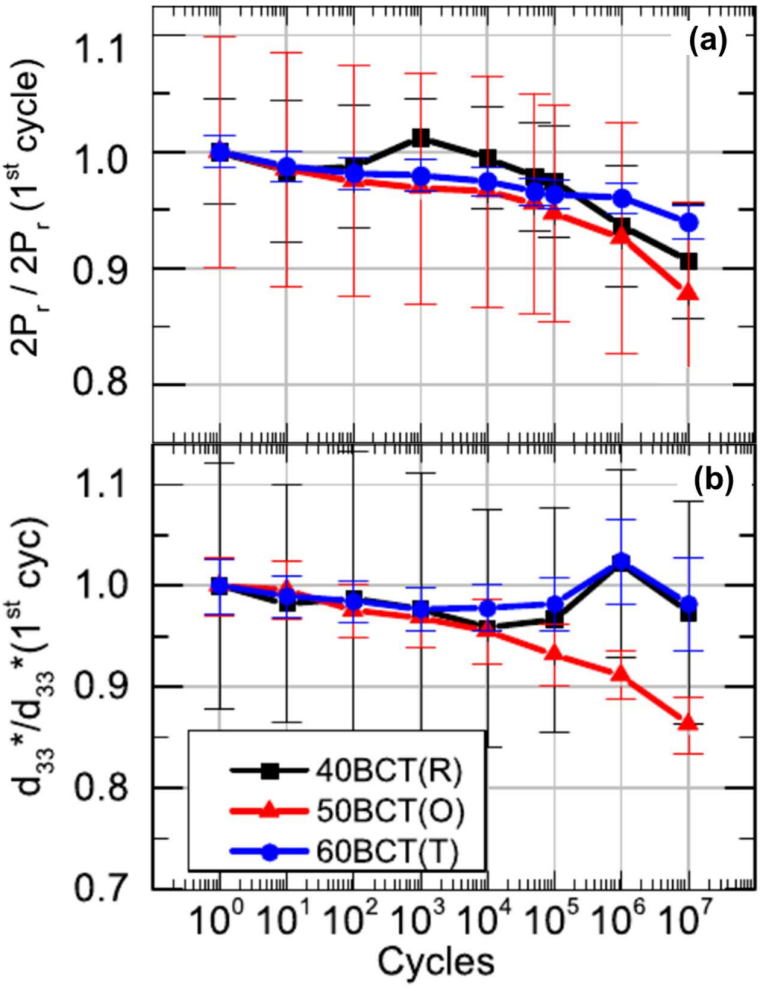

Figure 3.8 (a) The remanent polarization ($2P_r$) and (b) $\boldsymbol{d_{33}^*}$ by normalized the first cycle as a function of unipolar cycles for 40BCT(R), 50BCT(O), and 60BCT(T) samples. The error bars in this plot are exaggerated by the normalization process.

increasing unipolar cycles. It shows a small d_{33}^* reduction for the first 10^5 cycles, and a slight increase at 10^6 cycles. It is noted that this increase could be related to a change of the cycling high voltage setup (described in the Experimental Procedure section). The reduction of d_{33}^* values for 40BCT (R), and 60BCT (T) samples after 10^7 cycles are both small: 2% for 60BCT (T); 3% for 40BCT (R). The orthorhombic 50BCT (O) shows a gradual decrease throughout the entire cycling range, with a decrease of 13% of its initial d_{33}^* value after 10^7 cycles.

The unipolar electric cycling caused degradation of electromechanical properties in all three studied samples have been revealed by the results of Fig. 3.7 and Fig. 3.8. The observed features, including the increased bipolar strain hysteresis asymmetry, the decrease of remanent polarization, and the reduction of maximum achievable strain, suggest the fatigue under the unipolar electrical cycling.

Figure 3.9 shows the macroscopic images of the polished surface of samples that were taken before and after cycling with a light microscope. No cracks or pores can be observed in either the initial state or the final state after 10^7 poling cycles. These phenomena imply that the effect of macroscopic defects on the fatigue behavior of three compositions is very unlikely. However, the samples became darker after cycling (Fig. 3.9). This color change is suggested to indicate the migration of oxygen vacancies upon unipolar cycling, as observed for acceptor-doped barium titanate [7]. Interestingly, the color scale was also restored to the initial state after annealing. Based on these observations, fatigue

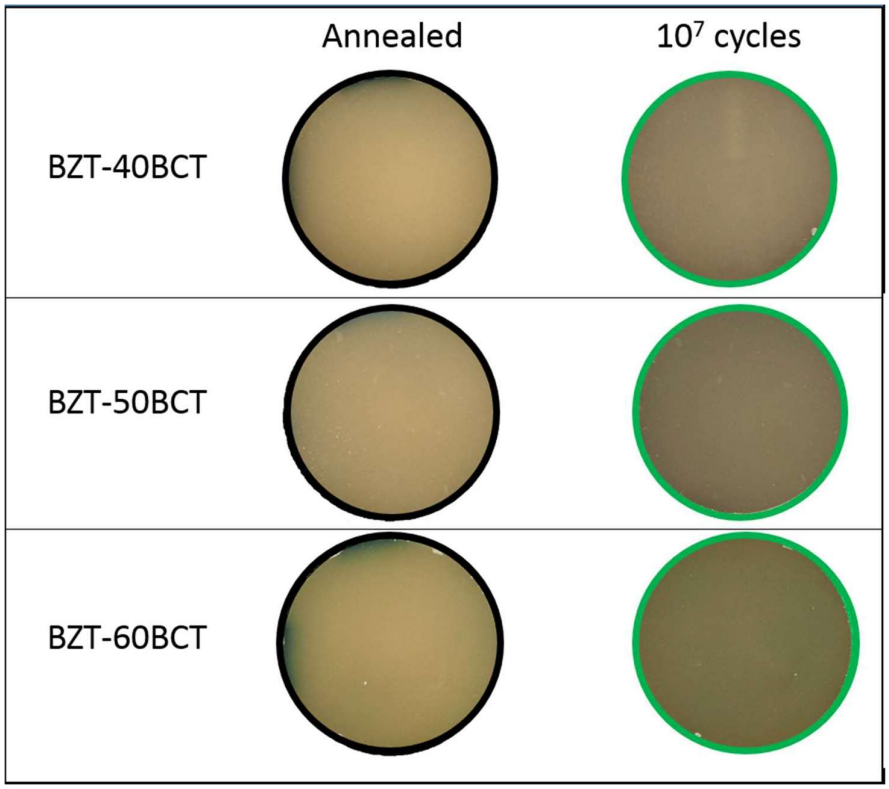

Figure 3.9 Top polished surfaces of the samples used for PFM examinations taken on an optical light microscope before and after cycling. Each sample has a diameter of 7.8 mm.

mechanisms related to the cycling-induced irreversible changes can be excluded. [236, 242] The appearance of an internal bias field and a strong strain asymmetry indicates that the fatigue mechanism for BZT-*x*BCT is likely related to the internal migration of free charge carriers.

For giving an in-depth insight on the fatigue behaviors of 40BCT (R), and 60BCT (T) samples, 50BCT (O) samples, PFM studies were conducted on ferroelectric domain structures of the three compositions before and after 10^7 cycles.

Figure 3.10 provides the obtained PFM images for all three compositions, where the lateral and vertical amplitudes are presented on the same spot of the sample before (in the annealed state) and after cycling. The corresponding topography images have been shown in Fig. 3.6. The domain morphologies for all samples were also verified in another area of each sample.

The domain patterns in 40BCT (R) are detailed in Fig. 3.10 (a) and (b). In the annealed state, wedge-shaped domains consisting of lamellar sub-domains are observed. The domain morphology changed

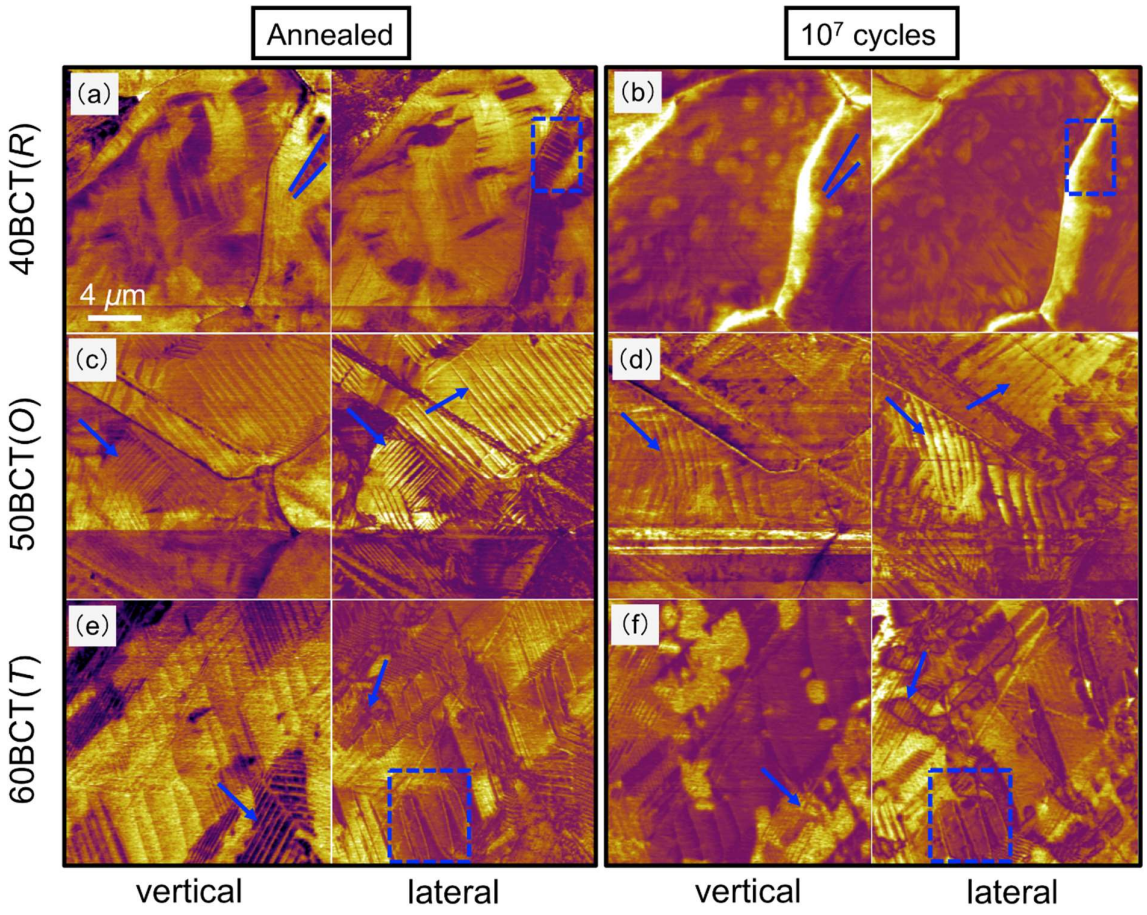

Figure 3.10 Vertical and lateral PFM amplitude images measured before cycling in the annealed state and after 10^7 unipolar cycles: (a) and (b) 40BCT (R), (c) and (d) 50BCT (O), and (e) and (f) 60BCT (T). The areas marked with blue arrows and squares highlight some of the most representative changes in the domain structures before and after poling cycles. Color bars: arbitrary.

after cycling, and the grains now seem to exhibit a single domain state. The phenomenon of single domain states in BZT-*x*BCT has been previously observed in TEM studies by Guo *et al.* [227] and Zakhozheva *et al.* [151, 153] The observed single domain developed from a multi-domain state upon the application of an *in situ* external electric field and could be achieved for several compositions with different strengths of nominal poling fields, including 40BCT (R), 50BCT (O), and 60BCT (T). The field amplitudes required to obtain the single domain state were higher for compositions with larger coercive fields, and the domain state was not stable. It reverted to a multi-domain state with an increase or removal of the applied field. Our findings indicate that the initial domain configuration will not be recovered simply by removing the field if the single domain state is achieved during unipolar cycling.

The previously described defect agglomeration fatigue mechanism suggests that domains are pinned by the accumulated defects, decreasing the fraction of irreversible contributions and reducing the electromechanical properties. However, in the 40BCT (R) sample, the domain configuration underwent a dramatic change during cycling from a multi-domain to a single-domain state. The reduced domain wall density is confirmed by reducing the zero-field permittivity $\varepsilon_r'(0)$ from 1712 at the initial state to 1561 after 10^7 cycles. [203] Although the exact reason for this behavior remains unclear, it seems possible that a single domain state, or a state with lower domain wall density, is stabilized by the charged defects agglomerating at the grain boundaries. A detailed *in situ* microscopic study is needed for the understanding of this phenomenon.

In the case of 50BCT (O) (Fig. 3.10 (c) and (d)), an abundance of lamellar and wedge-shaped domains is observed in both the annealed and the cycled state. It was previously reported that the initial domain configuration of this composition also contains miniaturized nano-domains within the lamellar arrangement. [158, 249] However, the average size of such nano-domains was reported to be between 20-100 nm, and thus is hard to be resolved in PFM images in Fig. 3.10. Moreover, these nano-domains were reported to disappear once the material was poled, leaving a micrometer-range multi-domain configuration. [42, 151] Since the electric field applied for the cycling is sufficiently strong to pole the material during the first cycle, it is assumed that the initial nano-domains are not present during the electric cycling and have no influence on the fatigue behavior of this composition.

After unipolar cycling (Fig. 3.10(d)), the domains' overall configuration changed and some small or fragmented domains were observed. Although a single domain state has also been reported for this composition [227], this was not observed in this work. The newly-formed, small, fragmented domains are confirmed by the increased parameter $\varepsilon_r'(0)$ from 1590 at the initial state to 1629 after 10^7 cycles, which indicates increased domain wall density. Domain fragmentation upon cycling was previously observed in PZT using *in situ* TEM [250] and related to decreased irreversible contributions.

It should also be considered that the composition 50BCT (O) at room temperature is very close to the phase transition to the tetragonal structure. The applied electric field or even slight changes in the temperature could cause a premature phase transition, giving rise to the differences observed in the domain configuration after cycling.

In the case of 60BCT (T) (Fig. 3.10 (e) and (f)), the lamellar domain configuration found before cycling was still present after cycling. The PFM picture of the cycled state reveals that large domains were unaffected; however, new small fragmented domains were introduced. It is confirmed by the increased parameter $\varepsilon_r'(0)$. This behavior is qualitatively the same as observed in the 50BCT(O) sample. However, the general stability of the overall domain morphology is an indication that intrinsic contributions play a more significant role in this composition.

3.2.3 Conclusion

The unipolar fatigue behavior of three BZT-xBCT compositions with different crystallographic structures, *i.e.*, 40BCT (R), 50BCT (O), and 60BCT (T), was evaluated. Domain wall pinning by agglomerated charge carriers is suggested to be the dominant fatigue mechanism in all compositions and could be removed by mild thermal annealing (400 °C for 2 hours). However, the three compositions with distinct crystal structures had different responses to the unipolar cycling. The orthorhombic 50BCT (O) was demonstrated to be the most susceptible composition, with a 12% drop in P_r and loss of 13% for d_{33}^* 10^7 unipolar cycles. The tetragonal composition 60BCT (T) exhibited the best fatigue resistance, with a slight drop of 6% in P_r and a loss of 2% for d_{33}^*. The 40BCT (R) also showed a fatigue resistance behavior with the degradation of 9% and 3% for P_r and d_{33}^*, respectively.

PFM studies were performed to relate the fatigue behavior to the different strain mechanisms of each of the three studied compositions. PFM domain maps indicate that the high amount of extrinsic contributions to strain made orthorhombic 50BCT (O) and rhombohedral 40BCT (R) compositions most susceptible to fatigue during unipolar cycling. 50BCT (O) shows a domain fragmentation with increased domain wall intensity upon cycling. The fatigue response of 40BCT (R) was additionally affected by the formation of a single domain state, which increased the fraction of irreversible contributions and partially compensated the reduction of the electromechanical properties. Domains maps show that the tetragonal composition 60BCT (T) has high intrinsic contributions to strain, making it more resistant to electric fatigue, resulting in relatively stable electromechanical properties.

Contributions to this work:

Xijie Jiang (TUDa) carried out the PFM specimen preparation, PFM characterization, and related data processing. Na Liu (TUDa) and Christian Dietz (TUDa) offered help in PFM characterization. Virginia Rojas (TUDa) synthesized the BZT-0.5BCT ceramics, and performed the SEM

measurements, and studied macroscopic functional behaviors. Christian Dietz (TUDa) and Robert W. Stark (TUDa) supervised and oversaw this work. All authors discussed the results and contributed to this work.

3.3 Probing the domain structure of relaxor $Na_{1/2}Bi_{1/2}TiO_3$-6$BaTiO_3$ composites with ZnO inclusions*

Tremendous efforts have been made to advance lead-free materials to replace hazardous lead-containing materials. [185] A specific focus is on piezoceramics, which is widely used for piezoelectric applications and modern electronic components. Lead-free $(Na_{1/2}Bi_{1/2})TiO_3$ (NBT)-based solid solutions, [185], for example with $BaTiO_3$ (BT), have been promising candidates due to their good piezoelectric property, excellent reproducibility, and high maximum dielectric constant temperature T_m (300 °C). This NBT-BT system has a morphotropic phase boundary (MPB) at a BT content of 6–7%, wherein the material possesses relaxor ferroelectric properties and is ideal for high-power applications. [22, 251] X-ray and neutron scattering techniques studies close to the MPB region indicated a pseudocubic symmetry in average. [252-254] While transmission electron microscopy (TEM) [254, 255] and nuclear magnetic resonance of sodium [251, 256] results evidenced the non-cubic structure at the local scale of NBT-BT ceramics, such a coexistence of tetragonal and rhombohedral phases. The corresponding electric field-temperature phase diagram [257] and stress-temperature phase diagram [258] of $0.96(Na_{1/2}Bi_{1/2})TiO_3$-$0.06BaTiO_3$ (NBT-6BT) ceramics have been constructed to describe the field and tress induced transitions.

However, a noticeable drawback for the NBT-6BT system is the low depolarization temperature (T_d) at around 100 °C, [185, 259] where a noticeable reduction of macroscopic piezoelectric properties takes place due to a ferroelectric to relaxor transition. [260] Therefore, the T_d determines the upper-limit working temperatures of the NBT-6BT ceramics, hindering their practical applications at elevated temperatures.

Numerous attempts have been conducted to increase or even eliminated the T_d without reducing the macroscopic piezoelectric properties. General methods include solid solution modification and chemical doping. However, it has been found that the good piezoelectric properties and enhanced thermal stability in these methods are closely correlated and hard to decouple. [12, 185, 261] This could be because the stability of ferroelectric domains indicated by the depolarization temperature contrasts the anisotropic flattening of the Gibbs free energy, causing an improved piezoelectric response. [12, 262] Recently, a breakthrough was reported demonstrating thermal stability with the thermal depolarization up to 130°C without decreasing the piezoelectric properties in a 3-0 type composite, based on the relaxor ferroelectric NBT-6BT and semiconductor ZnO was demonstrated. [263] The enhanced thermal stability was interpreted with a charge order model, showing that the free electrons of ZnO partially compensate for the depolarization fields at pores and grain boundaries. However, the exact mechanism remains unclear and needs further characterizations in detail. So far, microscopic ferroelectric domain structure studies using PFM have rarely been performed to probe

*Part of this chapter has been published in Ref. [264].

underlying mechanisms of enhanced thermal stability.

In this study, NBT-6BT:*x*ZnO composites were prepared and investigated with PFM and KPFM at room temperature. Prior to PFM characterizations, the thermal depolarization behavior of the composites was assessed with temperature-dependent in situ d_{33}, dielectric permittivity, and large-signal strain measurements. In order to understand the effects of ZnO inclusion, PFM results of pure NBT-6BT ceramics and NBT-6BT:0.1ZnO composites were obtained and compared in terms of the ferroelectric domain structure, relaxation of poling regions, and local hysteresis loops. The thermal strain effects originated from the mismatch of thermal expansion between ZnO, and the NBT-6BT matrix is evaluated and suggested to influence the enhanced thermal stability of NBT-6BT:0.1ZnO composites.

3.3.1 Experimental

$0.94(Na_{1/2}Bi_{1/2})TiO_3$-$0.06BaTiO_3$ powder was prepared by a conventional solid-state synthesis method. Stoichiometric amounts of powders Bi_2O_3 (99.975 %), $BaCO_3$ (99.8 %), Na_2CO_3 (99.5 %), and TiO_2 (99.6 %) (all Alfa Aesar), were weighed and milled for 24 h in ethanol at 250 rpm in a planetary ball mill (Fritsch Pulverisette 5). The dried powders were calcined in closed alumina crucibles at 900 °C for 3 h with a heating rate of 5 K min^{-1}. The obtained NBT-6BT powder was ground by mortar and pestle, milled for 24 h in ethanol at 250 rpm, and subsequently dried. The powder was sieved with a 160 µm nylon sieve and annealed in closed alumina crucibles at 1100 °C for 3 h to coarsen the particles.

The annealed NBT-6BT powder was ground by mortar and pestle, sieved (160 µm sieve), and weighed together with ZnO nano-sized powder (25 nm, 99.5 %, PlasmaChem GmbH) to form mixtures with NBT-6BT:xZnO mole ratios of x= 0, 0.1, 0.2, 0.3, and 0.4. A final milling step of 24 h in ethanol at 250 rpm was used to obtain the final powder mixture.

For analytical purposes, disks with a diameter of 10 mm were manually cold-pressed, cold isostatically compacted at 40 MPa, and sintered in closed alumina crucibles at 1012 °C for 1 h with a heating rate of 9 K min-1. As a reference,10mm NBT-6BT disks from non-coarsened powder were sintered in closed alumina crucibles at 1150 °C for 3 h with a heating rate of 5 K min-1. To avoid volatilization of bismuth and sodium during sintering, all the samples were embedded in atmospheric powders with the same composition.

Using a MFP-3D atomic force microscope (Asylum Research, Santa Barbara), PFM and KPFM measurements were performed to characterize the local domain morphology and surface potential, respectively. Prior to the measurement, bulk ceramics' surface was finely polished in the same way as BZT-0.5BCT ceramics (See details in the experimental part of Section 3.1). All measurements were acquired using electrically conductive cantilevers (ASYELEC-01, Asylum Research, Santa Barbara)

with a nominal free resonance frequency of 70 kHz and a nominal force constant of 2 N m^{-1}. Images were taken at a scan rate of 0.5 Hz with a resolution of 256 × 256 pixels. For PFM measurements, an ac driving voltage of 3 V (peak amplitude), and a drive frequency close to the tip-sample contact resonant frequency, which was approximately 300 kHz in the single frequency PFM mode were used, while KPFM was performed in standard lift mode using a lift height of 50 nm.

The microstructure was characterized by scanning electron microscopy (SEM) (Philips XL30 FEG). Polarization and strain as a function of electric field were measured with a triangular field up to 6 kV mm^{-1} at 1 Hz using a Sawyer-Tower circuit equipped with an optical sensor. The same electric field was also used to investigate the temperature range between 25 and 140 °C with a TF Analyzer 2000 (AixACCT systems). Samples were poled at room temperature for 20 min at 6 kV mm^{-1}, 24 h before measurement.

3.3.2 Results and Discussions

The microstructure of the prepared NBT-6BT:*x*ZnO composites was firstly studied by SEM. Figure 3.11 (a) and (b) correspond to SEM images of NBT-6BT:0.1ZnO and NBT-6BT:0.4ZnO composites acquired by the equipped backscattered electron detector. Two distinct solid phases can be identified in both SEM images: dark isolated grains and a bright continuous matrix. Unlike the common SEM secondary electron signal, which gives the topographical information of the surface, the backscattered electron signal can also provide compositional information of the material because the fraction of the back scattered electrons is dependant on the atomic number of the atoms on the sample surface: the larger the atomic number, the brighter the image. Therefore, the dark grains in SEM images mainly belong to the ZnO inclusion. Please note that a small portion of the dark regions are pores because the backscattered electron signal reflected in this area is relatively weak. The grains of the ZnO phase feature planar surfaces and have a grain size independent of composition, while the grain size of the NBT-6BT matrix decreases with increasing ZnO content, as evidenced in the inset of Fig. 3.11(b).

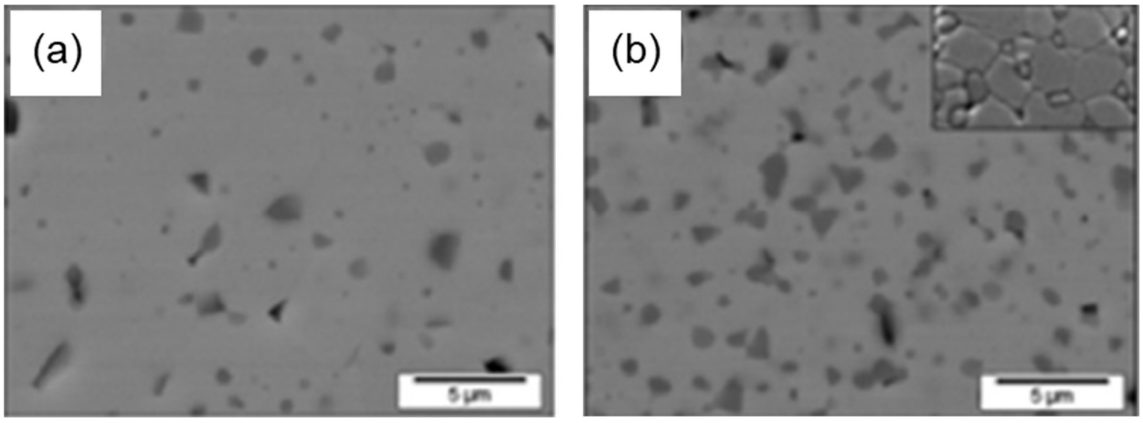

Figure 3.11 SEM backscattered electron signal of sintered, ground, and polished NBT-6BT:*x*ZnO composites: (a) x =0.1, (b) x =0.4. A thermally etched specimen is presented in the inset of (b).

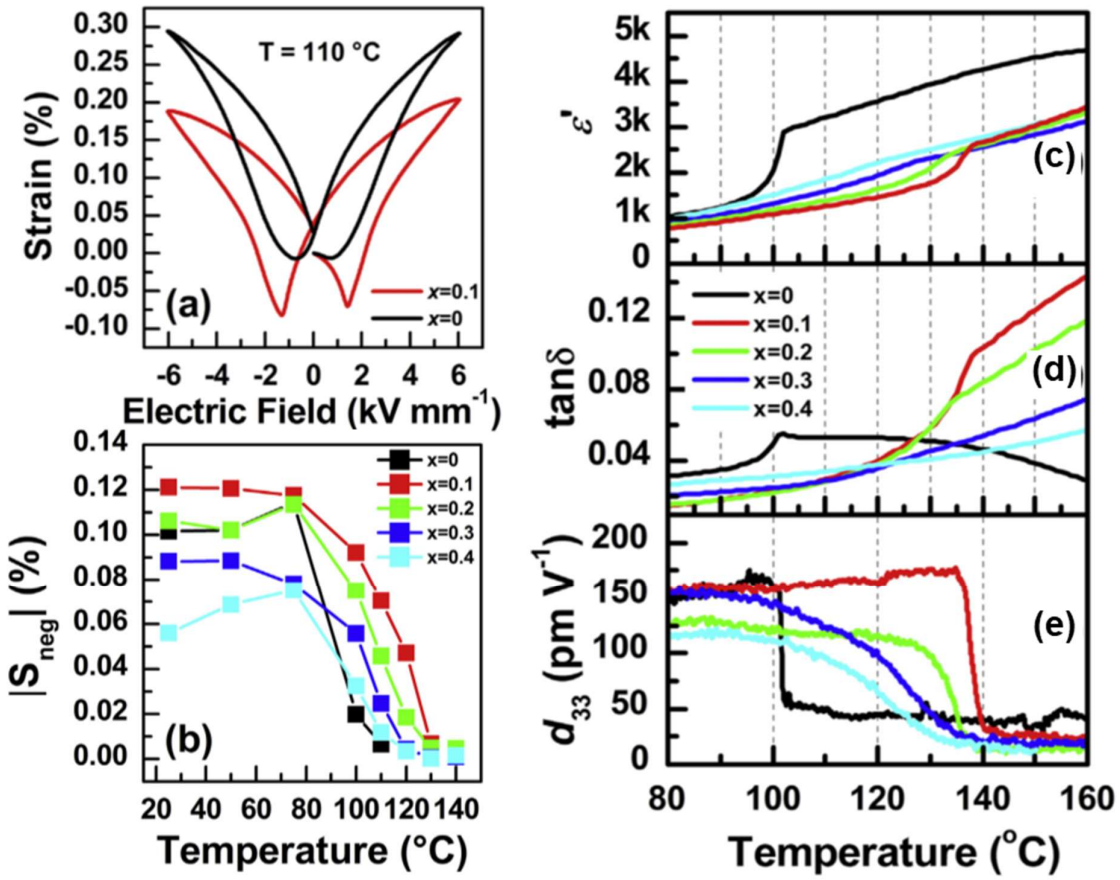

Figure 3.12 (a) Difference between a "butterfly-shaped" (x = 0.1) and a "sprout-shaped" (x = 0) isothermal strain hysteresis loop measured at 110 °C with a frequency of 1 Hz. (b) Negative strain extracted from isothermal bipolar strain hysteresis loops measured at different temperatures with a frequency of 1 Hz. The temperature-dependent relative permittivity (c), loss factor (d), and piezoelectric coefficient (c) of poled NBT-6BT:xZnO composites.

The transition temperature from the induced long-range ordered ferroelectric state into the non-polar ergodic relaxor state ($T_{F\text{-}R}$) serves as an upper bound for depolarization.[260, 265] An induced ferroelectric state is typically characterized by square-shaped polarization and butterfly-shaped strain loops, while the ergodic relaxor state is defined by slim polarization and sprout-shaped strain hysteresis loops with diminishing remanent polarization P_{rem} and negative strain S_{neg}. The different shapes are exemplified in Fig. 3.12. Figure 3.12 (a) indicates that, at 110 °C, the NBT-6BT is already in the ergodic phase (above $T_{F\text{-}R}$), while the NBT-6BT:0.1ZnO is still in the non-ergodic phase (below $T_{F\text{-}R}$). In order to estimate the depolarization temperature, isothermal hysteresis loops were further analyzed to measure the S_{neg} as a function of temperature. The results are depicted in Fig. 3.12 (b). It shows that S_{neg} for x=0.1 is the highest at all temperatures and steadily diminishes with increasing ZnO content. For all compositions, S_{neg} decreases as a function of temperature with rather pronounced drop between 90 °C for the pure NBT-6BT sample and 130 °C for the composite with x=0.1. Figure 3.12 (c), (d) depict the real part of relative dielectric permittivity (ε') and the loss factor (tanδ) for 80 to

160°C for poled samples measured at 10 kHz and recorded during heating. The inflection point in Fig. 3.12 (c), as well as the small peak in loss factor in Fig. 3.12 (d), implies the transition temperature from ferroelectric to ergodic relaxor (T_{F-R}).[260, 265] For the NBT-6BT material without ZnO, this temperature is determined to be about 100°C. In contrast, this transition for NBT-6BT:*x*ZnO composites is broadened and shifted to higher temperatures. Interestingly, the temperature increases to 138 °C for x=0.1 and then decreases with increasing ZnO content. Figure 3.12 (e) shows the piezoelectric coefficient d_{33} as a function of temperature (T), where the depolarization points T_d can be determined with the infection point of smooth curves. The piezoelectric coefficient of NBT-6BT without ZnO inclusion first changes slightly as a function of temperature and then drops abruptly at T_d =99 °C. T_d is shifted to 136 °C for x =0.1 and decreases with a further increase of the ZnO content. This trend matches well with that observed in the ε' (T) and tanδ (T) data. According to the literature [266, 267], the trend of decreasing depolarization temperature with increasing x can be attributed to the strain imcompatibility between elastically-hard inclusion and the matrix. These macroscopic ferroelectric and electromechanical studies unambiguiously demonstrate an improved temperature stability of NBT-6BT with ZnO inclusion, which is significant for practical applications like actuators in car engines.

Since NBT-6BT:0.1ZnO composites show the highest depolarization temperature, in the following part, the ferroelectric domain structure, relaxor behavior, and local ferroelectric hysteresis loops of NBT-6BT ceramics and NBT-6BT:0.1ZnO composites will be compared using PFM.

Figure 3.13 displays the surface topography of a 6 μm×6 μm region of the pure NBT-6BT and corresponding vertical and lateral piezoresponse and KPFM results. The response in the amplitude of the PFM signal is related to the local magnitude of the piezoelectric coefficient, while the phase shift with respect to the excitation is a measure of the out-of-plane polarization direction. Dark regions in the topography image denote the pores at the grain boundaries. From the phase contrast in both vertical (b) and lateral (e) directions, the domain structure is invisible, presumably due to the absence of long-range order domain structure in the relaxor NBT-6BT ceramics, of which polarized nanoregions play the key role for the ferroelectric properties. For the amplitude contrast in vertical (c) and lateral (f) directions, grains have different strain responses due to different crystallographic orientations. The KPFM image of the box region of (a) is displayed in (d). The contrast is coherent except the pore region, of which the contrast is darker than other regions, revealing a smaller potential.

With the addition of ZnO, PFM results in Fig. 3.14 clearly show the change of domain structure in the NBT-6BT matrix. Figure 3.14 (a) depicts the topography of a 6 μm×6 μm region of NBT-6BT:0.1ZnO composites. Two ZnO grains locating at the grain boundary (big) and inside the NBT-6BT grain(small) can be indexed. The size of the ZnO grain is similar to the measured size in the SEM image of NBT-6BT:0.1ZnO composites in Fig. 3.11 (a). The existence of the ZnO grains can be unambiguously proved through a surface contact potential difference (CPD) between the ZnO grain

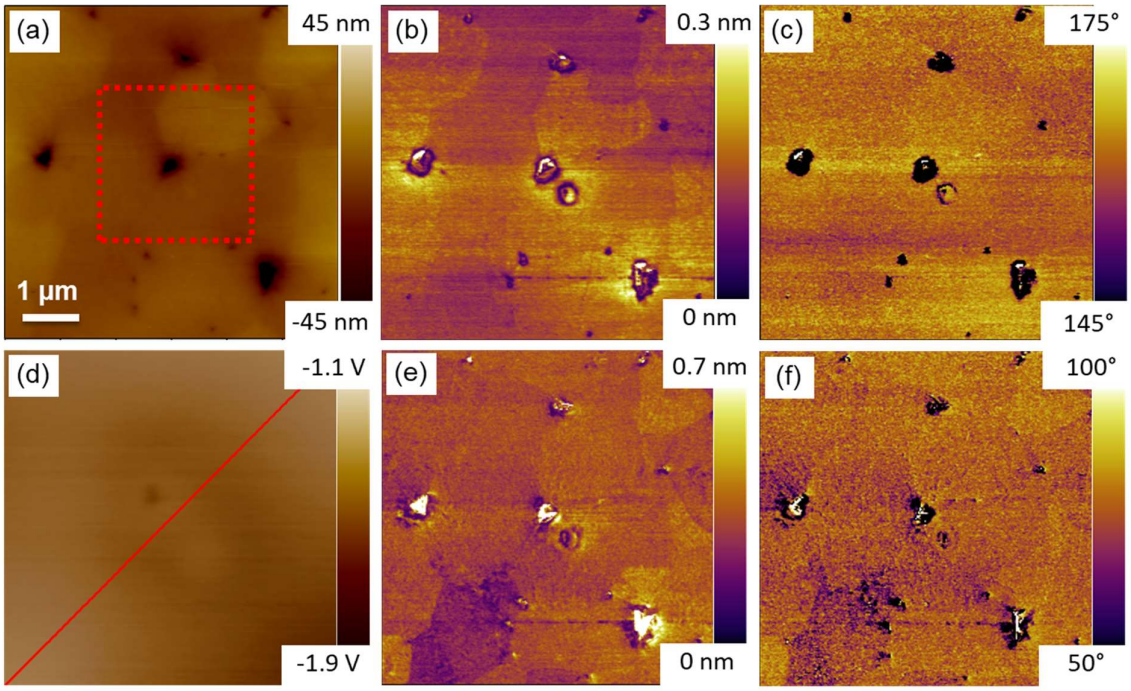

Figure 3.13 Surface topography (a), PFM vertical amplitude (b) and phase (c), KPFM (d), and PFM lateral amplitude (e) and phase (f) images of annealed NBT-6BT samples at room temperature. (d) is the KPFM image of the box region in (a).

and the NBT-6BT matrix as measured with KPFM in Fig. 3.14 (d). Since the work function of ZnO is higher than that of the NBT-6BT matrix, the contact potential difference is smaller in the ZnO region, resulting in a brighter contrast of ZnO than the matrix. The PFM amplitude in Fig. 3.14 (b, e) and phase images in Fig. 3.14 (c, f) of NBT-6BT:0.1ZnO exhibit a clear contrast. In both cases, lamella-like domain structure with distinct contrasts was observed in the adjacent matrix grains, which cannot be seen in the topography images. PFM has also been performed to study another region where the ZnO grain is inside the NBT-6BT, as shown in Fig. 3.14 (g-k). Lamella domains also emerge in the NBT-6BT grain. This behavior may result from higher stress developed at the adjacent grain, which requires a higher concentration of domains to relieve the stress. These results suggest a locally-induced ferroelectric state in the adjacent NBT-6BT matrix, facilitated by the ZnO inclusion.

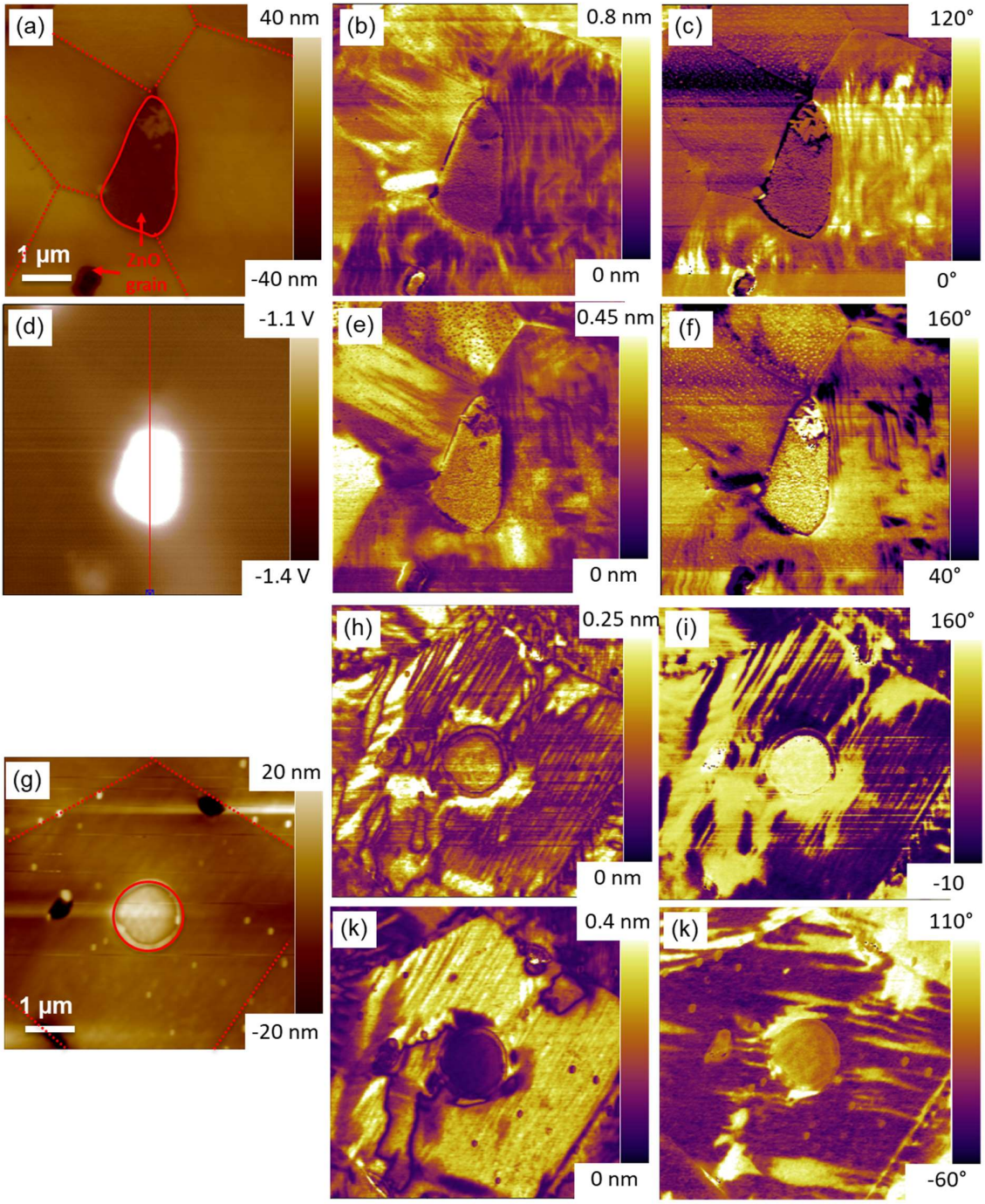

Figure 3.14 (a-f) are the surface topography, PFM vertical amplitude (b), vertical phase (c), KPFM (d), lateral amplitude (e), and lateral phase (f) images of a region of annealed NBT-6BT:0.1ZnO composites at room temperature where ZnO grain locates at the grain boundary. (g-k) correspond to surface topography, PFM vertical amplitude, vertical phase, lateral amplitude, and lateral phase images of another region where the ZnO grain is in a NBT-6BT grain.

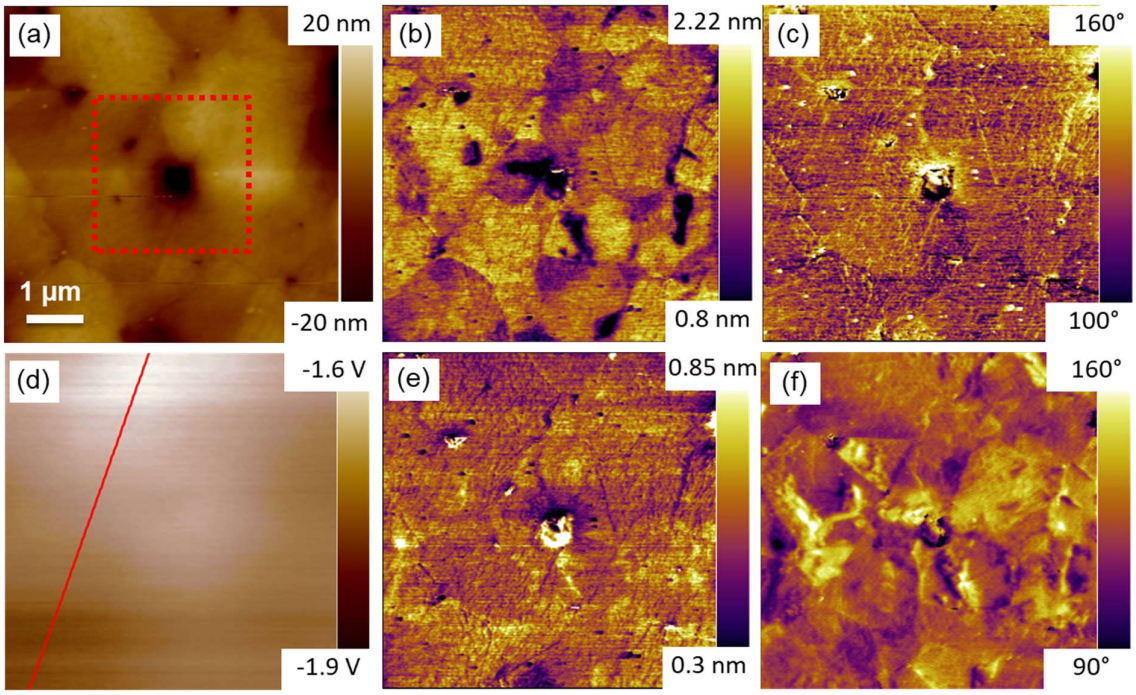

Figure 3.15 Surface topography (a), piezoresponse force microscopy vertical amplitude (b) and phase (c), KPFM (d), and lateral amplitude (e) and phase (f) images of macroscopically poled NBT-6BT samples at room temperature. (d) is the KPFM image of the box region in (a).

Figures 3.15 and 3.16 correspond to the PFM results on macroscopically poled NBT-6BT samples and NBT-6BT:0.1ZnO composites. Apart from pores and regions close to grain boundaries, NBT-6BT samples, PFM phase, and amplitude maps show uniform contrast throughout the studied region, indicating that the NBT-6BT domain is poled to the same orientation. Thanks to the poling effects, the amplitude difference between grains with varied orientations is not as evident as that of annealed samples. For NBT-6BT:0.1ZnO composites, the polarization direction of the ferroelectric NBT-6BT matrix will be re-oriented as the electric field is applied. However, this response is absent for no-ferroelectric ZnO. Therefore, an apparent contrast difference can be observed in PFM maps, particularly in the phase maps.

As shown in Fig. 3.16 (c), the ZnO grain has a darker contrast than the adjacent grains, of which the polarization direction is fully oriented to the poling field. Furthermore, due to the electric poling, the lamella-like domain structure becomes less visible than the annealed samples. A noticeable contrast difference can be seen in the PFM results in Fig. 3.16 (d), demonstrating that the intrinsic work function of the materials remains unchanged after poling.

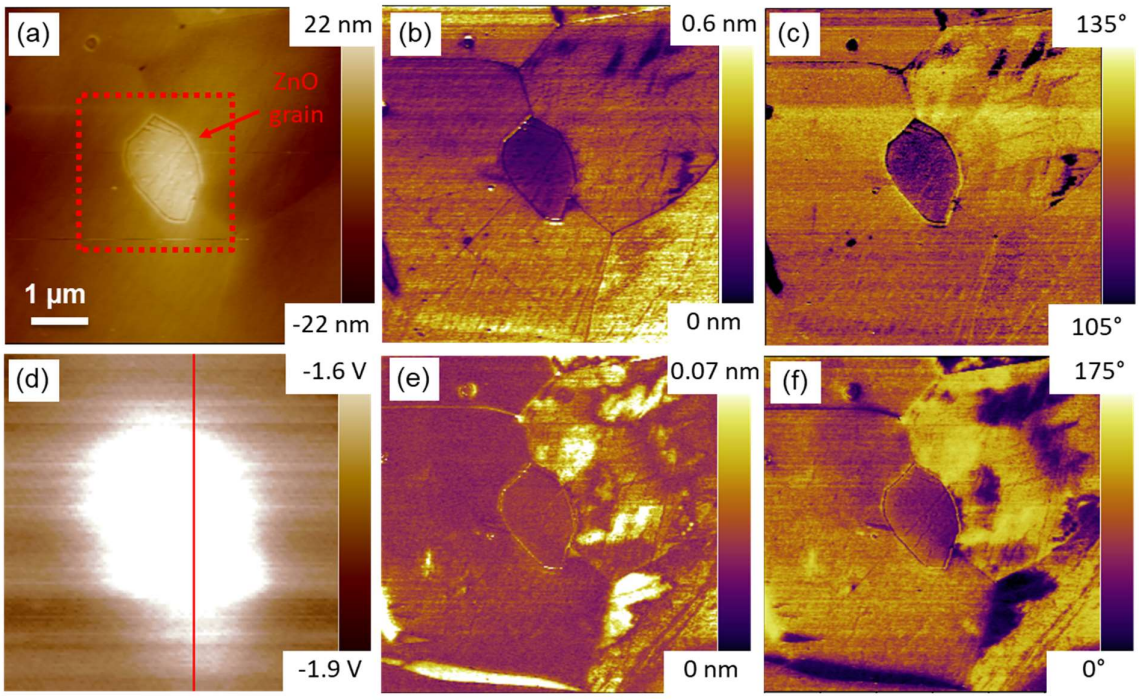

Figure 3.16 Surface topography (a), PFM vertical amplitude (b) and phase (c), KPFM (d), and PFM lateral amplitude (e) and phase (f) images of macroscopically poled NBT-6BT:0.1ZnO composites at room temperature. (d) is the KPFM image of the box region in (a).

Next, the influence of the ZnO inclusion in relaxation properties of domain structure was studied with PFM. For comparison, both NBT-6BT ceramics and NBT-6BT:0.1ZnO composites were poled with -50 V tip. The time-dependant domain evolution was investigated. Figure 3.17 shows the PFM vertical amplitude (red box) and phase images (green box) of the pure NBT-6BT samples as a function of time, respectively. The rectangle region was poled, evidenced by the brighter contrast compared to other regions. It shows that the contrast of poled region remains unchanged after 3.5 hours, indicating that the poled state stays. However, after 3.75 hours, the poled region can not be visualized in both vertical amplitude and phase images, showing a similar contrast to the neighboring regions. It reveals that the poled state is relaxed after between 3.5 hours and 3.75 hours. After 22 hours, the poled region disappears and randomly oriented domains are visible.

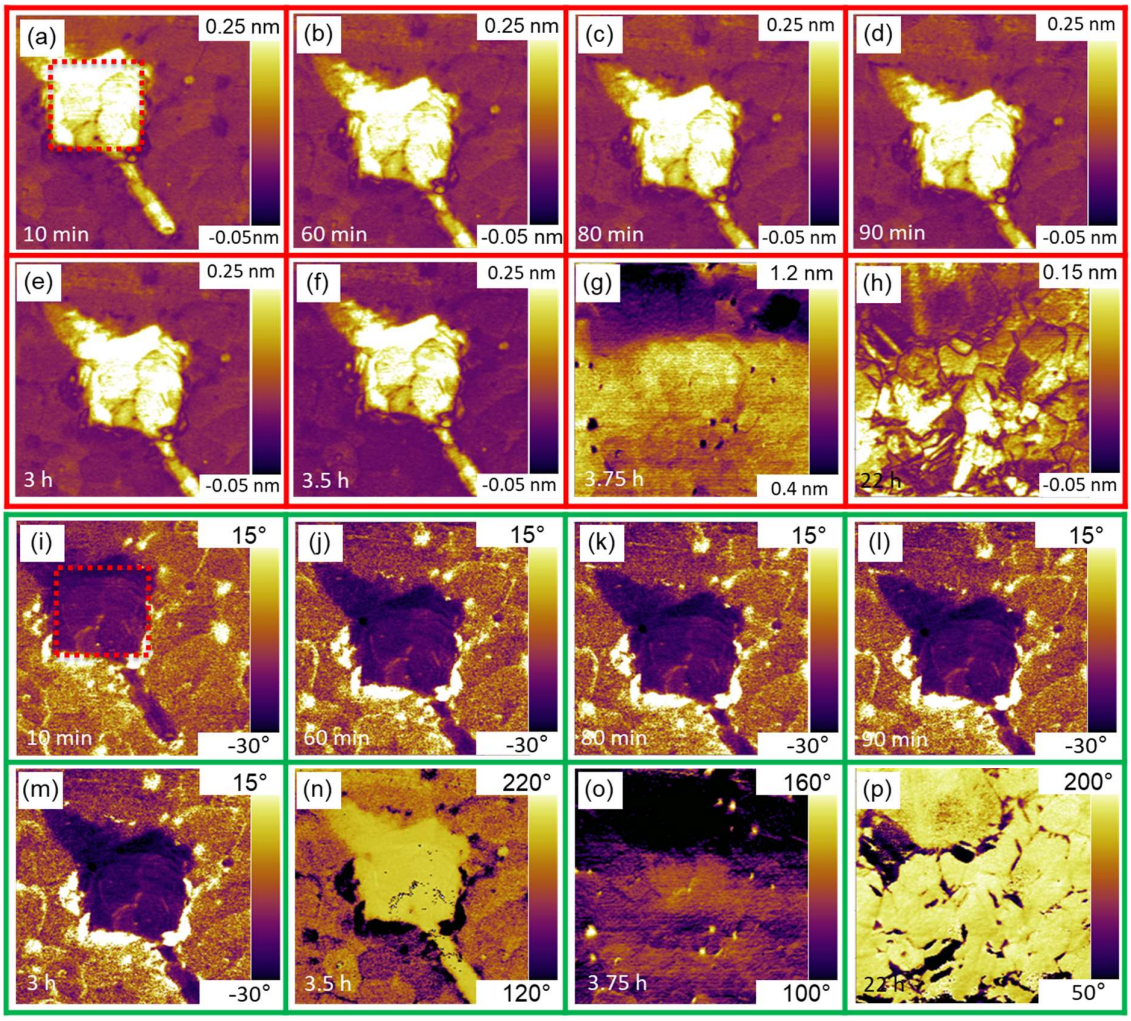

Figure 3.17 The relaxation process of -50V tip-poled NBT-6BT ceramics (10 μm×10 μm) with PFM vertical amplitude (red box) and vertical phase (green box). The rectangle-like region was poled with an AFM tip.

Figure 3.18 shows the domain evolution of the NBT-6BT:0.1ZnO composites with the same time scale. In both vertical amplitude and vertical phase images, it shows that the domain structure of poled rectangle region is almost unchanged. Compared to NBT-6BT ceramics, the poled state did not relax after 3.5 hours, even after 8 hours. The material still keeps the poled stated after 22 hours. These PFM results directly observe domain evolution after poling, clearly proving that the ZnO inclusion significantly influences the relaxation behavior of the NBT-6BT ceramics. The enhanced stability of poled regions at room temperature could be attributed to two mechanisms: firstly, the free charge carriers contributed by ZnO could partially compensate the depolarization field in NBT-6BT:0.1ZnO composites, which has been discussed in the literature. In addition to this, it is suggested that the strain effect is critical for the observed enhanced stability as well. Upon cooling from the sintering temperature, thermal strain occurs due to a difference in thermal expansion coefficient between ZnO ($7 \times 10^{-6}\,K^{-1}$) and NBT-6BT ($4.3 \times 10^{-6}\,K^{-1}$). The compressive stress is thus applied to the NBT-6BT

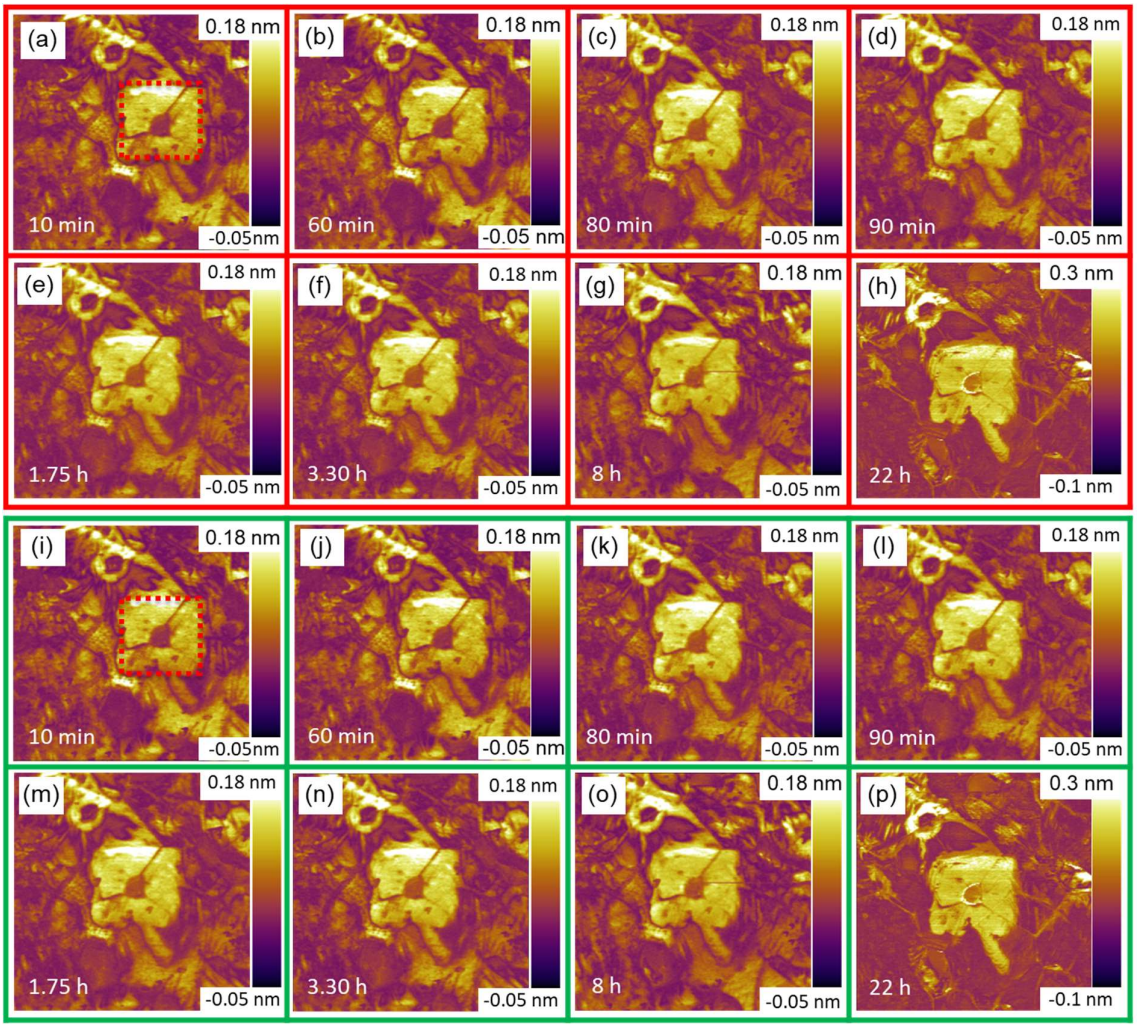

Figure 3.18 The relaxation process of -50V tip-poled NBT-6BT:0.1ZnO composites (10 μm×10 μm) with PFM vertical amplitude (red box) and vertical phase (green box). The rectangle-like region was poled with an AFM tip.

matrix, inducing a long-range ferroelectric order, as depicted in Fig. 3.14. The induced ferroelectric phase is energetically stable and is expected to harden the domain structure.

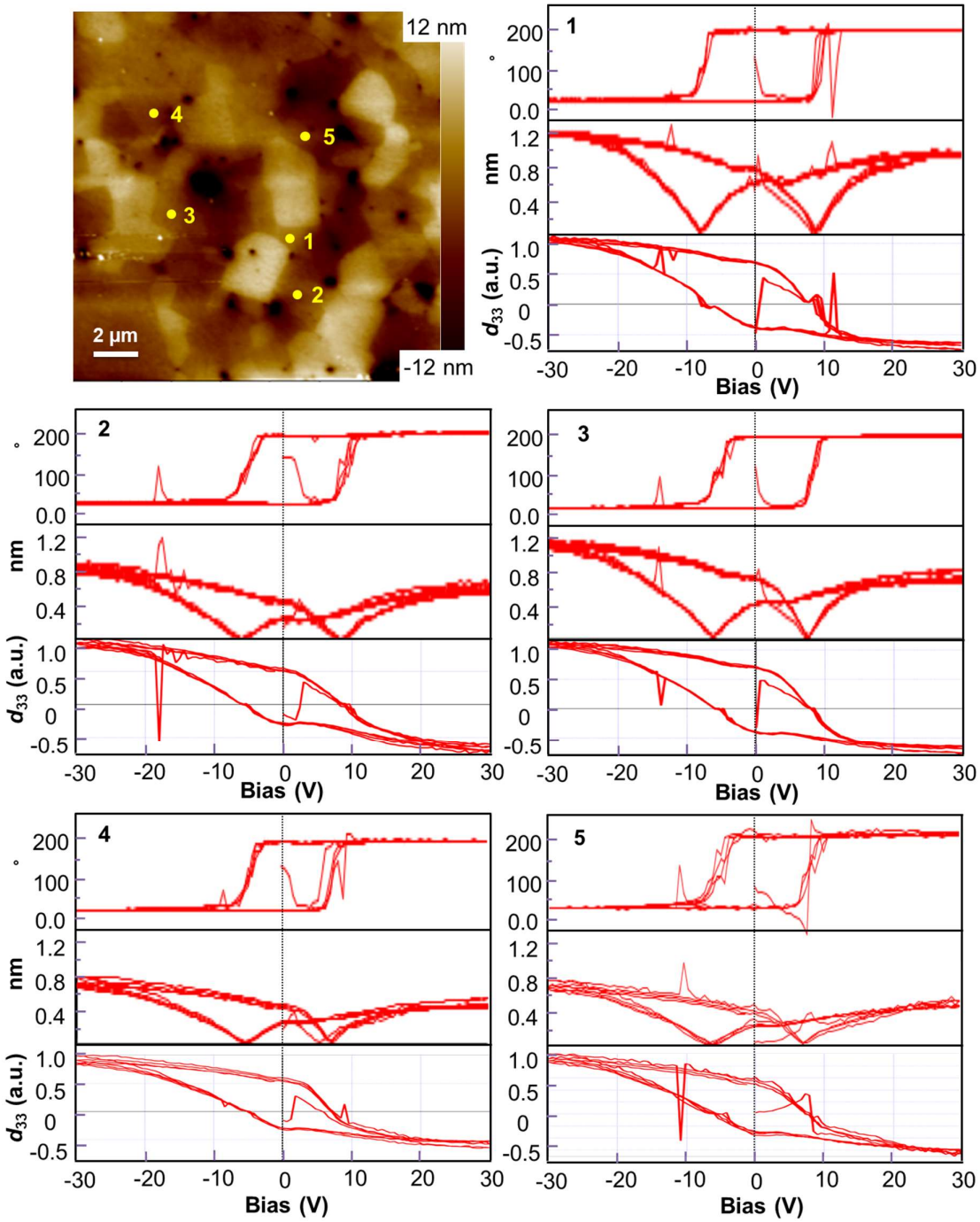

Figure 3.19 Local PFM phase (top), PFM amplitude (middle) and piezoelectric coefficient (bottom) measured from different position of NBT-6BT ceramics.

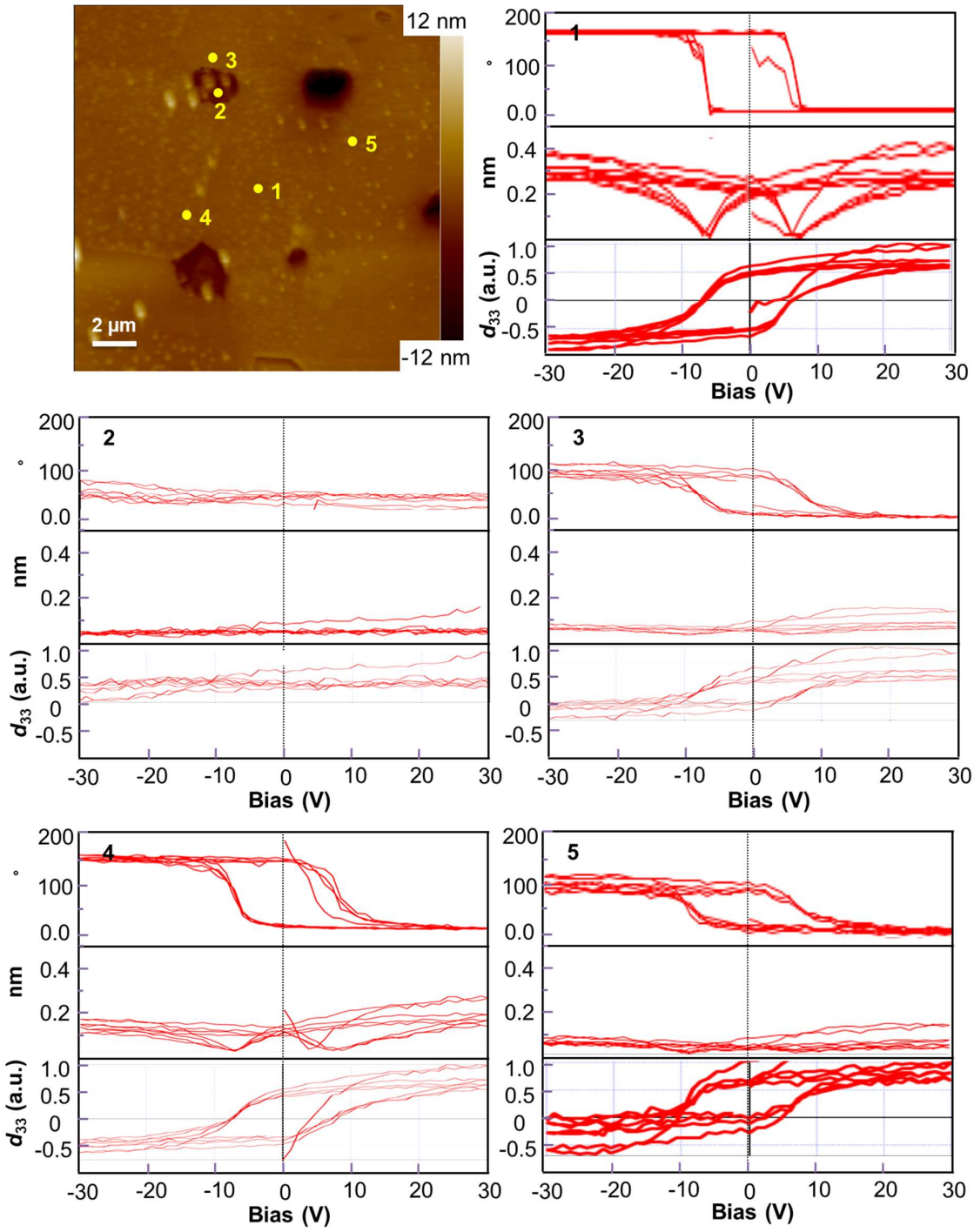

Figure 3.20 Local PFM phase (top), PFM amplitude (middle) and piezoelectric coefficient (bottom) measured from different position of NBT-6BT:0.1ZnO composites.

Figure 3.19 and Figure 3.20 exhibit local hysteresis loops measured at different positions of NBT-6BT samples and NBT-6BT:0.1ZnO composites, respectively. For NBT-6BT samples, hysteresis loops at 5 different regions have been extracted. The shape of all presented hysteresis loops in Fig. 3.19 is similar to the typical hysteresis loop of ferroelectric materials, demonstrating the ferroelectric

characteristics of NBT-6BT ceramics at room temperature. The parameters of 5 hysteresis loops, including the saturation polarization, remanent polarization, and coercive field, are almost the same, indicating a good uniformity of the ferroelectric behavior of NBT-6BT ceramics. However, the ferroelectricity of NBT-6BT ceramics is significantly modified with the inclusion of ZnO grains. In Fig. 3.20, except the position 2 in the ZnO grain, the hysteresis loops are in different shapes with each other. The hysteresis loop of position 1 in the central part of a NBT-6BT grain has a typical shape of ferroelectrics. However, hysteresis loops of positions 3, 4, 5 close to the ZnO grain deviates from the typical shape, indicating modified ferroelectricity. It may originate from the ferroelectric transition due to the strain effects with the ZnO inclusion. These site-specific results provide a direct study of the ferroelectricity with high spatial resolution, clearly demonstrating the effects of the ZnO on the ferroelectric behavior of the NBT-6BT matrix. No hysteresis loop can be obtained on the position 2 because ZnO is intrinsically not a ferroelectric.

3.3.3 Conclusion

The upper application temperature of $0.94Na_{1/2}Bi_{1/2}TiO_3$-$0.06BaTiO_3$:$x$ZnO relaxor ferroelectric/semiconductor composites was quantified using dielectric, ferroelectric, and piezoelectric measurements. Room temperature PFM data directly present the ferroelectric domain structure of studied samples, demonstrating a long-range ferroelectric order induced by the ZnO inclusion in NBT-6BT:0.1ZnO composites. After poling, PFM studies of domain evolution as a function of time evidenced the enhanced stability of domain structure in NBT-6BT:0.1ZnO composites, which may result from depolarization fields' compensation the free charge carriers from ZnO and residual thermal stresses in the composites. Compared to pure NBT-6BT ceramics, site-specific PFM investigations of the hysteresis loops reveal a more inhomogeneous ferroelectric behavior in the NBT-6BT matrix, stemming from the ZnO inclusion.

Contributions to this work:

Xijie Jiang (TUDa) carried out the PFM specimen preparation, PFM characterization, and related data processing. Chen Shen (TUDa), Na Liu (TUDa), and Christian Dietz (TUDa) offered help in PFM characterization. Lukas M. Riemers (TUDa) synthesized the lead-free $Na_{1/2}Bi_{1/2}TiO_3$-$6BaTiO_3$ with ZnO (NBT-6BT:xZnO) relaxor ferroelectric composites. Dr. Lalitha K Venkataraman provided the macroscopical information of the sample. Jurij Koruza (TUDa), Christian Dietz (TUDa), and Robert W. Stark (TUDa) supervised and oversaw this work. All authors discussed the results and contributed to this work.

3.4 Microscopic study of the high temperature creep behavior in polycrystalline $BaTiO_3$ *

Creep generally describes the tendency of a solid material to move slowly or deform permanently under the influence of persistent mechanical stresses that are still below the yield strength of the material. The creep behaviors depend on the material's intrinsic properties, exposure time, exposure temperature, and the applied structural load. Creep mechanisms are multiple and complicated. However, one mechanism is usually dominant at certain temperatures and stress. For example, diffusion creep tends to be dominant at high temperatures and low stress, while dislocation creep tends to be dominant at high temperatures and high stress.[268] The creep behavior is closely linked to the structural and functional properties of materials, making it a playground for engineering the properties of functional ceramics.

Dislocations in oxides ceramics can be treated as charged line defects and means for one-dimensional doping, which can tune electrical and thermal properties. [269] Dislocation has been demonstrated to be useful to change conductivity in plastically deformed TiO_2 and strontium titanate $SrTiO_3$ (STO) single crystals. [270, 271] Furthermore, it can also pin the flux lines in superconductors and to reducing the thermal conductivity of materials. [272, 273] Theoretical work has suggested that dislocations can pin domain walls in ferroelectrics and influence dielectric losses for high power applications. [274] Therefore, applying the dislocation creep mechanism to purposely form dislocation in the ferroelectric ceramics at high temperatures and high pressure is an interesting way to tailor the properties. [275] Furthermore, unlike some methods like nanoindentation, which only creates dislocation in a small local area, creep-induced dislocation could emege in a larege scale, revealing its promising applications.

As a well-known ferroelectric material, $BaTiO_3$ has been chosen as a model material in this study. The basic properties and structure-property relationship are well-established. The creep-mediated functionality of BT closely hinges on the structural variation after creep, particularly the domain structure, which reflects the polarization states of ferroelectrics. Therefore, to deliminate the surface morphology and corresponding domain structure of BT ceramics under different creep conditions is required to understand their behaviors.

3.4.1 Experimental

$BaTiO_3$ powders were synthesized via conventional solid-state reaction using TiO_2 (purity ≥99.6%, Sigma-Aldrich, St Louis, USA) and $BaCO_3$ (purity ≥99.8%, Sigma-Aldrich, St Louis, USA) as raw materials. The powders were mixed according to the stoichiometric formula and ball-milled for 12 hours with zirconia balls and ethanol in a planetary ball mill (Fritsch Pulverisette 5, Idar-Oberstein,

*Part of this chapter has been published in Ref. [276].

Germany). These powders were re-milled for 24 hours after drying and calcination at 1100°C for 6 hours. A die with an inner diameter of 6.5 mm was employed to press samples of cylindrical shape, which were further compacted under 200 MPa using a cold isostatic press (KIP 100E, Weber, Remshalden, Germany). Specimens were sintered at 1350°C for 6 hours, yielding cylinders with a diameter of about 4.8 mm and a height of 16.5 mm. Next, this cylinder was cut into small cylinders. Finally, cylinders with dimensions of 4 mm ± 0.05 mm in diameter and 8 mm ± 0.02 mm in height were used for the creep experiments. The smaller reference cylinder was cut into pellets (labeled as undeformed BT). The schematic diagram in Fig. 3.21 illustrates the sample preparation process.

For studying the creep behaviors, the cylinders were then deformed at fixed temperatures, compressive stress, and time respectively to yield either diffusion creep or dislocation creep. In this study, high temperature creeps investigations were focused on 3 samples prepared in different conditions: undeformed BT, BT that deformed at 1000°C and 200 MPa for 15 minutes (labeled as C-1000 °C-15 min), and BT deformed at 1050 °C and 200 MPa for 30 minutes (labeled C-1050 °C-30 min). The microstructure was quantified from polished cross-sections after thermal etching at 1250°C for 10 minutes using scanning electron microscopy (SEM) (XL30FEG, Philips, Amsterdam, Netherlands). The domain structure of polished surfaces was obtained with a piezoresponse force microscope (PFM) (MPF-3D, Asylum Research, Santa Barbara, CA, USA).

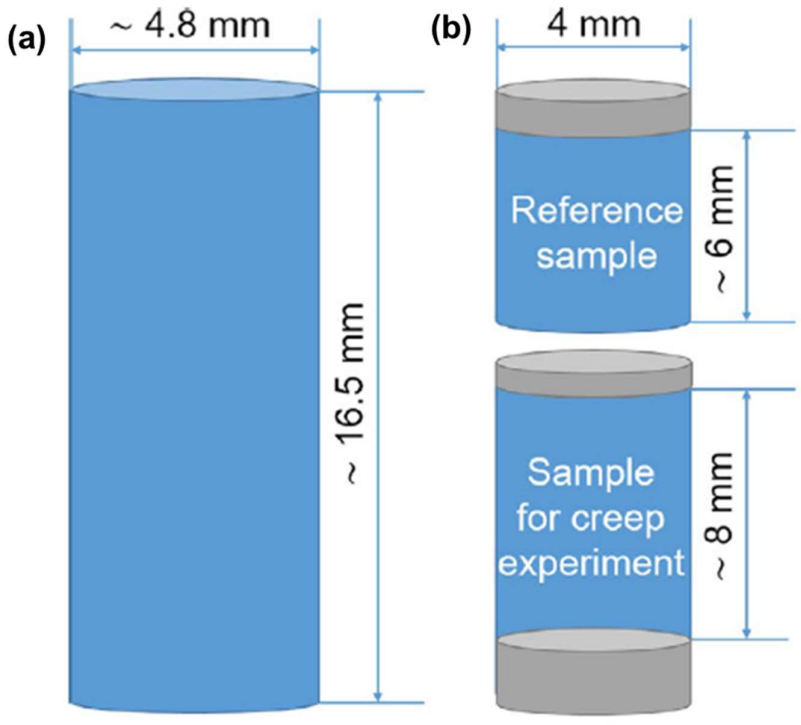

Figure 3.21 Schematic diagram of samples used in this study. The sintered cylinder (a) was cut into two smaller parts (b), whereby one was deformed, and the other served as a reference (the edges marked with gray were discarded).

3.4.2 Results and Discussions

The creep deformation analysis indicates that the C-1000 °C-15 min sample is in a diffusion creep regime and the C-1050 °C-30 min sample is in dislocation creep regime. The microstructure and domain structure for the undeformed BT, C-1000°C-15 min and C-1050°C-30 min samples were investigated by SEM and PFM, respectively, for revealing the adjustment of materials upon different creep mechanisms.

Figure 3.22 displays the SEM images for the undeformed BT, C-1000°C-15 min, and C-1050°C-30 min samples. It shows a good sintering quality for the ceramics. The grain size remains almost unchanged for different samples. Twins can be observed for all samples. However, no noticeable changes of the structure can be observed between different samples. The structure evolution resulting from creep, like dislocation and cavitations, usually occurs at the nanoscale to the atomic scale. Thus SEM technique is challenging to resolve.

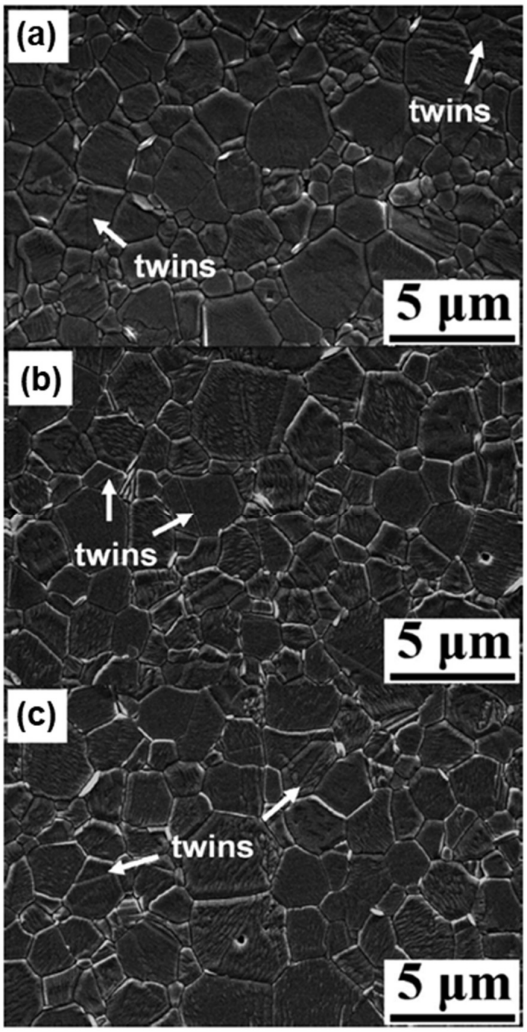

Figure 3.22 SEM images of (a) undeformed BT, (b) C-1000°C-15 min, and (c) C-1050°C-30 min

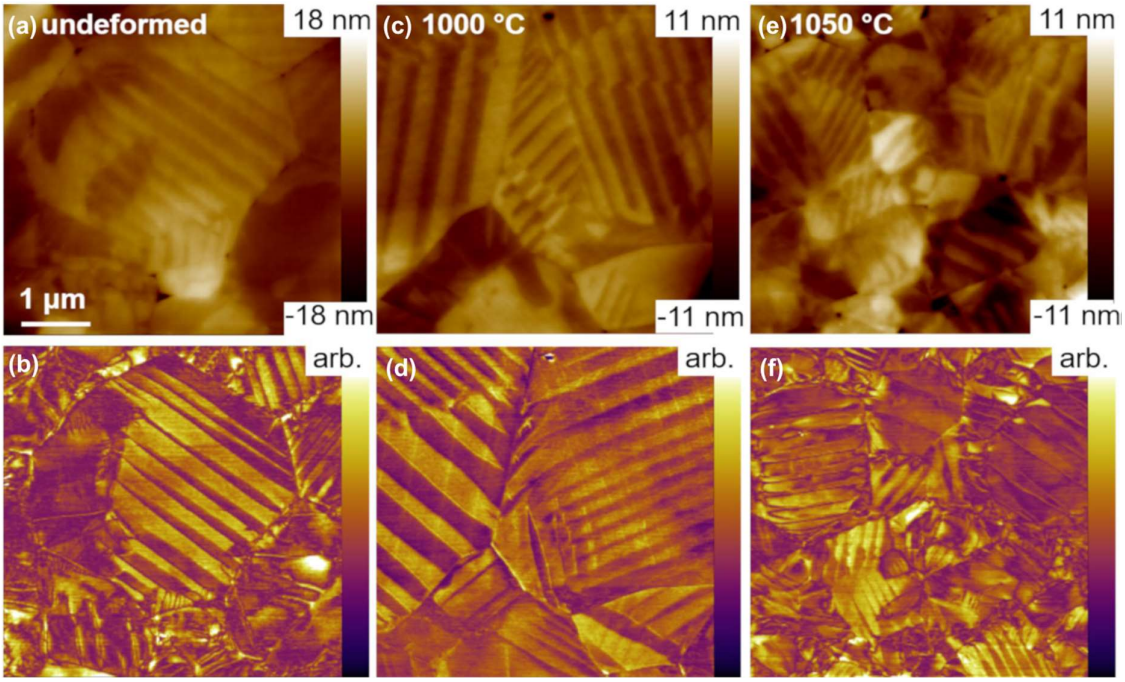

Figure 3.23 Piezoresponse force microscope images of the topography (a, c, e) and the lateral amplitude (b, d, f) for an undeformed sample (a, b), C-1000°C-15 min sample (c, d), and C-1050°C-30 min sample (e, f). The scales for the lateral amplitude and the height difference of the topography are on the right, respectively

The domain structure was investigated with piezoresponse force microscopy. The PFM images in Fig. 3.23 display the topography and the lateral amplitude for the undeformed sample (a, b), C-1000°C-15 min (c, d), and C-1050°C-30 min (e, f). The topography images show the smooth surface of 3 samples after polishing. Similar to SEM results, no obvious variation of the surface morphology between 3 samples can be observed. The grain boundaries can be obviously visualized. The imaged region for C-1050°C-30 min has a higher density of grain boundaries than undeformed BT and C-1000°C-15 min samples. Therefore, a higher density of domains walls can be identified in the corresponding domain maps in Fig 3.23(f). The domain walls are mostly 90° and 180° because all studied samples are in the tetragonal phase. The domain size is in the range of 115-154 nm, which agrees with the reports by Hoshina et al. [277] (100 nm for a grain size of 1.1 µm) and Cao and Randall [278] (150 nm-300 nm for grain sizes of 2 µm-4 µm). The presented PFM results show no significant changes in the domain structure between the samples. For uncovering the dislocation or diffusion creep mechanism, PFM imaging with improved spatial resolution or other high-resolution techniques like TEM should be employed to carry out a more detailed analysis of microstructure at the grain boundaries and the local domain structure in the vicinity of the dislocations.

3.4.3 Conclusion

PFM experiments have been carried out to study the surface morphology, and domain structure of polycrystalline $BaTiO_3$ deformed in different creep mechanisms. Our PFM results show that the

macroscopic structure and domain structure remain unchanged in different samples. Since the structure variations related to diffusion creep and dislocation mechanisms take place on the nanoscale to the atomic scale, microscopes with high resolution are required for these studies.

Contributions to this work:

Xijie Jiang (TUDa) carried out the PFM specimen preparation, PFM characterization and related data processing. Christian Dietz (TUDa) offered help in PFM characterization. Rongpeng Ren (TUDa) synthesized the $BaTiO_3$ ceramics. Jurij Koruza (TUDa), Christian Dietz (TUDa) and Robert W. Stark (TUDa) supervised and oversaw this work. All authors discussed the results and contributed to this work.

4. Conclusions and Outlook

This dissertation is mainly focused on visualizing the microscopic ferroelectric domain for a lead-free ferroelectric system and unveiling its correlation with functional behaviors. For this purpose, the PFM technique has been employed to study the static state and dynamic evolution of ferroelectric domains in lead-free piezoceramics. The studied materials are mainly lead-free (1-x)$Ba(Zr_{0.2}Ti_{0.8})O_3$-$x(Ba_{0.7}Ca_{0.3})TiO_3$ (BZT-xBCT) piezoelectric ceramic and $0.94Na_{1/2}Bi_{1/2}TiO_3$-$0.06BaTiO_3$:$x$ZnO relaxor ferroelectric/semiconductor composites.

For the BZT-0.5BCT piezoceramic, PFM experiments revealed the virgin domain structure of a BZT-0.5BCT piezoceramic consisted of lamellar and wedge-shaped domains at RT. Under temperature and electric field stimulations, the wedge-shaped domain was found to play a crucial role in the domain structure evolution of BZT-0.5BCT ceramics because of the swift response of its size and the domain wall motion. Furthermore, a transitional domain structure with a high density of domain walls emerges in both the temperature and electric field cases. Temperature-dependent domain evolution evidenced a phase transition to a tetragonal structure at a temperature between 40 °C and 45 °C in our experiment. A premature phase transition to the tetragonal phase under poling conditions was also revealed. Field-dependent domain studies at different temperatures for the BZT-0.5BCT piezoceramic directly revealed that the structure was mainly an extrinsic response at temperatures close to the line of equilibrium in the phase diagram and intrinsic at higher temperatures far from the phase boundary. Most interestingly, our electric-field-dependent PFM results show almost complete reversibility of the domain structure with an unaltered number and shape of domains at medium temperatures (40 °C – 60 °C), implying a slow rate of fatigue for the functional properties of the BZT-0.5BCT ceramics in this temperature range. Due to the limit of our experimental set-up, the highest reachable temperature is about 60 °C. For future work, it would be exciting to study the domain structure and field-dependent domain evolution at the higher temperature, especially close to the Curie temperature, to study the ferroelectric to the paraelectric phase transition.

PFM studies were also performed to explore the fundamental mechanism of the unipolar fatigue behavior of three BZT-xBCT compositions with different crystallographic structures, *i.e.*, 40BCT(R), 50BCT(O), and 60BCT(T). PFM domain maps indicate that the high amount of extrinsic contributions to strain made orthorhombic 50BCT(O) and rhombohedral 40BCT(R) compositions most susceptible to fatigue during unipolar cycling. 50BCT(O) shows a domain fragmentation with increased domain wall intensity upon cycling. The fatigue response of 40BCT(R) was additionally affected by the formation of a single domain state, which increased the fraction of irreversible contributions and partially compensated the reduction of the electromechanical properties. Domains maps show that the tetragonal composition 60BCT(T) has high intrinsic contributions to strain, making it more resistant to electric fatigue, resulting in relatively stable electromechanical properties.

For the $0.94Na_{1/2}Bi_{1/2}TiO_3$-$0.06BaTiO_3$:$x$ZnO relaxor composite, effects of the ZnO inclusion on the domain structure were characterized by PFM, demonstrating a long-range ferroelectric order induced by the ZnO inclusion in NBT-6BT:0.1ZnO composites. After poling, PFM studies of domain evolution as a function of time evidenced the enhanced stability of domain structure in NBT-6BT:0.1ZnO composites compared to pure NBT-6BT ceramics, which may result from the compensation of depolarization fields by the free charge carriers from ZnO and residual thermal stress in the composites. In contrast to pure NBT-6BT ceramics, site-specific PFM investigations of the hysteresis loops reveal a more inhomogeneous ferroelectric behavior in the NBT-6BT matrix, stemming from the ZnO inclusion. For future work, a temperature-dependent PFM study would be significant to reveal the depolarization mechanism with the inclusion of ZnO. Furthermore, in order to get further insights into the effects of the ZnO inclusion, in-depth studies on the boundary region between ZnO and matrix are demanding. Other microscope techniques, such as conductive AFM and TEM, can be adopted to study the charge distribution and strain field.

PFM experiments were carried out to study the surface morphology, and domain structure of polycrystalline $BaTiO_3$ deformed in different creep mechanisms. PFM results show that the macroscopic structure and domain structure remain unchanged in different samples. Since the structure variations related to diffusion creep and dislocation mechanisms take place on the nanoscale to the atomic scale, microscopes with high resolution are required for these studies. With the PFM technique, it would be interesting to use the DART mode to get more accurate images to see if more details can be measured.

For the future, the domain dynamics and domain wall evolution can be calculated in a more quantitative method, such as the simulation. To find the nanodomains inside the more considerable domain structure might be more important to help to understand the underneath mechanism of the ferroelectric properties. The small size of the remaining domains was not resolvable in the phase channel using single-frequency PFM. However, the dissociated nanometer-sized domains increased the density of domain walls per unit area, leading to observable dark areas in the amplitude images. To observe the real-time domain evolution, the single frequency high-speed imaging PFM should be used. High-speed PFM is straightforward to realize the fast imaging but is not capable to directly resolve nanodomains.

In this thesis, AFM-related techniques, particularly PFM, have been used for microscopic investigations of lead-free piezoceramics, emphasizing their microscopic domain structures. This thesis provides a comprehensive understanding of the microstructural origin of piezoceramics' ferroelectric behaviors, which is instructive for their practical applications.

Appendix

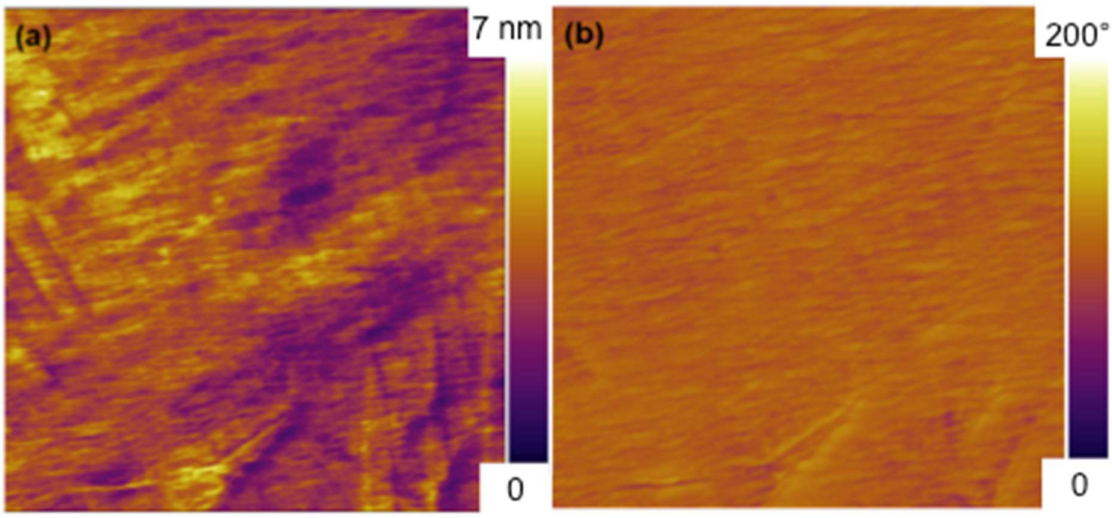

Figure A.1 (a) The vertical PFM amplitude and (b) the vertical PFM phase image for the BZT-0.5BCT ceramic in its virgin state.

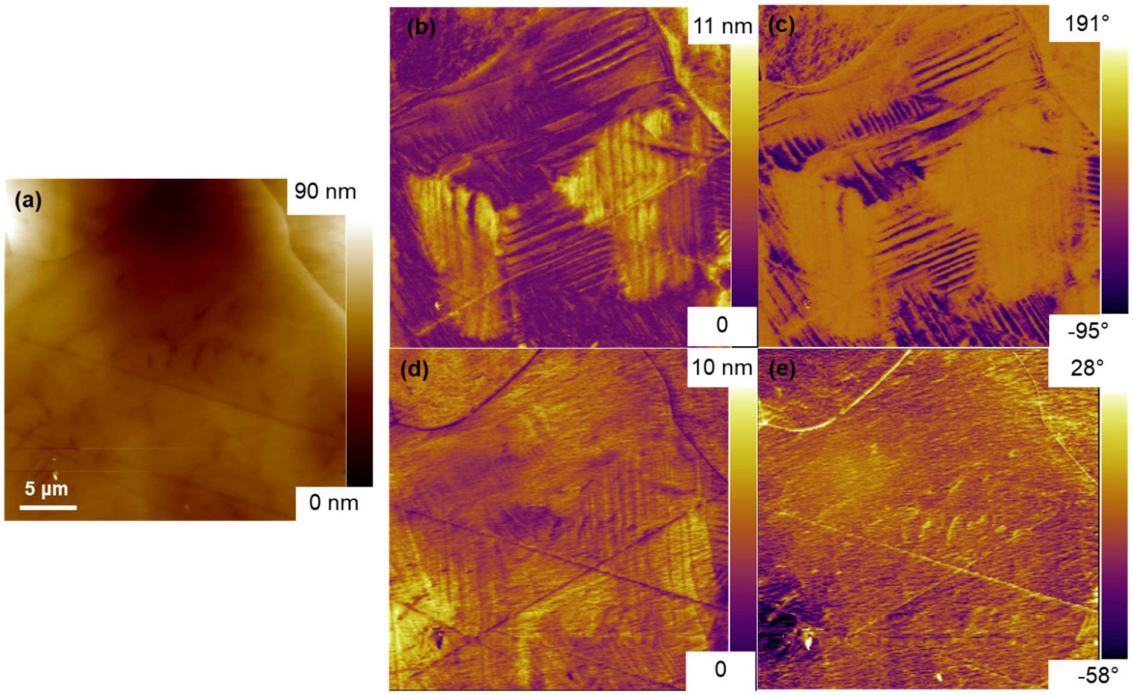

Figure A.2 (a) The topography, (b) lateral PFM amplitude, (c) lateral PFM phase image, (d) vertical PFM amplitude, and (e) vertical PFM phase image for a large region of the BZT-0.5BCT ceramic in its virgin state.

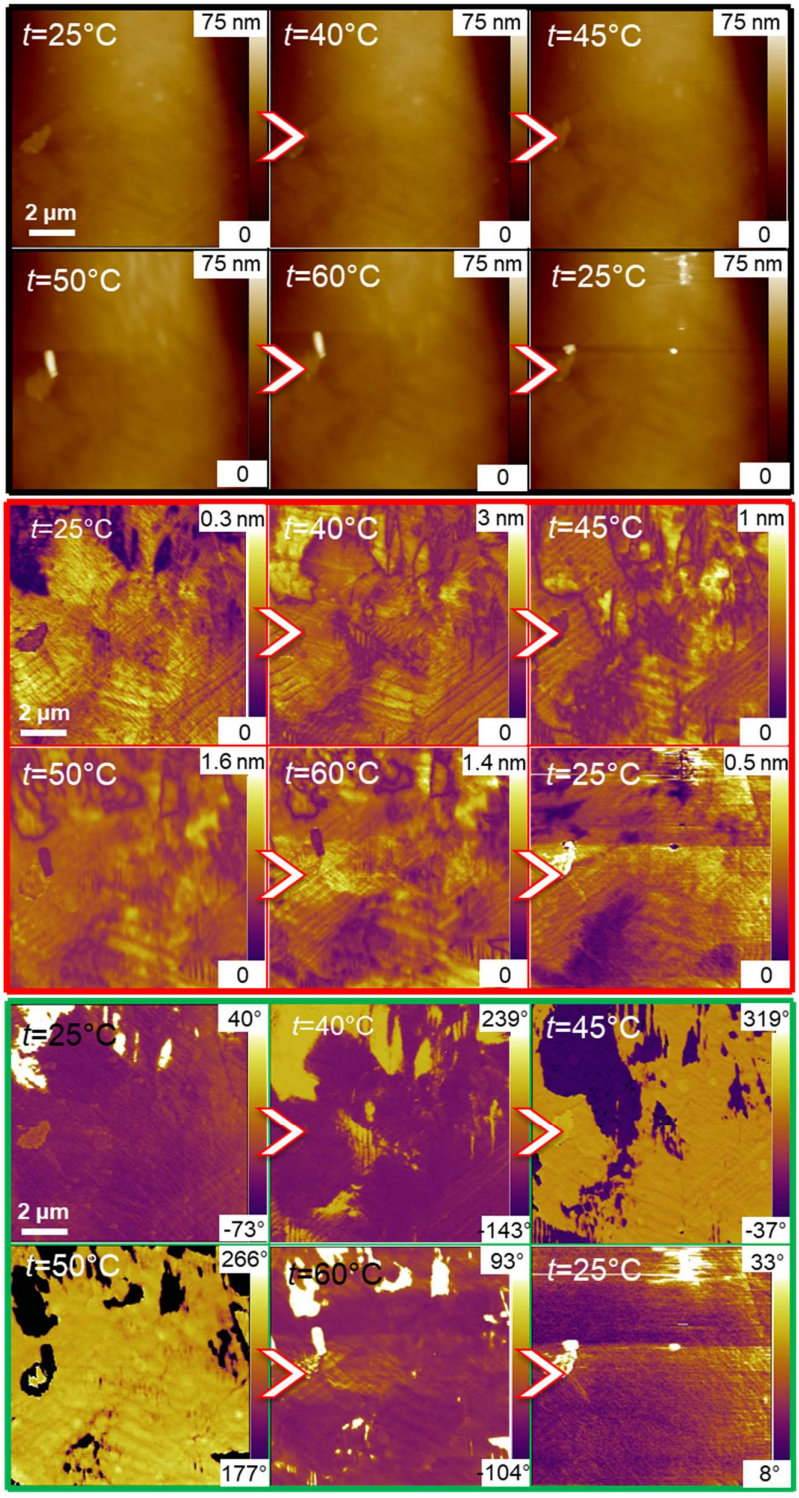

Figure A.3 The surface topography (black box), vertical PFM amplitude (red box), and phase (green box) for the BZT-0.5BCT ceramic during heating up to 60 °C and subsequent cooling down to RT (t = 25 °C).

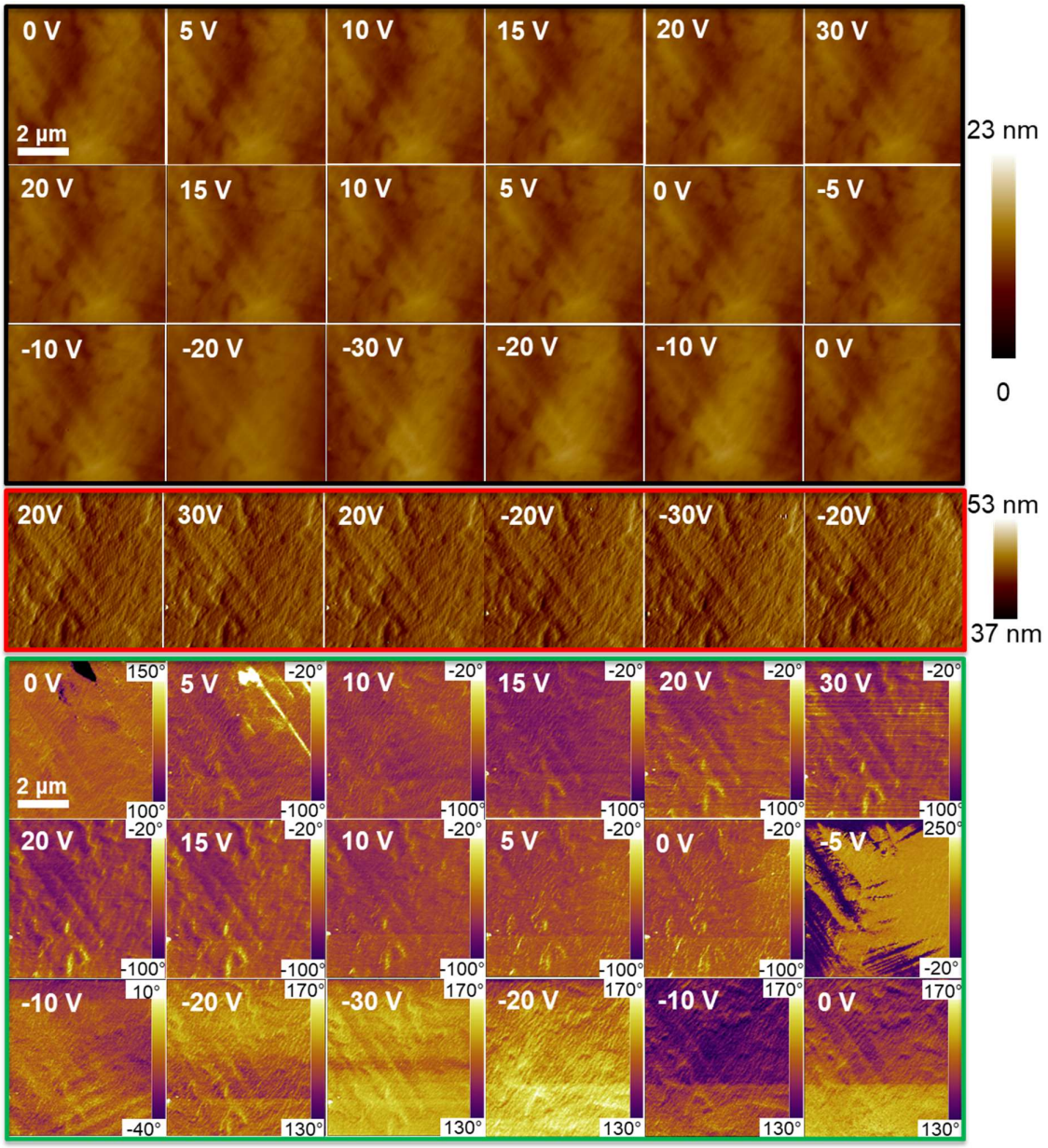

Figure A.4 The surface topography (black box) and PFM vertical phase map (green box) of the BZT-0.5BCT ceramic under applied voltages (0 V→ 30 V→ 0 V→ -30 V→ 0 V). The deflection maps (red box) at high voltages show that a constant force was applied to the surface and that the feedback worked properly, demonstrating that they remained on the surface during the high-voltage polling process.

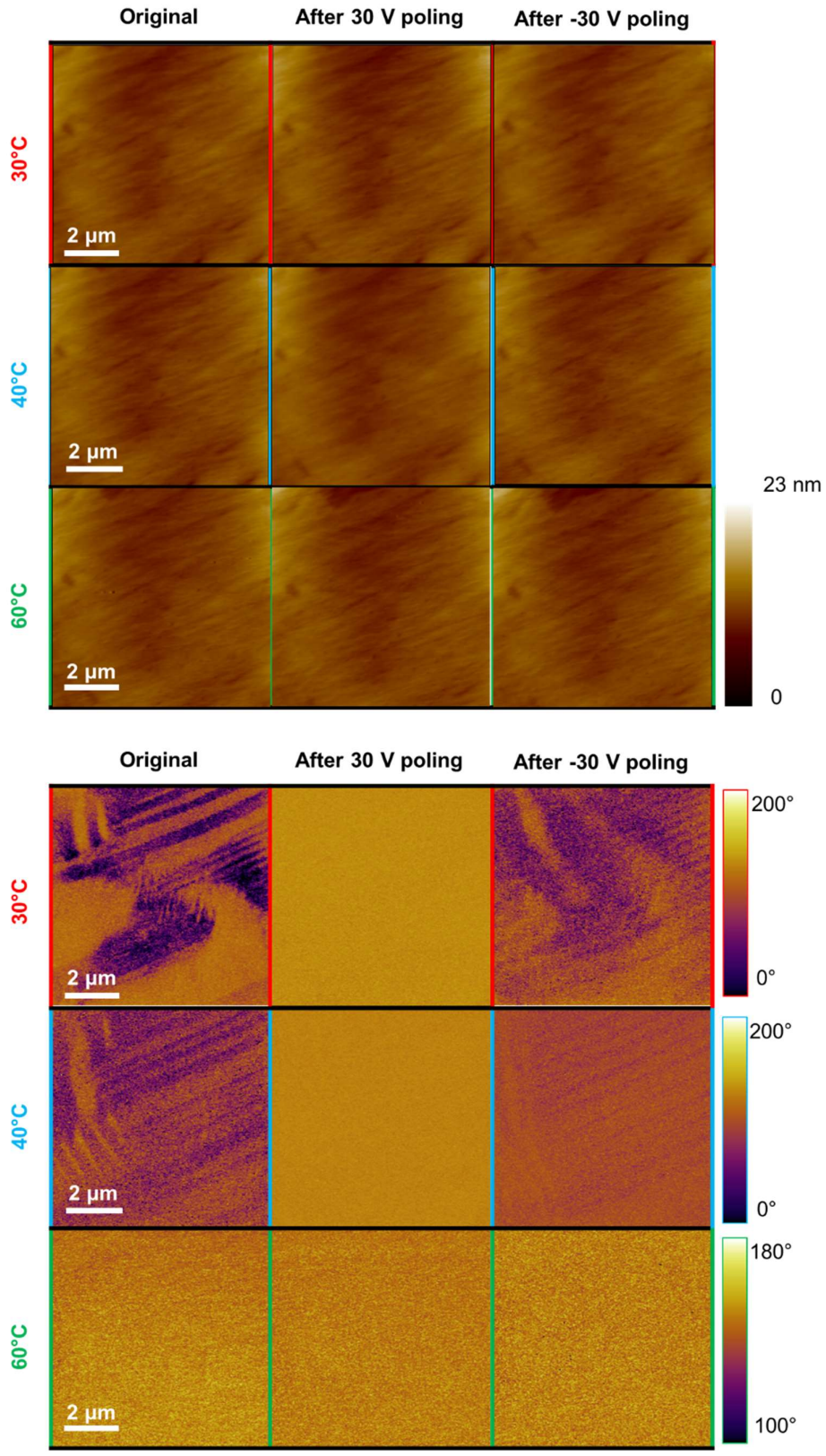

Figure A.5 The surface topography (the upper panel) and PFM vertical phase map (the bottom panel) for the BZT-0.5BCT ceramic under temperature and applied voltage stimulation.

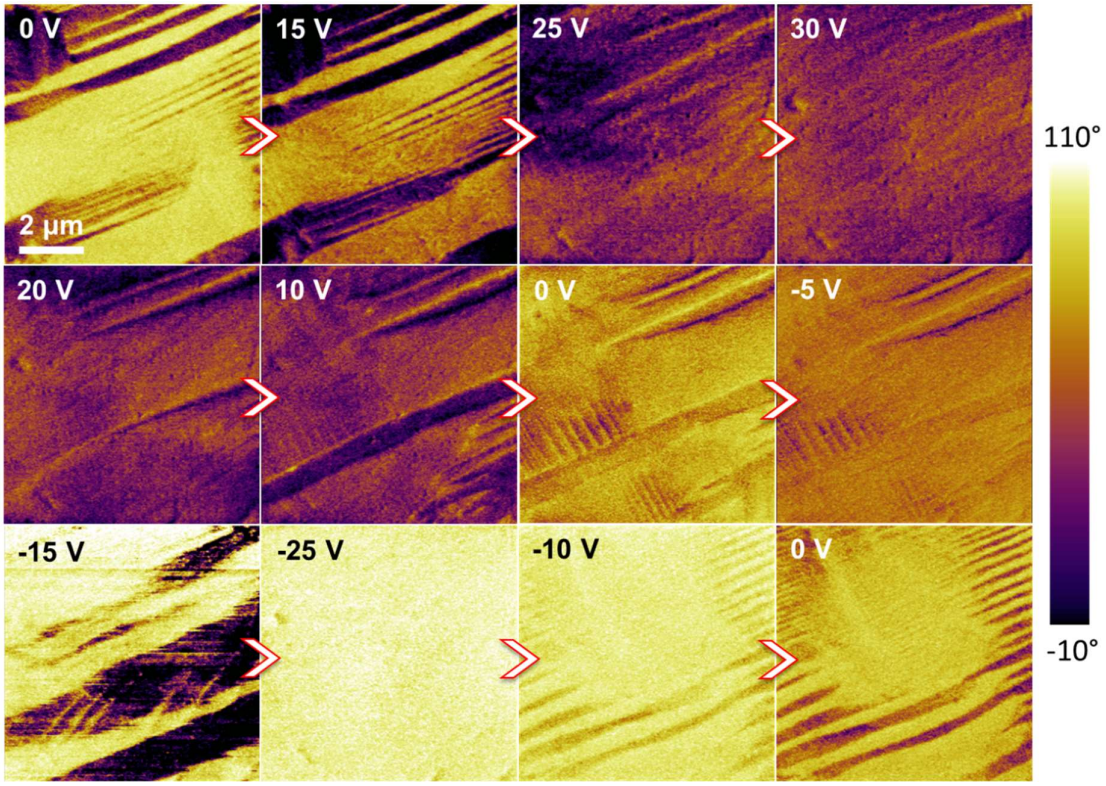

Figure A.6 The domain evolution of the BZT-0.5BCT ceramic under the stimulation of external electrical fields generated by the PFM tip at room temperature (T = 30 °C).

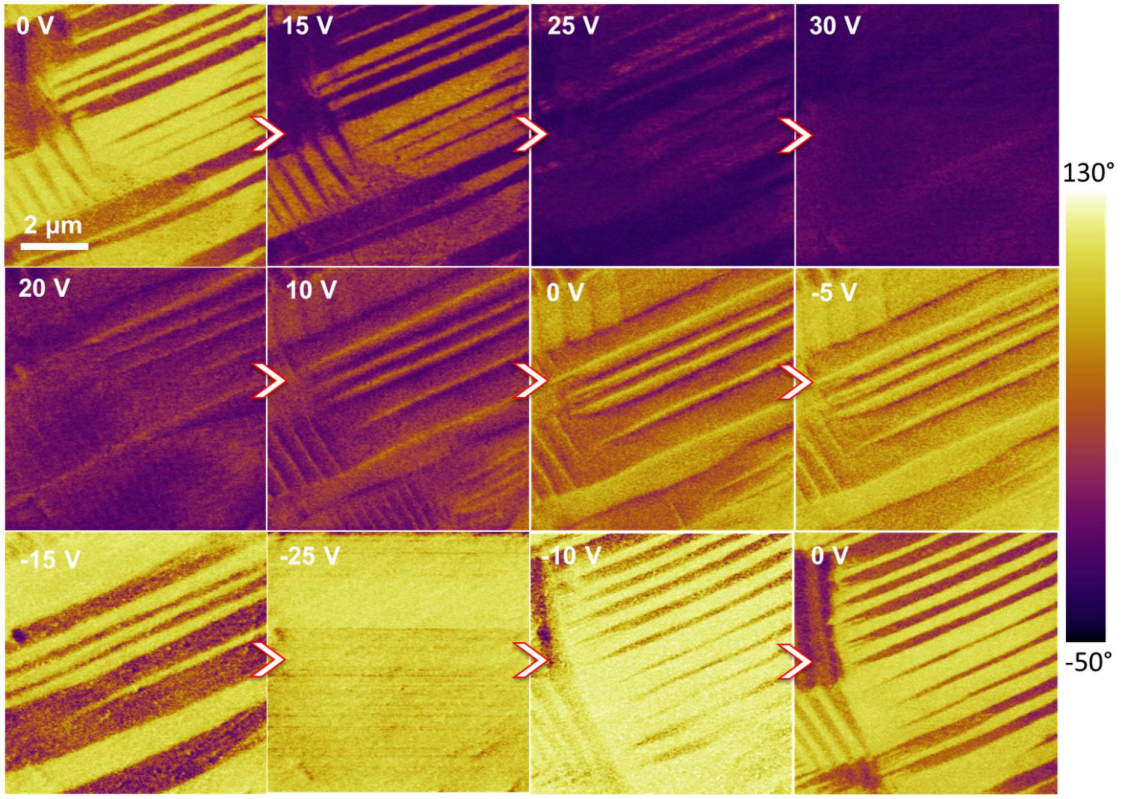

Figure A.7 The domain evolution of the BZT-0.5BCT ceramic under the stimulation of external electrical fields generated by the PFM tip at room temperature (T = 40 °C).

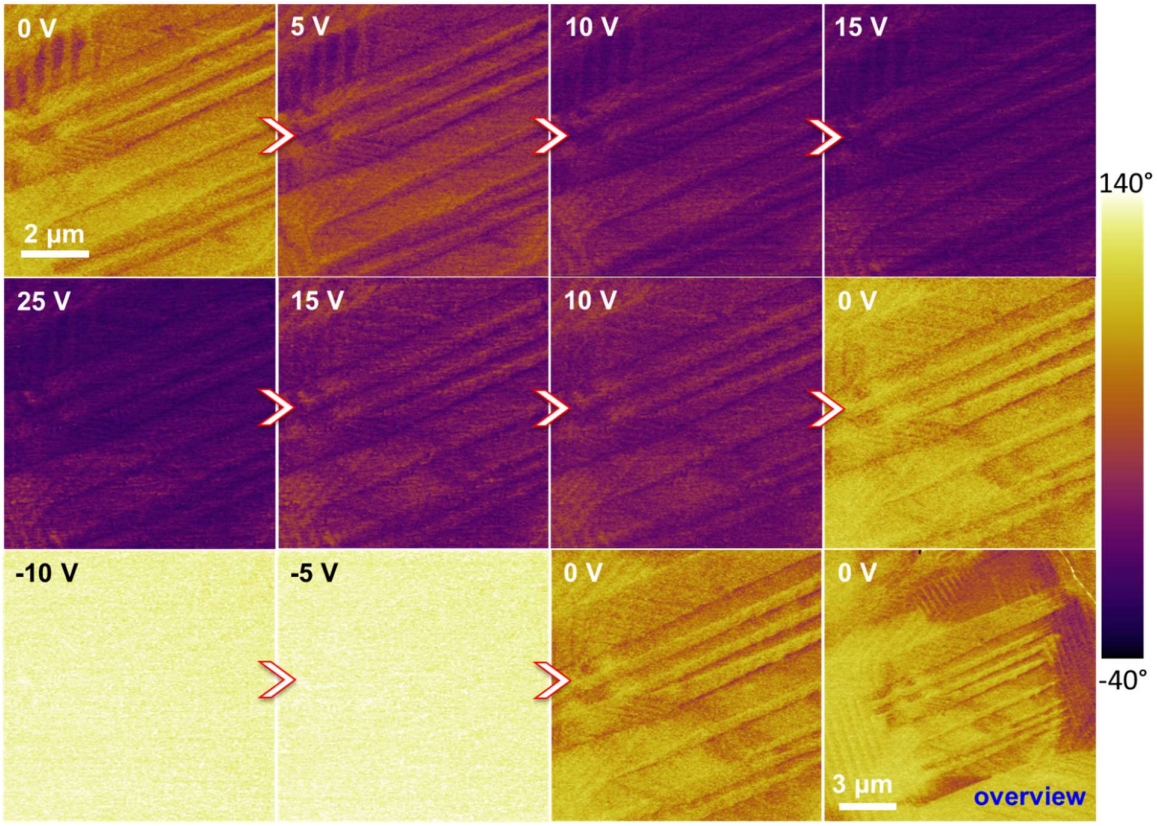

Figure A.8 The domain evolution of the BZT-0.5BCT ceramic under the stimulation of external electrical fields generated by the PFM tip at room temperature (T = 60 °C).

References

1. Uchino, K., *Piezoelectric actuators and ultrasonic motors*. Electronic Materials: Science & Technology. 1997, Boston: Kluwer Academic Publishers. 350.
2. Newnham, R.E., *Functional composites for sensors and actuators: smart materials.* 1998, Pennsylvania, USA: The Pennsylvania Academy of Science.
3. Uchino, K., *Ceramic actuators - Principles and applications.* MRS Bulletin, 1993. **18**(4): p. 42-48.
4. Sahoo, B., V.A. Jaleel, and P.K. Panda, *Development of PZT powders by wet chemical method and fabrication of multilayered stacks/actuators.* Materials Science and Engineering B-Solid State Materials for Advanced Technology, 2006. **126**(1): p. 80-85.
5. Newnham, R.E., et al., *Functional composites for sensors and actuators: smart materials.* The Pennsylvania Academy of Science, PA, USA, 1998.
6. Jaffe, B., *W. R. Cook and H.* Jaffe, Piezoelectric Ceramics, Academic Press, London, 1971.
7. Jaffe, B., *Piezoelectric ceramics*. Vol. 3. 2012: Elsevier.
8. Jo, W., et al., *Giant electric-field-induced strains in lead-free ceramics for actuator applications - status and perspective.* Journal of Electroceramics, 2012. **29**(1): p. 71-93.
9. *"Eu-Directive 2002/95/Ec: Restriction of the Use of Certain Hazardous Sbustances in Electrical and Electronic Equipment (RoHS),"* O.J.E. Union, Editor. 2003. p. 19.
10. *"Eu-directive 2011/65/Eu: Restriction of the use of certain hazardous substances in electrical and electronic equipment (RoHS),"* O.J.E. Union, Editor. 2011. p. 88.
11. Prytz, O., et al., *Charge-ordered spinel AlV2O4: High-energy-resolution EELS and computational studies.* Physical Review B, 2012. **85**(19).
12. Rodel, J., et al., *Perspective on the Development of Lead-free Piezoceramics.* Journal of the American Ceramic Society, 2009. **92**(6): p. 1153-1177.
13. Saito, Y., et al., *Lead-free piezoceramics.* Nature, 2004. **432**(7013): p. 84.
14. Shrout, T.R. and S.J. Zhang, *Lead-free piezoelectric ceramics: alternatives for PZT?* Journal of Electroceramics, 2007. **19**(1): p. 113.
15. Hong, C.-H., et al., *Lead-free piezoceramics–Where to move on?* Journal of Materiomics, 2016. **2**(1): p. 1-24.
16. Malič, B., et al., *Sintering of lead-free piezoelectric sodium potassium niobate ceramics.* Materials, 2015. **8**(12): p. 8117-8146.

17. Li, J.F., et al., *(K,Na)NbO_3-Based Lead-Free Piezoceramics: Fundamental Aspects, Processing Technologies, and Remaining Challenges.* Journal of the American Ceramic Society, 2013. **96**(12): p. 3677-3696.

18. Saito, Y., et al., *Lead-free piezoceramics.* Nature, 2004. **432**(7013): p. 84-87.

19. Takenaka, T., K.-i. Maruyama, and K. Sakata, *($Bi_{1/2}Na_{1/2}$)TiO_3-$BaTiO_3$ system for lead-free piezoelectric ceramics.* Japanese journal of applied physics, 1991. **30**(9S): p. 2236.

20. Zhang, S.-T., et al., *Temperature-Dependent Electrical Properties of 0.94$Bi_{0.5}Na_{0.5}TiO_3$–0.06$BaTiO_3$ Ceramics.* Journal of the American Ceramic Society, 2008. **91**(12): p. 3950-3954.

21. Rout, D., et al., *Study of the morphotropic phase boundary in the lead-free $Na_{1/2}Bi_{1/2}TiO_3$-$BaTiO_3$ system by Raman spectroscopy.* Journal of the Ceramic Society of Japan, 2009. **117**(1367): p. 797-800.

22. Yao, J., et al., *Evolution of domain structures in $Na_{1/2}Bi_{1/2}TiO_3$ single crystals with $BaTiO_3$.* Physical Review B, 2011. **83**(5).

23. Jo, W., et al., *Giant electric-field-induced strains in lead-free ceramics for actuator applications–status and perspective.* Journal of Electroceramics, 2012. **29**(1): p. 71-93.

24. Liu, W. and X. Ren, *Large piezoelectric effect in Pb-free ceramics.* Physical review letters, 2009. **103**(25): p. 257602.

25. Wang, D., et al., *Phase Diagram and Enhanced Piezoelectric Response of Lead-Free $BaTiO_3$–$CaTiO_3$–$BaHfO_3$ System.* Journal of the American Ceramic Society, 2014. **97**(10): p. 3244-3251.

26. Takenaka, T., et al., *Lead-free piezoelectric ceramics based on perovskite structures.* Journal of Electroceramics, 2007. **19**(4): p. 259-265.

27. Damjanovic, D., et al., *What can be expected from lead-free piezoelectric materials?* Functional Materials Letters, 2010. **3**(01): p. 5-13.

28. Moulson, A.J. and J.M. Herbert, *Electroceramics: materials, properties, applications*. 2003: John Wiley & Sons.

29. Haertling, G.H., *Ferroelectric ceramics: history and technology.* Journal of the American Ceramic Society, 1999. **82**(4): p. 797-818.

30. Bokov, A. and Z.-G. Ye, *Recent progress in relaxor ferroelectrics with perovskite structure.* Journal of materials science, 2006. **41**(1): p. 31-52.

31. Cross, L.E., *Relaxor ferroelectrics.* Ferroelectrics, 1987. **76**(1): p. 241-267.

32. Zhao, X., et al., *Electric field-induced phase transitions in (111)-,(110)-, and (100)-oriented $Pb(Mg_{1/3}Nb_{2/3})O_3$ single crystals.* Physical Review B, 2007. **75**(10): p. 104106.

33. Wang, Y., et al., *Giant domain wall contribution to the dielectric susceptibility in $BaTiO_3$ single crystals.* Applied Physics Letters, 2007. **91**(6): p. 062905.

34. Seshadri, S.B., et al., *An in situ diffraction study of domain wall motion contributions to the frequency dispersion of the piezoelectric coefficient in lead zirconate titanate.* Applied Physics Letters, 2013. **102**(4): p. 042911.

35. Damjanovic, D., P. Muralt, and N. Setter, *Ferroelectric sensors.* IEEE sensors journal, 2001. **1**(3): p. 191-206.

36. Jo, W., et al., *On the phase identity and its thermal evolution of lead free $(Bi_{1/2}Na_{1/2})TiO_3$-6 mol% $BaTiO_3$.* Journal of Applied Physics, 2011. **110**(7): p. 074106.

37. Ehmke, M.C., et al., *In Situ X-ray Diffraction of Biased Ferroelastic Switching in Tetragonal Lead-free (1-x)$Ba(Zr_{0.2}Ti_{0.8})O_3$-x$(Ba_{0.7}Ca_{0.3})TiO_3$ Piezoelectrics.* Journal of the American Ceramic Society, 2013. **96**(9): p. 2913-2920.

38. Hirota, K., S. Wakimoto, and D.E. Cox, *Neutron and x-ray scattering studies of relaxors.* Journal of the Physical Society of Japan, 2006. **75**(11): p. 111006-111006.

39. Xu, G., et al., *Neutron elastic diffuse scattering study of $Pb(Mg_{1/3}Nb_{2/3})O_3$.* Physical Review B, 2004. **69**(6): p. 064112.

40. Viehland, D., et al., *Freezing of the polarization fluctuations in lead magnesium niobate relaxors.* Journal of Applied Physics, 1990. **68**(6): p. 2916-2921.

41. Bokov, A. and Z.-G. Ye, *Recent progress in relaxor ferroelectrics with perovskite structure.* Progress in Advanced Dielectrics, 2020: p. 105-164.

42. Guo, H., et al., *Polarization alignment, phase transition, and piezoelectricity development in polycrystalline 0.5$Ba(Zr_{0.2}Ti_{0.8})O_3$-0.5$(Ba_{0.7}Ca_{0.3})TiO_3$.* Physical Review B, 2014. **90**(1).

43. Vilarinho, P.M., Y. Rosenwaks, and A. Kingon, *Scanning probe microscopy-characterization, nanofabrication and device application of functional materials*. 2004, The Netherlands: Kluwer Academic Pbulishers.

44. Auciello, O., et al., *Nanoscale scanning force imaging of polarization phenomena in ferroelectric thin films.* Mrs Bulletin, 1998. **23**(1): p. 33-42.

45. Alexe, M. and A. Gruverman, *Nanoscale characterization of ferroelectric: Scanning probe microscopy approach*. 2004, Berlin: Springer.

46. Franke, K., et al., *Modification and detection of domains on ferroelectric PZT films by scanning force microscopy.* Surface Science, 1994. **302**(1-2): p. L283-L288.

47. Gruverman, A., O. Auciello, and H. Tokumoto, *Scanning force microscopy for the study of domain structure in ferroelectric thin films.* Journal of Vacuum Science & Technology B, 1996. **14**(2): p. 602-605.

48. Gruverman, A., O. Auciello, and H. Tokumoto, *Nanoscale investigation of fatigue effects in $Pb(Zr,Ti)O_3$ films.* Applied Physics Letters, 1996. **69**(21): p. 3191-3193.

49. Eng, L.M., et al., *Nanoscale reconstruction of surface crystallography from three-dimensional polarization distribution in ferroelectric barium-titanate ceramics.* Applied Physics Letters, 1999. **74**(2): p. 233-235.

50. Eng, L.M., et al., *Nondestructive imaging and characterization of ferroelectric domains in periodically poled crystals.* Journal of Applied Physics, 1998. **83**(11): p. 5973-5977.

51. Abplanalp, M., L.M. Eng, and P. Gunter, *Mapping the domain distribution at ferroelectric surfaces by scanning force microscopy.* Applied Physics a-Materials Science & Processing, 1998. **66**: p. S231-S234.

52. Kholkin, A., et al., *Surface domain structures and mesoscopic phase transition in relaxor ferroelectrics.* Advanced Functional Materials, 2011. **21**(11): p. 1977.

53. Lehnen, P., et al., *Ferroelectric nanodomains in the uniaxial relaxor system $Sr_{0.61-x}Ba_{0.39}Nb_2O_6 : Ce_x^{3+}$.* Physical Review B, 2001. **64**(22): p. 224109.

54. Balke, N., et al., *Electromechanical Imaging and Spectroscopy of Ferroelectric and Piezoelectric Materials: State of the Art and Prospects for the Future.* Journal of the American Ceramic Society, 2009. **92**(8): p. 1629-1647.

55. Okino, H., J. Sakamoto, and T. Yamamoto, *Contact-resonance piezoresponse force microscope and its application to domain bbservation of $Pb(Mg_{1/3}Nb_{2/3})O_3$-$PbTiO_3$ single crystals.* Japanese Journal of Applied Physics Part 1-Regular Papers Short Notes & Review Papers, 2003. **42**(9B): p. 6209.

56. Alexe, M. and A. Gruverman, *Nanoscale characterisation of ferroelectric materials: scanning probe microscopy approach*. 2004: Springer Science & Business Media.

57. Kalinin, S.V. and A. Gruverman, *Scanning probe microscopy of functional materials: nanoscale imaging and spectroscopy*. 2010: Springer Science & Business Media.

58. Voigtländer, B., *Scanning probe microscopy: Atomic force microscopy and scanning tunneling microscopy*. 2015: Springer.

59. Lines, M. and A. Glass, *Principles and Applications of Ferroelectrics and Related Materials 1977*. 1977, Oxford University Press: New York, NY.

60. Katzir, S., *The discovery of the piezoelectric effect*, in *THE BEGINNINGS OF PIEZOELECTRICITY*. 2006, Springer. p. 15-64.

61. Xu, Y., *Ferroelectric materials and their applications*. 2013: Elsevier.

62. Defaÿ, E., *Integration of ferroelectric and piezoelectric thin films: concepts and applications for microsystems*. 2013: John Wiley & Sons.

63. Bottger, U., S. Tiedke, and R. Waser, *Polar Oxides: Properties, Characterization, and Imaging*. 2005: Wiley-VCH.

64. Jacques, C. and C. Pierre, *Development, via compression, of electric polarization in hemihedral crystals with inclined faces.* Bull. Soc. Minérologique Fr, 1880. **3**: p. 90-3.

65. Rödel, J. and J.-F. Li, *Lead-free piezoceramics: Status and perspectives.* MRS Bulletin, 2018. **43**(8): p. 576-580.

66. Kaminow, I., *Principles and applications of ferroelectrics and related materials.* IEEE Journal of Quantum Electronics, 1978. **14**(6): p. 450-451.

67. Rabe, K.M., C.H. Ahn, and J.-M. Triscone, *Physics of ferroelectrics - A modern perspective*. 2007: Springer.

68. Jin, L., F. Li, and S.J. Zhang, *Decoding the fingerprint of ferroelectric loops: Comprehension of the material properties and structures.* Journal of the American Ceramic Society, 2014. **97**(1): p. 1-27.

69. Damjanovic, D., *Ferroelectric, dielectric and piezoelectric properties of ferroelectric thin films and ceramics.* Reports on Progress in Physics, 1998. **61**(9): p. 1267-1324.

70. Valasek, J., *Piezo-electric and allied phenomena in Rochelle salt.* Physical review, 1921. **17**(4): p. 475.

71. Roberts, S., *Dielectric and piezoelectric properties of barium titanate.* Physical Review, 1947. **71**(12): p. 890-895.

72. Rose, G., *De novis quibusdam fossilibus quae in montibus Uraliis inveniuntur*. 1839: Schade.

73. Goldschmidt, V., *Crystal structure and chemical constitution.* Transactions of the Faraday Society, 1929. **25**: p. 253-283.

74. Kubacka, A., M. Fernandez-Garcia, and G. Colon, *Advanced nanoarchitectures for solar photocatalytic applications.* Chemical reviews, 2012. **112**(3): p. 1555-1614.

75. Acosta, M., et al., *BaTiO3-based piezoelectrics: Fundamentals, current status, and perspectives.* Applied Physics Reviews, 2017. **4**(4): p. 041305.

76. Jona, F. and G. Shirane, *"Ferroelectric Crystals", Dover Publications, Inc, New York 1993, chapter V11.*

77. Newnham, R., *Properties of Materials Anisotropy: Anisotropy, Symmetry.* Structure, 2005.

78. Arlt, G., *Twinning in ferroelectric and ferroelastic ceramics: stress relief.* Journal of materials Science, 1990. **25**(6): p. 2655-2666.

79. Tagantsev, A.K., L.E. Cross, and J. Fousek, *Domains in ferroic crystals and thin films*. Vol. 13. 2010: Springer.

80. Kao, K.C., *Dielectric phenomena in solids*. 2004: Elsevier Academic Press.

81. Fousek, J., *Permissible domain walls in ferroelectric species.* Czechoslovak Journal of Physics B, 1971. **21**(9): p. 955-968.

82. Burfoot, J.C. and W.T. George, *polar dielectrics and their applications*. 1979, London: Palgrave Macmillan.

83. Samara, G.A., *Ferroelectricity revisited - Advances in materials and physics*, in *Solid State Physics, Vol 56*, H. Ehrenreich and F. Spaepen, Editors. 2001. p. 239-458.

84. Rubio-Marcos, F., et al., *Ferroelectric domain wall motion induced by polarized light.* Nature communications, 2015. **6**(1): p. 1-9.

85. Lines, M.E. and A.M. Glass, *principles and applications of ferroelectrics and related materials* 1977, Clarendon: Oxford.

86. Eric Cross, L., *Ferroelectric ceramics: tailoring properties for specific applications*, in *Ferroelectric ceramics*. 1993, Springer. p. 1-85.

87. Zhang, Q., et al., *Domain wall excitations and their contributions to the weak-signal response of doped lead zirconate titanate ceramics.* Journal of applied Physics, 1988. **64**(11): p. 6445-6451.

88. Zhang, Q., et al., *Direct evaluation of domain-wall and intrinsic contributions to the dielectric and piezoelectric response and their temperature dependence on lead zirconate-titanate ceramics.* Journal of Applied Physics, 1994. **75**(1): p. 454-459.

89. Hagemann, H.-J., *Loss mechanisms and domain stabilisation in doped $BaTiO_3$.* Journal of Physics C: Solid State Physics, 1978. **11**(15): p. 3333.

90. Damjanovic, D., *Stress and frequency dependence of the direct piezoelectric effect in ferroelectric ceramics.* Journal of Applied Physics, 1997. **82**(4): p. 1788-1797.

91. Bondarenko, E., V.Y. Topolov, and A. Turik, *The role of 90 domain wall displacements in forming physical properties of perovskite ferroelectric ceramics.* Ferroelectrics Letters Section, 1991. **13**(1): p. 13-19.

92. Kounga, A.B., et al., *High-temperature poling of ferroelectrics.* Journal of Applied Physics, 2008. **104**(2): p. 024116.

93. Kungl, H. and M.J. Hoffmann, *Temperature dependence of poling strain and strain under high electric fields in LaSr-doped morphotropic PZT and its relation to changes in structural characteristics.* Acta Materialia, 2007. **55**(17): p. 5780-5791.

94. Boser, O., *Statistical-theory of hysteresis in ferroelectric materials.* Journal of Applied Physics, 1987. **62**(4): p. 1344-1348.

95. Heywang, W., K. Lubitz, and W. Wersing, *Piezoelectricity - Evolution and future of a Technology*. 2008, The Netherlands: Springer.

96. Damjanovic, D., *Ferroelectric, dielectric and piezoelectric properties of ferroelectric thin films and ceramics.* Reports on Progress in Physics, 1998. **61**(9): p. 1267.

97. Smolenskii, G.A., et al., *NEW FERROELECTRICS OF COMPLEX COMPOSITION .4.* Soviet Physics-Solid State, 1961. **2**(11): p. 2651-2654.

98. Herabut, A. and A. Safari, *Processing and electromechanical properties of* $(Bi_{0.5}Na_{0.5})_{(1-1.5x)}La_xTiO_3$ *ceramics.* Journal of the American Ceramic Society, 1997. **80**(11): p. 2954-2958.

99. Suchanicz, J., et al., *Electrostrictive strain and pyroeffect in the region of phase coexistence in* $Na_{0.5}Bi_{0.5}TiO_3$. Ferroelectrics, 1988. **77**: p. 107-110.

100. Zvirgzds, J.A., et al., *X-ray study of phase-transitions in ferroelectric* $Na_{0.5}Bi_{0.5}TiO_3$. Ferroelectrics, 1982. **40**(1-2): p. 75-77.

101. Siny, I.G., C.S. Tu, and V.H. Schmidt, *Critical acoustic behavior of the relaxor ferroelectric* $Na_{1/2}Bi_{1/2}TiO_3$ *in the intertransition region.* Physical Review B, 1995. **51**(9): p. 5659-5665.

102. Jones, G.O. and P.A. Thomas, *The tetragonal phase of* $Na_{0.5}Bi_{0.5}TiO_3$ *- a new variant of the perovskite structure.* Acta Crystallographica Section B-Structural Science, 2000. **56**: p. 426-430.

103. Jones, G.O. and P.A. Thomas, *Investigation of the structure and phase transitions in the novel A-site substituted distorted perovskite compound* $Na_{0.5}Bi_{0.5}TiO_3$. Acta Crystallographica Section B-Structural Science Crystal Engineering and Materials, 2002. **58**: p. 168-178.

104. Glazer, A., *Simple ways of determining perovskite structures.* Acta Crystallographica Section A: Crystal Physics, Diffraction, Theoretical and General Crystallography, 1975. **31**(6): p. 756-762.

105. Jones, G. and P. Thomas, *Investigation of the structure and phase transitions in the novel A-site substituted distorted perovskite compound* $Na_{0.5}Bi_{0.5}TiO_3$. Acta Crystallographica Section B: Structural Science, 2002. **58**(2): p. 168-178.

106. Sakata, K. and Y. Masuda, *Ferroelectric and antiferroelectric properties of $(Na_{0.5}Bi_{0.5})TiO_3$-$SrTiO_3$ solid solution ceramics.* Ferroelectrics, 1974. **7**(1): p. 347-349.

107. Vakhrushev, S., et al., *Phase transitions and soft modes in sodium bismuth titanate.* Ferroelectrics, 1985. **63**(1): p. 153-160.

108. Suchanicz, J., *Behaviour of $Na_{0.5}Bi_{0.5}TiO_3$ ceramics in the ac electric field.* Ferroelectrics, 1998. **209**(1): p. 561-568.

109. Tu, C.-S., I. Siny, and V.H. Schmidt, *Sequence of dielectric anomalies and high-temperature relaxation behavior in $Na_{1/2}Bi_{1/2}TiO_3$.* Physical Review B, 1994. **49**(17): p. 11550.

110. Xu, C., D. Lin, and K. Kwok, *Structure, electrical properties and depolarization temperature of $(Bi_{0.5}Na_{0.5})TiO_3$-$BaTiO_3$ lead-free piezoelectric ceramics.* Solid state sciences, 2008. **10**(7): p. 934-940.

111. Schmitt, L.A., et al., *Comparative study of two lead-free piezoceramics using diffraction techniques.* Journal of Applied Crystallography, 2010. **43**(4): p. 805-810.

112. Yu, H. and Z.-G. Ye, *Dielectric, ferroelectric, and piezoelectric properties of the lead-free $(1-x)(Na_{0.5}Bi_{0.5})TiO_3$-$xBiAlO_3$ solid solution.* Applied physics letters, 2008. **93**(11): p. 112902.

113. Wang, X., et al., *Electromechanical properties and dielectric behavior of $(Bi_{1/2}Na_{1/2})_{(1-1.5x)}Bi_xTiO_3$ lead-free piezoelectric ceramics.* Solid State Communications, 2004. **129**(5): p. 319-323.

114. Takenaka, T., *Piezoelectric properties of some lead-free ferroelectric ceramics.* Ferroelectrics, 1999. **230**(1): p. 87-98.

115. Jaffe, B., W.R. Cook, and H. Jaffe, *piezoelectric ceramics*. 1971, London: Academic.

116. Yoshii, K., et al., *Electrical properties and depolarization temperature of $(Bi_{1/2}Na_{1/2})TiO_3$-$(Bi_{1/2}K_{1/2})TiO_3$ lead-free piezoelectric ceramics.* Japanese Journal of Applied Physics Part 1-Regular Papers Brief Communications & Review Papers, 2006. **45**(5B): p. 4493-4496.

117. Jo, W., et al., *On the phase identity and its thermal evolution of lead free $(Bi_{1/2}Na_{1/2})TiO_3$-6 mol% $BaTiO_3$.* Journal of Applied Physics, 2011. **110**(7): p. 074106.

118. Jo, W., et al., *Giant electric-field-induced strains in lead-free ceramics for actuator applications - status and perspective.* Journal of Electroceramics, 2012. **29**(1): p. 71-93.

119. Acosta, M., W. Jo, and J. Rodel, *Temperature- and frequency-dependent properties of the $0.75Bi_{1/2}Na_{1/2}TiO_3$-$0.25SrTiO_3$ lead-free incipient piezoceramic.* Journal of the American Ceramic Society, 2014. **97**(6): p. 1937-1943.

120. Xu, C., D. Lin, and K.W. Kwok, *Structure, electrical properties and depolarization temperature of $(Bi_{0.5}Na_{0.5})TiO_3$-$BaTiO_3$ lead-free piezoelectric ceramics.* Solid state sciences, 2008. **10**(7): p. 934-940.

121. Xu, Q., et al., *Synthesis and piezoelectric and ferroelectric properties of $(Na_{0.5}Bi_{0.5})_{1-x}Ba_xTiO_3$ ceramics.* Materials Chemistry and Physics, 2005. **90**(1): p. 111-115.

122. Chu, B.-J., et al., *Electrical properties of $Na_{1/2}Bi_{1/2}TiO_3$–$BaTiO_3$ ceramics.* Journal of the European Ceramic Society, 2002. **22**(13): p. 2115-2121.

123. Chen, M., et al., *Structure and electrical properties of $(Na_{0.5}Bi_{0.5})_{1-x}Ba_xTiO_3$ piezoelectric ceramics.* Journal of the European Ceramic Society, 2008. **28**(4): p. 843-849.

124. Takenaka, T., K.-i.M.K.-i. Maruyama, and K.S.K. Sakata, *$(Bi_{1/2}Na_{1/2})TiO_3$–$BaTiO_3$ system for lead-free piezoelectric ceramics.* Japanese journal of applied physics, 1991. **30**(9S): p. 2236.

125. Bokov, A.A. and Z.G. Ye, *Recent progress in relaxor ferroelectrics with perovskite structure.* Journal of Materials Science, 2006. **41**(1): p. 31-52.

126. Ehmke, M., et al., *Stabilization of the fatigue-resistant phase by CuO addition in $(Bi_{1/2}Na_{1/2})TiO_3$–$BaTiO_3$.* Journal of the American Ceramic Society, 2011. **94**(8): p. 2473-2478.

127. Glaum, J., et al., *Influence of B-Site disorder on the properties of unpoled $Bi_{1/2}Na_{1/2}TiO_3$–$BaTiO_3$-$0.06Ba(Zr_xTi_{1-x})O_3$ piezoceramics.* Journal of the American Ceramic Society, 2016. **99**(8): p. 2801-2808.

128. Jo, W., et al., *Effect of Nb-donor and Fe-acceptor dopants in $(Bi_{1/2}Na_{1/2})TiO_3$–$BaTiO_3$-$(K_{0.5}Na_{0.5})NbO_3$ lead-free piezoceramics.* Journal of Applied Physics, 2010. **108**(1).

129. Groh, C., et al., *Relaxor/ferroelectric composites: A solution in the quest for practically viable lead-free incipient piezoceramics.* Advanced Functional Materials, 2014. **24**(3): p. 356-362.

130. Acosta, M., et al., *Tailoring ergodicity through selective A-site doping in the $Bi_{1/2}Na_{1/2}TiO_3$-$Bi_{1/2}K_{1/2}TiO_3$ system.* Journal of Applied Physics, 2015. **117**(13): p. 134106.

131. Jo, W., et al., *Origin of the large strain response in $(K_{0.5}Na_{0.5})NbO_3$-modified $(Bi_{0.5}Na_{0.5})TiO_3$-$BaTiO_3$ lead-free piezoceramics.* Journal of Applied Physics, 2009. **105**(9): p. 094102.

132. Rahman, J.U., et al., *Dielectric, ferroelectric and field-induced strain response of lead-free $BaZrO_3$-modified $Bi_{0.5}Na_{0.5}TiO_3$ ceramics.* Current Applied Physics, 2014. **14**(3): p. 331-336.

133. Maqbool, A., et al., *Enhanced electric field-induced strain and ferroelectric behavior of $(Bi_{0.5}Na_{0.5})TiO_3$-$BaTiO_3$–$SrZrO_3$ lead-free ceramics.* Ceramics International, 2014. **40**(8): p. 11905-11914.

134. Jo, W., et al., *Evolving morphotropic phase boundary in lead-free $(Bi_{1/2}Na_{1/2})TiO_3$–$BaTiO_3$ piezoceramics.* Journal of applied physics, 2011. **109**(1): p. 014110.

135. Song, T.K., et al., *Effects of Zr Doping on the Depolarization Temperature and the Piezoelectric Properties in $(Bi_{0.5}Na_{0.5})TiO_3$-$BaTiO_3$ Lead-free Ceramics.* Journal of Korean Physical Society, 2010. **57**: p. 1905.

136. Song, T., et al., *Depolarization temperatures in Pb-free piezoelectric materials.* Journal of the Korean Physical Society, 2007. **51**(9): p. 697-700.

137. Dittmer, R., *Lead-Free Piezoceramics–Ergodic and Nonergodic Relaxor Ferroelectrics Based on Bismuth Sodium Titanate*. 2013, Technische Universität.

138. Patel, S., et al., *Thermomechanical Energy Conversion Potential of Lead-Free $0.50Ba(Zr_{0.2}Ti_{0.8})O_3$-$0.50(Ba_{0.7}Ca_{0.3})TiO_3$ Bulk Ceramics.* Energy Technology, 2017: p. n/a-n/a.

139. Fan, Z.M., et al., *Domain disruption and defect accumulation during unipolar electric fatigue in a BZT-BCT ceramic.* Applied Physics Letters, 2017. **111**(25).

140. Xue, D., et al., *Phase transitions and phase diagram of $Ba(Zr_{0.2}Ti_{0.8})O_3$-$x(Ba_{0.7}Ca_{0.3})TiO_3$ Pb-free system by anelastic measurement.* Journal of Applied Physics, 2015. **117**(12).

141. Acosta, M., et al., *Origin of the large piezoelectric activity in $(1-x)Ba(Zr_{0.2}Ti_{0.8})O_3$-$x(Ba_{0.7}Ca_{0.3})TiO_3$ ceramics.* Physical Review B, 2015. **91**(10).

142. Lu, S., et al., *Temperature driven nano-domain evolution in lead-free $Ba(Zr_{0.2}Ti_{0.8})O_3$-$50(Ba_{0.7}Ca_{0.3})TiO_3$ piezoceramics.* Applied Physics Letters, 2014. **105**(3).

143. Acosta, M., et al., *Relationship between electromechanical properties and phase diagram in the $Ba(Zr_{0.2}Ti_{0.8})O_3$-$x(Ba_{0.7}Ca_{0.3})TiO_3$ lead-free piezoceramic.* Acta Materialia, 2014. **80**: p. 48-55.

144. Keeble, D.S., et al., *Revised structural phase diagram of $(Ba_{0.7}Ca_{0.3}TiO_3)$-$(BaZr_{0.2}Ti_{0.8}O_3)$.* Applied Physics Letters, 2013. **102**(9): p. 092903.

145. Liu, W. and X. Ren, *Large Piezoelectric Effect in Pb-Free Ceramics.* Physical Review Letters, 2009. **103**(25).

146. Xu, X., et al., *Influence of the Strain on Dielectric and Ferroelectric Properties of $0.5BaZr_{0.2}Ti_{0.8}O_3$-$0.5Ba_{0.7}Ca_{0.3}TiO_3$.* Journal of the American Ceramic Society, 2015. **98**(9): p. 2823-2828.

147. Choi, M.-J., et al., *Microstructural and electrical properties of lead-free $0.5Ba(Zr_{0.2}Ti_{0.8})O_3$-$0.5(Ba_{0.7}Ca_{0.3})TiO_3$ (BZT-BCT) epitaxial films grown on Si (001) substrates.* Scripta Materialia, 2015. **108**: p. 96-99.

148. Zhang, Y., et al., *Correlation Between Piezoelectric Properties and Phase Coexistence in (Ba,Ca)(Ti,Zr)O_3 Ceramics.* Journal of the American Ceramic Society, 2014. **97**(9): p. 2885-2891.

149. Praveen, J.P., et al., *Large piezoelectric strain observed in sol-gel derived BZT-BCT ceramics.* Current Applied Physics, 2014. **14**(3): p. 396-402.

150. Xue, D., et al., *Elastic, piezoelectric, and dielectric properties of $Ba(Zr_{0.2}Ti_{0.8})O_3$-$50(Ba_{0.7}Ca_{0.3})TiO_3$ Pb-free ceramic at the morphotropic phase boundary.* Journal of Applied Physics, 2011. **109**(5).

151. Zakhozheva, M., et al., *Wide Compositional Range In Situ Electric Field Investigations on Lead-Free $Ba(Zr_{0.2}Ti_{0.8})O_3$-$x(Ba_{0.7}Ca_{0.3})TiO_3$ Piezoceramic.* Physical Review Applied, 2015. **3**(6).

152. Puli, V.S., et al., *Nanoscale polarisation switching and leakage currents in $(Ba_{0.955}Ca_{0.045})(Zr_{0.17}Ti_{0.83})O_3$ epitaxial thin films.* Journal of Physics D-Applied Physics, 2015. **48**(35).

153. Zakhozheva, M., et al., *In situ electric field induced domain evolution in $Ba(Zr_{0.2}Ti_{0.8})O_3$-$0.3(Ba_{0.7}Ca_{0.3})TiO_3$ ferroelectrics.* Applied Physics Letters, 2014. **105**(11).

154. Ehmke, M.C., et al., *Phase coexistence and ferroelastic texture in high strain (1-x) $Ba(Zr_{0.2}Ti_{0.8})O_3$-$x(Ba_{0.7}Ca_{0.3})TiO_3$ piezoceramics.* Journal of Applied Physics, 2012. **111**(12).

155. Cox, D., et al., *Universal phase diagram for high-piezoelectric perovskite systems.* Applied Physics Letters, 2001. **79**(3): p. 400-402.

156. Bao, H., et al., *A modified lead-free piezoelectric BZT-xBCT system with higher T-C.* Journal of Physics D-Applied Physics, 2010. **43**(46).

157. Benabdallah, F., et al., *Linking large piezoelectric coefficients to highly flexible polarization of lead free $BaTiO_3$-$CaTiO_3$-$BaZrO_3$ ceramics.* Journal of Applied Physics, 2011. **109**(12): p. 124116.

158. Gao, J., et al., *Microstructure basis for strong piezoelectricity in Pb-free $Ba(Zr_{0.2}Ti_{0.8})O_3$-$(Ba_{0.7}Ca_{0.3})TiO_3$ ceramics.* Applied Physics Letters, 2011. **99**(9).

159. Damjanovic, D., et al., *Elastic, dielectric, and piezoelectric anomalies and Raman spectroscopy of $0.5Ba(Ti_{0.8}Zr_{0.2}O_3$-$0.5(Ba_{0.7}Ca_{0.3})TiO_3$.* Applied Physics Letters, 2012. **100**(19): p. 192907.

160. Brandt, D.R.J., et al., *Mechanical constitutive behavior and exceptional blocking force of lead-free BZT-xBCT piezoceramics.* Journal of Applied Physics, 2014. **115**(20).

161. Tian, Y., et al., *Phase Transition Behavior and Large Piezoelectricity Near the Morphotropic Phase Boundary of Lead-Free $(Ba_{0.85}Ca_{0.15})(Zr_{0.1}Ti_{0.9})O_3$ Ceramics.* Journal of the American Ceramic Society, 2013. **96**(2): p. 496-502.

162. Zhang, L., et al., *Phase transitions and the piezoelectricity around morphotropic phase boundary in $Ba(Zr_{0.2}Ti_{0.8})O_3$-$x(Ba_{0.7}Ca_{0.3})TiO_3$ lead-free solid solution.* Applied Physics Letters, 2014. **105**(16): p. 162908.

163. Binnig, G., et al., *Surface studies by scanning tunneling microscopy.* Physical review letters, 1982. **49**(1): p. 57.

164. Kalinin, S.V. and D.A. Bonnell, *Imaging mechanism of piezoresponse force microscopy of ferroelectric surfaces.* Physical Review B, 2002. **65**(12).

165. Guthner, P. and K. Dransfeld, *Local poling of ferroelectric polymers by scanning force microscopy.* Applied Physics Letters, 1992. **61**(9): p. 1137-1139.

166. Hidaka, T., et al., *Formation and observation of 50 nm polarized domains in $PbZr_{1-x}Ti_xO_3$ thin film using scanning probe microscope.* Applied physics letters, 1996. **68**(17): p. 2358-2359.

167. Gruverman, A., O. Auciello, and Tokumoto, *Scanning force microscopy for the study of domain structure in ferroelectric thin films.* Journal of Vacuum Science & Technology B: Microelectronics and Nanometer Structures Processing, Measurement, and Phenomena, 1996. **14**(2): p. 602-605.

168. Gruverman, A., O. Auciello, and H. Tokumoto, *Nanoscale investigation of fatigue effects in $Pb(Zr,Ti)O_3$ films.* Applied Physics Letters, 1996. **69**(21): p. 3191-3193.

169. Rodriguez, B.J., et al., *Electromechanical imaging of biomaterials by scanning probe microscopy.* Journal of structural biology, 2006. **153**(2): p. 151-159.

170. Gruverman, A., et al., *Scanning force microscopy as a tool for nanoscale study of ferroelectric domains.* Ferroelectrics, 1996. **184**: p. 11-20.

171. Gruverman, A., et al., *Domain-structure and polarization reversal in ferroelectrics studied by atomic-force microscopy.* Journal of Vacuum Science & Technology B, 1995. **13**(3): p. 1095-1099.

172. Gruverman, A. and S.V. Kalinin, *Piezoresponse force microscopy and recent advances in nanoscale studies of ferroelectrics.* Journal of Materials Science, 2006. **41**(1): p. 107-116.

173. Kalinin, S.V., et al., *Vector piezoresponse force microscopy.* Microscopy and Microanalysis, 2006. **12**(3): p. 206-220.

174. Guyonnet, J., *Ferroelectric Domain Walls: Statics, Dynamics, and Functionalities Revealed by Atomic Force Microscopy*. 2014: Springer Science & Business Media.

175. Ganpule, C., et al., *Imaging three-dimensional polarization in epitaxial polydomain ferroelectric thin films.* Journal of applied physics, 2002. **91**(3): p. 1477-1481.

176. Gruverman, A., O. Auciello, and H. Tokumoto, *Scanning force microscopy: application to nanoscale studies of ferroelectric domains.* Integrated Ferroelectrics, 1998. **19**(1-4): p. 49-83.

177. Jesse, S., H.N. Lee, and S.V. Kalinin, *Quantitative mapping of switching behavior in piezoresponse force microscopy.* Review of Scientific Instruments, 2006. **77**(7).

178. Jesse, S., A.P. Baddorf, and S.V. Kalinin, *Switching spectroscopy piezoresponse force microscopy of ferroelectric materials.* Applied Physics Letters, 2006. **88**(6).

179. Yang, S.M. and Y. Kim, *Nanoscale probing of ferroelectric domain switching using piezoresponse force microscopy.* Journal of the Korean Ceramic Society, 2019. **56**(4): p. 340-349.

180. Melitz, W., et al., *Kelvin probe force microscopy and its application.* Surface science reports, 2011. **66**(1): p. 1-27.

181. Kalinin, S.V. and A. Gruverman, *Scanning probe microscopy: electrical and electromechanical phenomena at the nanoscale*. Vol. 1. 2007: Springer Science & Business Media.

182. Takano, H., et al., *Chemical and biochemical analysis using scanning force microscopy.* Chemical Reviews, 1999. **99**(10): p. 2845-2890.

183. Nonnenmacher, M., M. o'Boyle, and H.K. Wickramasinghe, *Kelvin probe force microscopy.* Applied physics letters, 1991. **58**(25): p. 2921-2923.

184. Shikler, R., et al., *Two-dimensional surface band structure of operating light emitting devices.* Journal of applied physics, 1999. **86**(1): p. 107-113.

185. Rödel, J., et al., *Transferring lead-free piezoelectric ceramics into application.* Journal of the European Ceramic Society, 2015. **35**(6): p. 1659-1681.

186. Saito, Y., et al., *Lead-free piezoceramics.* Nature, 2004. **432**(7013): p. 84-7.

187. Gao, J.H., et al., *Recent Progress on $BaTiO_3$-Based Piezoelectric Ceramics for Actuator Applications.* Actuators, 2017. **6**(3): p. 24.

188. Zheng, T., et al., *Recent development in lead-free perovskite piezoelectric bulk materials.* Progress in Materials Science, 2018. **98**: p. 552-624.

189. Liu, W., L. Cheng, and S. Li, *Prospective of $(BaCa)(ZrTi)O_3$ Lead-free Piezoelectric Ceramics.* Crystals, 2019. **9**(3): p. 179.

190. Gao, J., et al., *Symmetry determination on Pb-free piezoceramic $0.5Ba(Zr_{0.2}Ti_{0.8})O_3$-$0.5(Ba_{0.7}Ca_{0.3})TiO_3$ using convergent beam electron diffraction method.* Journal of Applied Physics, 2014. **115**(5): p. 054108.

191. Hao, J., et al., *Correlation between the microstructure and electrical properties in high-performance $(Ba_{0.85}Ca_{0.15})(Zr_{0.1}Ti_{0.9})O_3$ lead-free piezoelectric ceramics.* Journal of the American Ceramic Society, 2012. **95**(6): p. 1998-2006.

192. Tutuncu, G., et al., *Domain wall motion and electromechanical strain in lead-free piezoelectrics: Insight from the model system $(1-x)Ba(Zr_{0.2}Ti_{0.8})O_3$–$x(Ba_{0.7}Ca_{0.3})TiO_3$ using in situ high-energy X-ray diffraction during application of electric fields.* Journal of Applied Physics, 2014. **115**(14): p. 144104.

193. Keeble, D.S., et al., *Revised structural phase diagram of $(Ba_{0.7}Ca_{0.3}TiO_3)$-$(BaZr_{0.2}Ti_{0.8}O_3)$.* Applied Physics Letters, 2013. **102**(9): p. 092903.

194. Bjørnetun Haugen, A., et al., *Structure and phase transitions in $0.5(Ba_{0.7}Ca_{0.3}TiO_3)$-$0.5(BaZr_{0.2}Ti_{0.8}O_3)$ from −100 °C to 150 °C.* Journal of Applied Physics, 2013. **113**(1): p. 014103.

195. Torres-Matheus, O.A., R.E. Garcia, and C.M. Bishop, *Microstructural phase coexistence kinetics near the polymorphic phase boundary.* Acta Materialia, 2021. **206**: p. 116579.

196. Puli, V.S., et al., *Structure, dielectric tunability, thermal stability and diffuse phase transition behavior of lead free BZT-BCT ceramic capacitors.* Journal of Physics and Chemistry of Solids, 2013. **74**(3): p. 466-475.

197. Zhang, Y., et al., *High bipolar fatigue resistance of BCTZ lead-free piezoelectric ceramics.* Journal of the American Ceramic Society, 2016. **99**(1): p. 174-182.

198. Wang, H., et al., *Infrared optical properties of ferroelectric $0.5BaZr_{0.2}Ti_{0.8}O_3$–$0.5Ba_{0.7}Ca_{0.3}TiO_3$ thin films.* Ceramics International, 2015. **41**(1): p. 475-480.

199. Wang, H., et al., *Spectroscopic ellipsometry study of $0.5BaZr_{0.2}Ti_{0.8}O_3$–$0.5Ba_{0.7}Ca_{0.3}TiO_3$ ferroelectric thin films.* Journal of Alloys and Compounds, 2014. **615**: p. 526-530.

200. Wang, H., et al., *Optical Character of Barium Titanate Based Thin Films around the Phase Transition.* Ferroelectrics, 2016. **491**(1): p. 8-14.

201. Acosta, M., et al., *Mechanisms of electromechanical response in $(1-x)Ba(Zr_{0.2}Ti_{0.8})O_3$-$x(Ba_{0.7}Ca_{0.3})TiO_3$ ceramics.* Applied Physics Letters, 2015. **107**(14).

202. Silva, J.P.B., et al., *Ferroelectric switching dynamics in $0.5Ba(Zr_{0.2}Ti_{0.8})O_3$-$0.5(Ba_{0.7}Ca_{0.3})TiO_3$ thin films.* Applied Physics Letters, 2018. **113**(8): p. 082903.

203. Rojas, V., et al., *Influence of composition on the unipolar electric fatigue of $Ba(Zr_{0.2}Ti_{0.8})O_3$-$(Ba_{0.7}Ca_{0.3})TiO_3$ lead-free piezoceramics.* Journal of the American Ceramic Society, 2017. **100**(10): p. 4699-4709.

204. Lv, X., X.X. Zhang, and J.G. Wu, *Nano-domains in lead-free piezoceramics: a review.* Journal of Materials Chemistry A, 2020. **8**(20): p. 10026-10073.

205. Gao, J., et al., *Major contributor to the large piezoelectric response in (1-x)$Ba(Zr_{0.2}Ti_{0.8})O_3$-x$(Ba_{0.7}Ca_{0.3})TiO_3$ ceramics: Domain wall motion.* Applied Physics Letters, 2014. **104**(25).

206. Tagantsev, A.K., L.E. Cross, and J. Fousek, *Domains in Ferroic Crystals and Thin Films.* Domains in Ferroic Crystals and Thin Films, 2010: p. 1-821.

207. Zhang, Y., et al., *Characterization of domain distributions by second harmonic generation in ferroelectrics.* Npj Computational Materials, 2018. **4**(1).

208. Jiang, X., et al., *Ferroelectric domain evolution in a $Ba(Zr_{0.2}Ti_{0.8})O_3$-0.5$(Ba_{0.7}Ca_{0.3})TiO_3$ piezoceramic studied using piezoresponse force microscopy.* Applied Physics Letters, 2021. **118**(26): p. 262902.

209. Wang, H., et al., *Direct Observation of Huge Flexoelectric Polarization around Crack Tips.* Nano Lett, 2020. **20**(1): p. 88-94.

210. Fan, Z.M., et al., *Domain disruption and defect accumulation during unipolar electric fatigue in a BZT-BCT ceramic.* Applied Physics Letters, 2017. **111**(25): p. 252902.

211. Fan, Z.M., et al., *An ideal amplitude window against electric fatigue in $BaTiO_3$-based lead-free piezoelectric materials.* Acta Materialia, 2018. **151**: p. 253-259.

212. Zheng, T., et al., *The structural origin of enhanced piezoelectric performance and stability in lead free ceramics.* Energy & Environmental Science, 2017. **10**(2): p. 528-537.

213. Coondoo, I., et al., *Synthesis and characterization of lead-free 0.5$Ba(Zr_{0.2}Ti_{0.8})O_3$-0.5$(Ba_{0.7}Ca_{0.3})TiO_3$ ceramic.* Journal of Applied Physics, 2013. **113**(21).

214. Shvartsman, V.V., et al., *Fatigue-induced evolution of domain structure in ferroelectric lead zirconate titanate ceramics investigated by piezoresponse force microscopy.* Journal of Applied Physics, 2005. **98**(9).

215. Dietz, C., *Sensing in-plane nanomechanical surface and sub-surface properties of polymers: local shear stress as function of the indentation depth.* Nanoscale, 2018. **10**(1): p. 460-468.

216. Liu, N., et al., *Visualization of polar nanoregions in lead-free relaxors via piezoresponse force microscopy in torsional dual AC resonance tracking mode.* Nanoscale, 2015. **7**(27): p. 11787-11796.

217. Liu, N., et al., *Revealing the core-shell interactions of a giant strain relaxor ferroelectric $0.75Bi_{1/2}Na_{1/2}TiO_3$-$0.25SrTiO_3$.* Scientific Reports, 2016. **6**.

218. Lu, S., et al., *Temperature driven nano-domain evolution in lead-free $Ba(Zr_{0.2}Ti_{0.8})O_3$-$50(Ba_{0.7}Ca_{0.3})TiO_3$ piezoceramics.* Applied Physics Letters, 2014. **105**(3): p. 032903.

219. Randall, C.A., et al., *Intrinsic and extrinsic size effects in fine-grained morphotropic-phase-boundary lead zirconate titanate ceramics.* Journal of the American Ceramic Society, 1998. **81**(3): p. 677-688.

220. Cao, W.W. and C.A. Randall, *Grain size and domain size relations in bulk ceramic ferroelectric materials.* Journal of Physics and Chemistry of Solids, 1996. **57**(10): p. 1499-1505.

221. Wu, H., et al., *Microstructure at morphotropic phase boundary in $Pb(Mg_{1/3}Nb_{2/3})O_3$-$PbTiO_3$ ceramic: Coexistence of nano-scaled {110}-type rhombohedral twin and {110}-type tetragonal twin.* Journal of Applied Physics, 2012. **112**(5): p. 052004.

222. Hong, S., et al., *Three-dimensional ferroelectric domain imaging of bulk $Pb(Zr,Ti)O_3$ by atomic force microscopy.* Applied Physics Letters, 2004. **84**(13): p. 2382-2384.

223. Sato, Y., T. Hirayama, and Y. Ikuhara, *Real-time direct observations of polarization reversal in a piezoelectric crystal: $Pb(Mg_{1/3}Nb_{2/3})O_3$-$PbTiO_3$ studied via in situ electrical biasing transmission electron microscopy.* Phys Rev Lett, 2011. **107**(18): p. 187601.

224. Coondoo, I., et al., *Temperature-dependent Raman spectroscopy, domain morphology and photoluminescence studies in lead-free BCZT ceramic.* Ceramics International, 2021. **47**(2): p. 2828-2838.

225. Tan, X., et al., *The Antiferroelectric ↔ Ferroelectric Phase Transition in Lead-Containing and Lead-Free Perovskite Ceramics.* Journal of the American Ceramic Society, 2011. **94**(12): p. 4091-4107.

226. Schultheiß, J., et al., *Domain wall-grain boundary interactions in polycrystalline $Pb(Zr_{0.7}Ti_{0.3})O_3$ piezoceramics.* Journal of the European Ceramic Society, 2020. **40**(12): p. 3965-3973.

227. Guo, H.Z., et al., *Unique single-domain state in a polycrystalline ferroelectric ceramic.* Physical Review B, 2014. **89**(10).

228. Brajesh, K., et al., *Relaxor ferroelectricity and electric-field-driven structural transformation in the giant lead-free piezoelectric$(Ba,Ca)(Ti,Zr)O_3$.* Physical Review B, 2015. **92**(22): p. 224112.

229. Li, B., J.E. Blendell, and K.J. Bowman, *Temperature-Dependent Poling Behavior of Lead-free BZT-BCT Piezoelectrics.* Journal of the American Ceramic Society, 2011. **94**(10): p. 3192-3194.

230. Brandt, D.R., et al., *Mechanical constitutive behavior and exceptional blocking force of lead-free BZT-xBCT piezoceramics.* Journal of Applied Physics, 2014. **115**(20): p. 204107.

231. Coondoo, I., et al., *Synthesis and characterization of lead-free $0.5Ba(Zr_{0.2}Ti_{0.8})O_3$-$0.5(Ba_{0.7}Ca_{0.3})TiO_3$ ceramic.* Journal of Applied Physics, 2013. **113**(21): p. 214107.

232. Koruza, J., et al., *Enhancing the operational range of piezoelectric actuators by uniaxial compressive preloading.* Journal of Physics D: Applied Physics, 2015. **48**(21): p. 215302.

233. Zhang, Y., et al., *Unipolar Fatigue Behavior of BCTZ Lead-Free Piezoelectric Ceramics.* Journal of the American Ceramic Society, 2016. **99**(4): p. 1287-1293.

234. Tagantsev, A.K., et al., *Polarization fatigue in ferroelectric films: Basic experimental findings, phenomenological scenarios, and microscopic features.* Journal of Applied Physics, 2001. **90**(3): p. 1387-1402.

235. Lupascu, D. and J. Rödel, *Fatigue in bulk lead zirconate titanate actuator materials.* Advanced Engineering Materials, 2005. **7**(10): p. 882-898.

236. Lupascu, D.C., *Fatigue in ferroelectric ceramics and related issues*. Vol. 61. 2013: Springer Science & Business Media.

237. Wang, D., Y. Fotinich, and G.P. Carman, *Influence of temperature on the electromechanical and fatigue behavior of piezoelectric ceramics.* Journal of applied physics, 1998. **83**(10): p. 5342-5350.

238. Jiang, Q. and L. Cross, *Effects of porosity on electric fatigue behaviour in PLZT and PZT ferroelectric ceramics.* Journal of materials science, 1993. **28**(16): p. 4536-4543.

239. Zeng, F.W., H. Wang, and H.-T. Lin, *Fatigue and failure responses of lead zirconate titanate multilayer actuator under unipolar high-field electric cycling.* Journal of Applied Physics, 2013. **114**(2): p. 024101.

240. Brennan, C., *Model of ferroelectric fatigue due to defect/domain interactions.* Ferroelectrics, 1993. **150**(1): p. 199-208.

241. Nuffer, J., D. Lupascu, and J. Rödel, *Damage evolution in ferroelectric PZT induced by bipolar electric cycling.* Acta Materialia, 2000. **48**(14): p. 3783-3794.

242. Nuffer, J., et al., *Microstructural modifications of ferroelectric lead zirconate titanate ceramics due to bipolar electric fatigue.* Journal of the European Ceramic Society, 2002. **22**(13): p. 2133-2142.

243. Glaum, J., et al., *Temperature and driving field dependence of fatigue processes in PZT bulk ceramics.* Acta materialia, 2011. **59**(15): p. 6083-6092.

244. Balke, N., et al., *Fatigue of lead zirconate titanate ceramics. I: Unipolar and DC loading.* Journal of the American Ceramic Society, 2007. **90**(4): p. 1081-1087.

245. Verdier, C., D. Lupascu, and J. Rödel, *Unipolar fatigue of ferroelectric lead–zirconate–titanate.* Journal of the European Ceramic Society, 2003. **23**(9): p. 1409-1415.

246. Wang, H., et al., *Fatigue responses of lead zirconate titanate stacks under semibipolar electric cycling with mechanical preload.* Journal of Applied Physics, 2010. **108**(8): p. 084107.

247. Wang, H., A.A. Wereszczak, and H.-T. Lin, *Fatigue response of a PZT multilayer actuator under high-field electric cycling with mechanical preload.* Journal of applied physics, 2009. **105**(1): p. 014112.

248. Bao, H., et al., *A modified lead-free piezoelectric BZT–xBCT system with higher TC.* Journal of Physics D: Applied Physics, 2010. **43**(46): p. 465401.

249. Gao, J., et al., *Symmetry determination on Pb-free piezoceramic $0.5Ba(Zr_{0.2}Ti_{0.8})O_3$-$0.5(Ba_{0.7}Ca_{0.3})TiO_3$ using convergent beam electron diffraction method.* Journal of Applied Physics, 2014. **115**(5).

250. Guo, H., et al., *Nanofragmentation of ferroelectric domains during polarization fatigue.* Advanced Functional Materials, 2015. **25**(2): p. 270-277.

251. Ma, C., et al., *Creation and destruction of morphotropic phase boundaries through electrical poling: a case study of lead-free $(Bi_{1/2}Na_{1/2})TiO_3$−$BaTiO_3$ piezoelectrics.* Physical review letters, 2012. **109**(10): p. 107602.

252. Ranjan, R. and A. Dviwedi, *Structure and dielectric properties of $(Na_{0.50}Bi_{0.50})_{1-x}Ba_xTiO_3$: $0 \leq x \leq 0.10$.* Solid state communications, 2005. **135**(6): p. 394-399.

253. Garg, R., et al., *Lead-free piezoelectric system $(Na_{0.5}Bi_{0.5})TiO_3$–$BaTiO_3$: Equilibrium structures and irreversible structural transformations driven by electric field and mechanical impact.* Physical Review B, 2013. **88**(1): p. 014103.

254. Hinterstein, M., et al., *Cyclic electric field response of morphotropic $Bi_{1/2}Na_{1/2}TiO_3$−$BaTiO_3$ piezoceramics.* Applied Physics Letters, 2015. **106**(22): p. 222904.

255. Ma, C., et al., *Domain structure-dielectric property relationship in lead-free $(1-x)(Bi_{1/2}Na_{1/2})TiO_3$−$xBaTiO_3$ ceramics.* Journal of applied physics, 2010. **108**(10): p. 104105.

256. Groszewicz, P.B., et al., *Nanoscale phase quantification in lead-free $(Bi_{1/2}Na_{1/2})TiO_3$−$BaTiO_3$ relaxor ferroelectrics by means of Na23 NMR.* Physical Review B, 2014. **90**(22): p. 220104.

257. Sapper, E., et al., *Electric-field–temperature phase diagram of the ferroelectric relaxor system (1−x)$Bi_{1/2}Na_{1/2}TiO_3$−x$BaTiO_3$ doped with manganese.* Journal of Applied Physics, 2014. **115**(19): p. 194104.

258. Schader, F.H., et al., *Stress-modulated relaxor-to-ferroelectric transition in lead-free ($Na_{1/2}Bi_{1/2}$)TiO_3−$BaTiO_3$ ferroelectrics.* Physical Review B, 2016. **93**(13): p. 134111.

259. Foronda, H., et al., *Thermally-induced loss of piezoelectricity in ferroelectric $Na_{0.5}Bi_{0.5}TiO_3$–$BaTiO_3$.* Materials Letters, 2014. **115**: p. 132-135.

260. Jo, W., et al., *Two-stage processes of electrically induced-ferroelectric to relaxor transition in 0.94($Bi_{1/2}Na_{1/2}$) TiO_3-0.06$BaTiO_3$.* Applied Physics Letters, 2013. **102**(19): p. 192903.

261. Shrout, T.R. and S.J. Zhang, *Lead-free piezoelectric ceramics: Alternatives for PZT?* Journal of Electroceramics, 2007. **19**(1): p. 113-126.

262. Damjanovic, D., *Contributions to the piezoelectric effect in ferroelectric single crystals and ceramics.* Journal of the American Ceramic society, 2005. **88**(10): p. 2663-2676.

263. Zhang, J., et al., *Semiconductor/relaxor 0-3 type composites without thermal depolarization in $Bi_{0.5}Na_{0.5}TiO_3$-based lead-free piezoceramics.* Nature Communications, 2015. **6**.

264. Riemer, L.M., et al., *Stress-induced phase transition in lead-free relaxor ferroelectric composites.* Acta Materialia, 2017. **136**: p. 271-280.

265. Sapper, E., et al., *Influence of electric fields on the depolarization temperature of Mn-doped (1-x) $Bi_{1/2}Na_{1/2}TiO_3$-x$BaTiO_3$.* Journal of Applied Physics, 2012. **111**(1): p. 014105.

266. Schader, F.H., *Mechanical stability of the electromechanical properties and phase transitions in lead-containing and lead-free ferroelectrics.* 2016.

267. Lynch, C.S., *The effect of uniaxial stress on the electro-mechanical response of 8/65/35 PLZT.* Acta materialia, 1996. **44**(10): p. 4137-4148.

268. Langdon, T.G., *Deformation mechanism maps for applications at high temperatures.* Ceramics International, 1980. **6**(1): p. 11-18.

269. Szot, K., et al., *Influence of Dislocations in Transition Metal Oxides on Selected Physical and Chemical Properties.* Crystals 2018. **8**(6): p. 241.

270. Whitworth, R., *Charged dislocations in ionic crystals.* Advances in Physics 1975. **24**(2): p. 203-304.

271. Adepalli, K.K., et al., *Tunable oxygen diffusion and electronic conduction in $SrTiO_3$ by dislocation-induced space charge fields.* Advanced Functional Materials, 2017. **27**(22): p. 1700243.

272. Dam, B., et al., *Origin of high critical currents in $YBa_2Cu_3O_{7-\delta}$ superconducting thin films.* Nature, 1999. **399**(6735): p. 439-442.

273. Kim, S.I., et al., *Dense dislocation arrays embedded in grain boundaries for high-performance bulk thermoelectrics.* Science, 2015. **348**(6230): p. 109-114.

274. Kontsos, A. and C.M. Landis, *Computational modeling of domain wall interactions with dislocations in ferroelectric crystals.* International journal of solids and structures, 2009. **46**(6): p. 1491-1498.

275. Höfling, M., et al., *Control of polarization in bulk ferroelectrics by mechanical dislocation imprint.* Science, 2021. **372**(6545): p. 961-964.

276. Ren, P., et al., *High temperature creep-mediated functionality in polycrystalline barium titanate.* Journal of the American Ceramic Society, 2020. **103**(3): p. 1891-1902.

277. Hoshina, T., *Size effect of barium titanate: fine particles and ceramics.* Journal of the ceramic society of Japan, 2013. **121**(1410): p. 156-161.

278. Cao, W. and C.A. Randall, *Grain size and domain size relations in bulk ceramic ferroelectric materials.* Journal of Physics and Chemistry of Solids, 1996. **57**(10): p. 1499-1505.

Declaration

Declaration

The work described in this thesis was carried out in the group of Physics of Surfaces, Department of Materials Science, Technische Universität Darmstadt during the period from October 2015 to September 2022. I certify that the work in this thesis is the author's original work, and no part of the thesis has been submitted for a degree at any other university or institute. Prior to the submission of this thesis, some work has been published as described in the relevant chapters herein.

Eidesstattliche Erklärung

Hiermit erkläre ich an Eides statt, dass ich die vorliegende Dissertation selbstständig und nur mit den angegebenen Quellen und Hilfsmitteln angefertigt habe. Von mir wurde weder an der Technischen Universität Darmstadt noch an einer anderen Hochschule ein Promotionsversuch unternommen.

Stuttgart, den 19.09.2022
Xijie Jiang

TECHNISCHE
UNIVERSITÄT
DARMSTADT